Interplay of Microwave Irradiation and Magnetic Fields in Charge Transport through Superconductor-Ferromagnet-Superconductor-Heterostructures

Dissertation zur Erlangung des akademischen Grades eines
Doktors der Naturwissenschaften (Dr. rer. nat.)

vorgelegt von

Andreas Bloch

an der

Mathematisch-Naturwissenschaftliche Sektion

Fachbereich Physik

Konstanz, 2024

Tag der mündlichen Prüfung: 16. Oktober 2023
1. Referentin: Prof. Dr. Elke Scheer
2. Referent: Prof. Dr. Angelo Di Bernardo

Zusammenfassung

Motiviert durch das Potential supraleitender Spintronik wird in der vorliegenden Dissertation das Wechselspiel von Supraleiter (S)-Ferromagnet (F)-Heterostrukturen unter Mikrowelleneinstrahlung, untersucht. Der aktuelle Stand der Forschung zu diesem Feld wird in Kapitel 1 vorgestellt.

Das Kapitel 2 fasst die physikalischen Grundlagen zusammen, die in unserer Arbeit eine Rolle spielen, wie Supraleitung und Josephson-Kontakte (JJ) (Abschnitt 2.1 und 2.2), Mikrowellen (Abschnitt 2.3), Magnetismus (2.4). Das Zusammenspiel all dieser Faktoren wird in Abschnitt 2.5 dargelegt, bei dem Proximity-Effekte auftreten (Abschnitt 2.5.1) und ferromagnetische Josephson-Kontakte (fJK) besonderes Verhalten unter MW Einstrahlung zeigen (Abschnitt 2.5.2).

Das Kapitel 3 stellt die Herstellung und den Aufbau der Proben in Abschnitt 3.1 und den experimentellen Aufbau in Abschnitt 3.2 vor. Die untersuchten Proben bestehen aus zwei Lagen 50 nm dünnem Al, die eine Lage von 12 nm dünnem Co so einfassen, dass ein Stromfluss durch die Co-Lage gewährleistet ist. Aus Gründen der Herstellung ist die 12 nm Co-Schicht in einem Teil der Probe auf ca. 1,5 nm reduziert, was die Ausprägung eines fJJ ermöglicht.

Die statischen Transporteingenschaften dieser S-F-Heterostrukturen ohne MW-Einstrahlung werden in Kapitel 4 zusammengefasst. Die supraleitende Energielücke $\Delta = 212\,\mu\text{eV}$ wird anhand einer Referenzprobe aus einem Al-AlOx-Al-Kontakt mit nominell selber Geometrie wie die eigentlichen Proben in Abschnitt 4.1 bestimmt. Die Transporteigenschaften ohne MW-Einstrahlung und ohne Magnetfeld B erlauben in Abschnitt 4.2 die Messung der kritschen Ströme der fJJ von $I_c = 4.4(1)\,\mu\text{A}$. Darüber hinaus kann die Diffusionskonstante für Elektronen in Al-Co-Heterostrukuren von $D = 21(4)\,\text{cm}^2\text{s}^{-1}$ bestimmt werden, die sich bei einer Co Dicke von $d_F > 10\,\text{nm}$ auf $D = 10(1)\,\text{cm}^2\text{s}^{-1}$ reduziert. Anhand verschiedener Merkmale in den Strom-Spannungs-Kurven (I-V-Kurven) werden in Abschnitt 4.3 unterschiedliche Probenteile identifiziert, die durch die Schattenbedampfungsmethode entstehen. Jede Probe besteht demnach aus reinen supraleitenden Teilen (S-Teil), aus Teilen bei denen die Supraleitung in Al durch die darauf oder darunter liegende Co-Lage entweder stark geschwächt oder ganz unterdrückt wird (SF-Teil) und aus den Teilen, bei denen zwei Al-Lagen die Co-Lage einfassen und einen fJJ bilden können (S/FS Teil). In Abschnitt 4.4 sind Abkühlkurven gezeigt, die eine supraleitende Sprungtemperatur von $T_c = 1.55(5)\,\text{K}$ aufweisen. Die Messungen unter Magnetfeldeinfluss in Abschnitt 4.5 ergeben kritische Magnetfelder von $B_c \approx 320\,\text{mT}$,

aus denen sich die diffusive supraleitende Kohärenzlänge $\xi_D \approx 32\,\mathrm{nm}$ und die magnetische Eindringtiefe $\lambda \approx 719(32)\,\mathrm{nm}$ bestimmen lassen. Das Al ist in unserer Probengeometrie demnach ein S vom Typ II.

Die dynamischen Transporteigenschaften unter MW-Einstrahlung sind in Kapitel 5 zusammengefasst. Abschnitt 5.1 zeigt eine MW-induzierte Erwärmung der Proben auf, wobei der S/FS Teil mit dem fJJ lokal stärker erwärmt wird, was wir als Kopplung der MW mit dem F interpretieren. Die Supraleitung in den S-Teilen kann hingegen durch MW verstärkt werden, was in Abschnitt 5.2 analysiert wird. Dabei werden Quasiteilchen durch MW in Zustände angeregt, die weiter von der Fermienergie entfernt sind. Dort können nun freigewordene Zustände von Elektronen besetzt werden, die Cooperpaare bilden, was die Supraleitung verstärkt. In Abschnitt 5.3 werden Beobachtungen eines außergewöhnlichen Verlaufs des kritischen Stroms I_c bei Erhöhung des B-Feldes unter MW Einstrahlung gezeigt. Dabei können verschiedene Effekte unterschieden werden. Erstens ein nicht-monotoner $I_c(B)$-Verlauf, bei dem I_c um $B = 0\,\mathrm{T}$ unterdrückt ist und sich bei Erhöhung des B-Feldes wieder einstellt (s. A. 5.3.1). Dieser Effekt tritt in verschiedenen Frequenzbändern auf. Zweitens ein anomaler $I_c(B)$ Verlauf um $14.1(3)\,\mathrm{GHz}$, bei dem $I_c(B)$ um $B = 0\,\mathrm{T}$ zwar am stärksten ist, für kleine $0\,\mathrm{T} < B \lesssim 20\,\mathrm{mT}$ aber ungewöhnlich schnell reduziert wird, bevor I_c bei weiter steigenden B-Feldern so monoton abnimmt, wie man es für eine orbitale Cooperpaar-Aufspaltung erwarten würde (siehe Abschnitt 5.3.2). Die dritte Beobachtung ist ein nicht-stetiger Sprung in $I_c(B)$ bei B-Feldern weit über der Koerzitivfeldstärke von Co, die etwa $5\,\mathrm{mT}$ beträgt (s. A. 5.3.3). In Abschnitt 5.4, kann ein B-Feld-abhängiger Frequenzgang der MW-Verkabelung als triviale Ursache für das außergewöhnliche $I_c(B)$-Verhalten ausgeschlossen werden. In Abschnitt 5.5 wird eine temperaturabhängige Erhöhung von I_c bei $B \neq 0\,\mathrm{T}$ beobachtet, die in fJJ auftritt, deren F entweder eine statische, oder dynamische inhomogene Magnetisierung aufweisen. Die Ursache des außergewöhnlichen $I_c(B)$-Verlaufs kann nicht eindeutig geklärt werden, wird in Abschnitt 5.6 aber diskutiert. Der Abschnitt 5.7 zeigt Ergebnisse einer T-abhängigen Hysterese des Widerstandes, bevor im letzten Abschnitt 6 die Dissertation zusammengefasst wird.

Contents

Zusammenfassung **I**

1 Introduction **1**
1.1 Motivation . . . 1
1.2 State of the Art . . . 1

2 Fundamentals **5**
2.1 Superconductivity . . . 5
2.1.1 Diffusion Constant . . . 7
2.1.2 Critical Current . . . 8
2.1.3 Superconductor in an External Magnetic Field . . . 8
2.1.4 Geometry Dependence of Superconductivity . . . 10
2.2 Josephson Junction . . . 11
2.2.1 Flux Quantization in a Josephson Junction . . . 12
2.2.2 RCSJ Model of a Josephson Junction . . . 12
2.3 Microwaves . . . 14
2.4 Magnetism . . . 15
2.5 Microwaves, Magnetism and Superconductivity . . . 19
2.5.1 Proximity Effects in S-F-Heterostructures . . . 19
2.5.2 Ferromagnetic Josephson Junction under MW Irradiation . 20

3 Experiment **23**
3.1 Samples and their Preparation . . . 23
3.2 Setup . . . 33
3.2.1 Cryogenics . . . 33
3.2.2 Electronics . . . 33

4 Static Transport **39**
4.1 Fundamental Sample Characterization . . . 39
4.2 Transport Characteristics . . . 41
4.3 Correlating Transport Features to Geometry . . . 49
4.4 Temperature Dependence . . . 52
4.5 Magnetic Field Dependence . . . 54

5 Dynamic Transport **61**
5.1 MW Induced Heating . . . 61
5.2 Microwave Stimulated Superconductivity . . . 65

5.3 Unusual Critical Current Behavior 72
5.3.1 Non-Monotonous Critical-Current-vs-B-Field Dependence 72
5.3.2 Anomalous Critical-Current-vs-B-Field Dependence 76
5.3.3 Discontinuous Critical-Current-vs-B-Field Dependence . . 84
5.4 Microwave Response 91
5.5 Non-Monotonous Critical Current vs Temperature 91
5.6 Discussion 93
5.7 Hysteretic Resistance vs Temperature 95

6 Conclusion **101**

References **104**

Abbreviations

abbreviation	meaning
Al	aluminum
Co	cobalt
S	superconductor
SC	superconductivity
sc	superconducting
F	ferromagnet
FM	ferromagnetism
FMR	ferromagnetic resonance
N	normal conductor/conducting state
JJ	Josephson junction
fJJ	ferromagnetic Josephson junction
WG	wave guide
MW	micro wave
B	magnetic flux density (B-field)
R_N	normal state resistance
$R_{(\mathrm{res})}$	(residual) resistance
J_c	critical current density
I_c	critical current
I_r	re-trapping current
ξ_0	BCS coherence length
ξ_D	diffusive SC coherence length
D	diffusion constant
QP	quasiparticle
I-V	current-voltage curve
dG	differential conductance
LRT	long-range (spin) triplet
SRT	short-range (spin) triplet
SOC	spin orbit coupling
BW	bandwidth

1 Introduction

1.1 Motivation

In order to meet the growing demand for computing power and data storage, new methods must be found to reduce the energy consumption of conventional electronic and spin based semiconducting systems. Spin based computation is called spintronics, in reference to electronics. Superconductors, with their dissipationless charge transport, seem like an obvious replacement for semiconductors at first glance. However, they do not carry any spin information under normal conditions. The interplay of the normaly opposing effects of superconductivity and ferromagnetism includes the possibility of the formation of superconducting Cooper pairs with finite spin. This is the novel field of superconducting spintronics on which most quantum computers are based [1]. Dissipationless computing seems within reach, especially since quantum computing becomes more energy efficient than conventional computing [2, 3]. This dissertation aims to contribute to the field of superconducting spintronics with investigations on superconductor (S)-ferromagnet (F)-heterostructures under microwave (MW) irradiation.

1.2 State of the Art

Heike Kamerlingh Onnes discovered superconductivity (SC) in 1911 [4, 5], and the first microscopic theory on conventional SC was presented by Bardeen, Cooper and Shrieffer in 1957 [6]. Their so called BCS theory describes a phonon mediated attractive force between two oppositely spin polarized electrons leading to a dissipationless charge transport without any spin information. These bosonic pairs of electrons are called "Cooper pairs", named after their first describer Cooper [7]. Since then exotic superconducting (sc) states where discovered, like sc equal-spin electron pairs with an overall spin of 1 (spin triplets). Spin triplets can be introduced in a S by an adjacent F due to proximity effects, which were theoretically described by Bergeret, Volkov and Efetov [8] and independently by Yagovtsav, Pugach and Eschrig [9]. Such a spin polarization in a S was probed by Salikhov et al. [10] in ferromagnetic resonance (FMR) measurements. Unlike conventional Cooper pairs with spin 0, spin triplets can sustain the exchange field in a F, leading to the possibility of sc spintronics. Theoretically sc spin triplets can be generated in various ways.

One method is to fabricate a spatially inhomogeneous magnetization at the

S-F interface which was originally proposed by Houzet and Buzdin [11] and reviewed by Eschrig [12] and Linder [13]. Such interfaces are called "magnetically active interfaces" and can be made, for example, out of a trilayer of Ho-Co-Ho. The magnetization turns in the Ho layers. Long-range triplet (LRT) SC through such a trilayer was experimentally observed by Robinson et al. [14]. Alidoust and Linder [15] calculated the LRT formation at such a Ho-Co-Ho trilayer and predict a similar sc singlet-to-LRT conversion at S-F-S junctions hosting either a Bloch or a Néel domain wall. A direct spectroscopic proof of LRT at a tunable inhomogeneous magnetization at a S-F interface was provided by Diesch et al. [16]. Experiments conducted by Fermin et al. [17] on disc-shaped ferromagnetic Josephson junctions (fJJ), without a purposely created magnetic active interface, lead to the hypothesis that magnetic vortex states created by the F in combination with the disc geometry can form LRTs. Control experiments on bar-shaped geometries by the same group rule out the vortex theory as a sufficient condition [18].

It appears that a combination of SC with a F can lead to LRT SC without special effort by implementing a magnetically active interface. Keizer et al. [19] showed a long-range supercurrent through a strongly spin-polarized CrO_2 barrier of thicknesses between 0.3 µm to 1 µm. Their sample consists of two sc NbTiN electrodes placed on top of a CrO_2 layer. The distance of the electrodes defines the F gap. This plain S-F-interface has no purposely engineered active magnetic interface. They even report a single domain magnetization of the CrO_2 whose magnetization direction changes the critical current (I_c) by 30%. Equivalent measurements on a 700 nm CrO_2 gap separating two sc $Mo_{70}Ge_{30}$ leads, were performed by Anwar et al. [20]. The actual mechanism forming LRT at a plain S-F interface is unknown to date. Possible explanations are a magnetic inhomogeneity naturally formed at the interface between S and F or a spin-triplet formation due to a combination of a homogeneous magnetization and spin orbit coupling (SOC), which was theoretically investigated by Bergeret and Tokatly [21] and by Eskilt et al. [22]. Bergeret and Tokatly introduce SOC by a lack of inversion symmetry and Eskilt et al. by an intermediate heavy metal layer between S and F.

All aforementioned experimental and theoretical findings and explanations for a LRT formation were based on static magnetizations. Another method to form LRT could be a dynamic singlet-to-triplet conversion by FMR, as proposed by Houzet and Buzdin [11] and Takahashi et al. [23]. The FMR frequencies are typically in the few GHz range and thus can be generated by the alternating magnetic field component of microwaves (MW). In experiments of Petcović et

al. [24] a FMR induced in a fJJ is reflected as a minimum in the current-voltage curve (I-V). A reduction of the line width of a FMR in a F adjacent to a S was observed by Jeon et al. [25] and interpreted as an enhanced spin flow into the S compared to the normal (N) conductive state of the superconductor.

Bobkova, Bobkov and Silaev [26] propose a singlet-to-LRT conversion stimulated by the alternating electric field component. Up to now, no experimental evidence for a dynamic LRT creation were published.

Further theoretical investigations on the interplay of MW and S-F structures have been reported by Hikino et al. [27, 28]. They show a modification of the Shapiro steps [29] under the influence of FMR and how the aspect ratio of a fJJ alters the Fraunhofer pattern. Both are transport characteristics which should be measurable but, to our knowledge, they have not been so far.

This thesis presents a variety of physical phenomena, which are brought about by the interplay of S, F and MWs. First, a brief overview of fundamentals in the context of S, F and MW is presented in section 2. The preparation of the samples and their structure is presented in section 3.1, followed by the description of the measurement set up in section 3.2. Section 4 deals with transport measurements without MW applied, where basic characterizations of the S-F-heterostructures are presented in section 4.1 and 4.2. The influence of the temperature T and of a magnetic field B is discussed in section 4.4 and 4.5, respectively.

Measurements conducted under MW irradiation are presented in section 5, starting with MW-induced heating in section 5.1 and MW stimulated SC in section 5.2 which was first observed in 1966 by Wyatt et al. [30] and by Dayem and Wiegand [31] and was theoretically explained by Eliashberg [32] in 1970. The topic is reviewed by Zolochevskii [33].

Section 5.3.1 shows a non-monotonous behavior of the critical current I_c with respect to a B-field under MW irradiation. A similar effect was first observed in 1974 by McCarthy and Warman [34] and has never been reported afterwards.

More recent publications show non monotonous $I_c(B)$ behavior without MW irradiation. Uranium based S, which are ferromagnetic (FM) and SC under pressure at the same time [35, 36], show re-entrant SC for B-fields much higher than the critical field B_c [35–39]. The $R(B)$ characteristics in this unusual S show a suppression of the SC for finite B-fields with a re-entrant SC at high B-fields. Rosul et al. [40] and Kinjo et al. [41] even suggest that the different sc phases in the uranium based S are formed by different pairing mechanisms. Esin et al. [42] show a suppression of the SC around zero B-field measured in an In-GeTe-

heterostructure. GeTe is a topological ferroelectric semimetal [43, 44] and In a conventional s-wave S. They model their system as a SFN junction in combination with SOC and their results are comparable to the non-monotonous $I_c(B)$ behavior presented in section 5.3.1.

The I_c of a conventional S of type I or type II decreases slowly for low B-fields and drops faster for B-fields close to B_c, as summarized by Meservey and Douglas [45] in 1964 for aluminum. In contrast to that, section 5.3.2 shows an anomalous $I_c(B)$, and section 5.3.3 a discontinuous $I_c(B)$ behavior. The latter can be seen in a publication of Quay et al. [46] but without any explanation of its origin. They actually report an enhancement of I_c under MW irradiation at frequencies of the quasiparticle spin resonance in the GHz range.

In section 5.7, a MW-mediated hysteresis of the resistance R with respect to a temperature change is presented. To our knowledge such a hysteresis has never been reported in the framework of SC and F but was observed in a metallic two dimensional electron gas (2DEG) formed at the interface of the two insulators $LaAlO_3$ and $SrTiO_3$ in combination with an applied backgate voltage V_{BG}. This was published by Minhas et al. in 2017 [47], Yan et al. in 2020 [48] and Kwak et al. [49].

2 Fundamentals

SC and ferromagnetism (FM) are two types of macroscopic quantum states consisting of a special energetic arrangement of electrons and their spins. They can be described by a macroscopic wave function or a magnetization, respectively, without having to know each specific state of a single electron in the respective system. Normally the two states of a S and a F are mutually exclusive but can be combined in a way that new physical phenomena emerge. The study of the S-F-heterostructure in the present work shall contribute another insight to some of the possible effects arising form the combination of S, F and a MW irradiation and a magnetic field (B-field). To understand the quite complex transport measurements, a separate overview on the components is given beforehand.

2.1 Superconductivity

Many materials can become superconducting when cooled below a specific critical transition temperature T_c. In the present work Al is chosen as the S for our S-F-heterostructures, because of sc Al can be described as a BCS S. Impurities in Al even enhance its superconducting properties and bulk $T_c = 1.175\,\mathrm{K}$ for clean Al [50] is well above the temperatures (T) we are able to achieve in our laboratories. Its sc properties do not only depend on impurities, but also on the geometry. T_c rises for films thinner than $\approx 100\,\mathrm{nm}$. For Al layers around $50\pm10\,\mathrm{nm}$ thickness T_c varies from 1.4 K to 2.1 K for grain sizes from 16 nm down to 4 nm [51–53]. For a bare S the transition from a N to a sc state is quite abrupt. In the case of S-F heterostructures the transition can happen continuously and with multiple steps in the resistance $R(T)$. In this thesis, T_c shall be defined as the temperature where the onset of SC is observed. Mostly this transition is monitored by an onset of a resistance decrease.

In a S two electrons of opposite spin and momentum are correlated on a length scale of the superconducting coherence length ξ to a bosonic particle called Cooper pair. The whole superconducting state, consisting of coherent Cooper pairs, can be described by a macroscopic wave function

$$\psi(\theta) = \sqrt{n_S}\exp i\theta \tag{1}$$

with a global phase θ and the superconducting particle density $n_S = |\psi|^2$. Any S is characterized by its gap energy $2\Delta(T)$. This is the minimum energy which

needs to be applied to break a Cooper pair. In turn, the energy of the sc state is reduced by $\Delta(T)$ per electron and SC thus becomes the preferred state of matter for $T < T_c$. An increase of the system's energy does not destroy SC as long as it is below $\Delta(T)$. According to the BCS theory, Δ can be expressed as

$$\Delta(T) = V \sum_k \kappa_k \left[1 - 2f(T, E_k)\right]. \tag{2}$$

V is the attractive potential between the two electrons and $\kappa_k = u_k \cdot v_k$ is the condensation amplitude. κ_k is determined by the probabilities v_k and u_k, that a state k is occupied by a Cooper pair or not, respectively. On the other hand, breaking a Cooper pair leads to an excitation that, with the probability of u_k, is of the form of an electron and, with the probability of v_k, is of the form of a hole. The probability amplitudes v_k and u_k are defined as follows.

$$v_k^2 = \frac{1}{2}\left(1 - \frac{\epsilon_k}{E_k}\right) \tag{3}$$

$$u_k^2 = \frac{1}{2}\left(1 + \frac{\epsilon_k}{E_k}\right) \tag{4}$$

The dispersion relation of such an excitation differs from the one of an electron and one speaks of a quasiparticle (QP) excitation of energy E_k.

$$E_k = \sqrt{\epsilon_k^2 + \Delta^2} \tag{5}$$

where ϵ_k is the kinetic energy contribution to the QP excitation that would correspond to a free electron near the Fermi energy.

$$\epsilon_k = \frac{\hbar^2}{2m}\left(k^2 - k_F^2\right) \approx \frac{\hbar^2 k_F}{m}\left(k - k_F\right) \tag{6}$$

Roughly speaking, the product $\kappa = u_k \cdot v_k$ is a measure of the amount of Cooper pairs around the Fermi level, determining Δ in the way given by equation (2).

$\Delta(T)$ decreases from its saturation value $\Delta(0)$ at $T = 0\,\mathrm{K}$ and vanishes at T_c. Near T_c the temperature dependence can roughly be described by

$$\Delta(T) = \Delta(0) \cdot 1.74 \cdot \left(1 - \frac{T}{T_c}\right)^{1/2}. \tag{7}$$

Compared to the bulk, the gap energy gradually increases when lowering the thickness of an Al sheet. It can increase from 180 µeV up to 350 µeV [45]. The sc

coherence length for a clean S at low temperature is given by the BCS theory as follows.

$$\xi_0 = \frac{\hbar v_F}{\pi \Delta(0)} \tag{8}$$

with the reduced Planck constant $\hbar$ and the Fermi velocity $v_F = l/\tau$ where τ is the scattering time and l the mean free path of the electrons in the N state. For Al $v_F = 2.02 \cdot 10^6$ m/s [54]. This equation for ξ_0 holds true for pure S. ξ_0 is almost constant for temperatures far below T_c and diverges at T_c for increasing temperatures $\xi \approx (T_c - T)^{-1/2}$. Thin film S can in many cases be considered to be dirty, which means $l << \xi_0$. In a dirty S the coherence length is reduced as follows.

$$\xi_D = \sqrt{\frac{\hbar D}{\Delta}} \tag{9}$$

where D is the diffusion constant, explained in the next section 2.1.1. We use the letter ξ without any subscript for expressions valid for all definitions of the coherence length (ξ_0, ξ_D etc.). There is a correlation between ξ_0 and ξ_D [55]:

$$\xi_D(T) = 0.855 \frac{\left(\xi_0 l\right)^{1/2}}{\left(1 - \frac{T}{T_c}\right)^{1/2}} \tag{10}$$

For temperatures well below T_c this relation reduces to the simple form

$$\xi_D(T) = 0.855 \cdot \left(\xi_0 l\right)^{1/2}. \tag{11}$$

2.1.1 Diffusion Constant

To estimate if our samples, consisting of Al, act as a S of type II due to geometrical confinements, we calculate ξ_D from equation (9) by means of the diffusion constant D of the normal conductive state of Al. D in general is the product of the charge carrier velocity v_F, the scattering time τ or the mean free path l.

$$D = \frac{1}{3} v_F^2 \tau = \frac{1}{3} v_F l \tag{12}$$

Besides that, D is related to the charge carrier mobility $\mu = |e|\tau / m_e$ by means of the Einstein relation [56]

$$D = \frac{k_B T}{e}\mu. \tag{13}$$

k_B is the Boltzmann constant and μ is related to the conductivity σ by the electronic charge carrier density n as follows.

$$\sigma = n \cdot e \cdot \mu = \frac{1}{\rho} \tag{14}$$

σ can experimentally be determined easily by the resistivity $\rho = R \cdot A/L$ with the resistance R and the length L and cross section A of the sample. Substituting equation (14) into the Einstein relation (13), leads to a handy equation that allows to calculate D of the electrons at the Fermi energy E_F from the conductance σ in the following way.

$$D = \frac{E_F}{ne^2}\sigma. \tag{15}$$

2.1.2 Critical Current

For the present thesis, the critical current I_c, at which a S turns normal conducting, is a key measurement parameter. The critical current I_c, which flows perpendicular through the sample cross section A, is the critical current density J_c and for a clean superconductor related to the superconducting gap energy Δ as follows.

$$J_c = \frac{ne\Delta}{\hbar k_F} \tag{16}$$

n is the particle density, e the elementary charge and k_F the Fermi wave vector. The measurable I_c hence is a direct indicator for the S state.

2.1.3 Superconductor in an External Magnetic Field

SC is weakened for an increasing B-field until the S becomes completely normal conducting at the critical magnetic field B_c. This value is a material property of any S but can increase due to the S's geometry or to the B-field direction with respect to the geometry. A B-field penetrates a dirty S on the length scale of the sc penetration depth λ.

$$\lambda = \lambda_L \sqrt{\frac{\xi_0}{l}} \tag{17}$$

where λ_L is the London penetration depth defined as

$$\lambda_L = \sqrt{\frac{m_e}{\mu_0 e^2 n_e}} \tag{18}$$

with the electron mass m_e, the vacuum permeability $\mu_0 \approx 4\pi \cdot 10^{-7}\mathrm{N/A^2}$, the elementary charge e and the electron density n_e. For bulk Al at low temperatures the experimental value is $\lambda = 50\,\mathrm{nm}$, whereas the theoretical value is $\lambda_L = 10\,\mathrm{nm}$ [57]. The depth λ also defines the regions at the surface of S where screening currents flow. These currents create an oppositely oriented B-field which completely compensate the applied B-field in the interior of the S. A S thus behaves like a perfect diamagnet. This is called the Meissner-Ochsenfeld effect. A S of type I expels the B-field completely until the superconductivity breaks down abruptly at the thermodynamic critical field

$$B_c = \frac{\Phi_0}{2\pi\sqrt{2}\lambda\xi_D} \tag{19}$$

Φ_0 is the flux quantum defined by the Planck constant h and e as follows [57].

$$\Phi_0 = \frac{h}{2e} \approx 2.07 \cdot 10^{-15}\,\mathrm{Vs}. \tag{20}$$

Between the characteristic theoretical and experimental quantities of a S, the following relation exists [55]:

$$\frac{\xi_D}{\xi_0} = \frac{\pi}{2\sqrt{3}} \frac{B_c(0)}{B_c(T)} \frac{\lambda_L}{\lambda} \tag{21}$$

For low T where $B_c(T) \approx B_c(0)$ this relation reduces to the simple and handy form

$$\xi_D \cdot \lambda \approx \xi_0 \cdot \lambda_L \tag{22}$$

In contrast to a type I S, a type II S is capable of hosting quantized magnetic flux vortices in its interior, which are surrounded by screening currents. The magnetic flux per vortex is one Φ_0 and decreases on the length scale of λ from the vortex core. The core of the vortex is normal, the material around is superconducting. This is a consequence of the altered superconducting length scales compared to type I S. The Cooper pair correlation length ξ is reduced inversely proportional according to equation (22). These properties lead to a

general characterization of type I and type II S by the ratio between ξ_D and λ as follows

$$\text{Type I} \qquad \xi_D \gtrapprox \lambda \tag{23}$$

$$\text{Type II} \qquad \xi_D \lessapprox \lambda \tag{24}$$

Up to a critical field B_{c1} a S of type II behaves like a S of type I and is in the so called Meissner phase.

$$B_{c1} = \frac{\Phi_0}{4\pi\lambda^2} \ln \frac{\lambda}{\xi_D} \tag{25}$$

For increasing B-fields in the range of B_{c1} and B_{c2}, the number of flux vortices in S continuously increases. This state is called Shubnikov phase, and is reflected experimentally in a monotonously decreasing $J_c(B)$ until the superconductivity breaks down at

$$B_{c2}(T) = \frac{\Phi_0}{2\pi\xi_D^2(T)}, \tag{26}$$

and the hole S turns normal. Note that this holds true for a bulk S where the dimensions are bigger than λ. Bulk S are defined as type I ore type II by their material properties, whereas a type II behavior can emerge out of a type I material due to geometrical confinements, which is described in the following section.

2.1.4 Geometry Dependence of Superconductivity

If at least one dimension of a S is smaller than ξ_0, the effective ξ_D is reduced. This holds true for the samples under investigation in this thesis which have a flat stripe geometry. A correlation between two electrons cannot extend beyond the borders of the S. For the same reason l is reduced. If ξ_D reduces, λ must increase to satisfy relation (22). This leads to the fact that a geometrical confinement of a S of type I can evolve type II characteristics if $\xi_D \lessapprox \lambda$ is fulfilled. If a B-field is applied parallel with respect to the surface of a flat S with thickness d, the critical B-field increases as follows [55]:

$$B_c^{||} = 2\sqrt{6} \cdot B_c \frac{\lambda}{d} \tag{27}$$

All measurements in this thesis were performed with the parallel B-field configuration. Therefor $B_c^{||}$ is abbreviated as B_c for the sake of simplicity, unless stated differently.

2.2 Josephson Junction

Two superconductors (S_1 and S_2) connected by a tunnel barrier or a weak link, like a normal metal or a constriction, form a Josephson junction (JJ). Our samples are made out of two different S bars sandwiching a ferromagnetic layer leading to a variety of possible weak links, described in the following sections. Between the two S forming a JJ, the Josephson current

$$I = I_c \sin\phi \tag{28}$$

flows, even without an applied voltage; this is called the dc Josephson effect. It depends on the phase difference $\phi = \theta_1 - \theta_2$ between the two wave functions expressed in equation (1) of S_1 and S_2. I_c is the critical current of a JJ. Although, equation (28) was originally predicted for tunnel junctions by Josephson [58], it holds true for any weak link JJ [55].

For a JJ formed by two identical S separated by a tunnel contact, the critical current can be calculated from the normal state resistance R_N with the equation of Ambegaokar and Baratoff

$$I_c \cdot R_N = \frac{\pi\Delta(T)}{2e} \tanh\left(\frac{\Delta(T)}{2k_B T}\right), \tag{29}$$

which holds true for metallic weak link JJs at $T \to T_c$ [55]. For tunnel junctions and at low temperatures $T \to 0$, equation (29) can be used to estimate the expected critical current as follows.

$$I_c(0) = \frac{\pi\Delta(0)}{2eR_N} \tag{30}$$

If a finite voltage V is applied to the JJ, the phase ϕ changes in time t

$$\frac{\mathrm{d}\phi}{\mathrm{d}t} = \frac{2eV}{\hbar} \tag{31}$$

$$\Rightarrow \phi(t) = \phi(0) + \frac{2eV}{\hbar} t \tag{32}$$

and causes an alternating current with the Josephson frequency $\omega_J = 2eV/\hbar$. The JJ current oscillates with 483 MHz per µV. This phenomenon is called the ac Josephson effect.

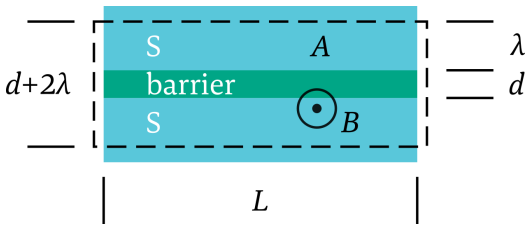

Figure 1: Schematic of a Josephson junction (JJ) interface with superconductors S separated by a barrier of thickness d. The dashed line frames the effective Josephson area $A = (d + 2\lambda) \cdot L$ where magnetic flux penetrates the JJ's interface on the length scale of λ.

2.2.1 Flux Quantization in a Josephson Junction

Magnetic flux Φ in a Josephson junction alters the critical current I_c. For a rectangular interface, depicted in figure 1, the critical current varies like a Fraunhofer pattern with minima at integer multiples of a flux quantum Φ_0 introduced in equation (20), except for $B = 0\,\mathrm{T}$ where a maximum occurs. The magnetic flux in general is defined as the are integral over the magnetic flux density $\boldsymbol{B}$ penetrating the area A as follows.

$$\Phi = \iint_A \boldsymbol{B}\,\mathrm{d}\boldsymbol{A} \tag{33}$$

The area $A = (d+2\lambda) \cdot L$ of the JJ's interface, which is penetrated by the magnetic field B, is defined by the barrier thickness d and length L and by the penetration depth λ. Figure 1 illustrates the geometry and relevant lengths. Assuming a homogeneous B-field penetrating the interface of the JJ perpendicularly reduces formula (33) to $\Phi = B \cdot A$ like shown in figure 1. Hence, the magnetic field at which the critical current reaches its first minimum is $B_0 = \Phi_0 / A$.

2.2.2 RCSJ Model of a Josephson Junction

A JJ in practice has in addition to equation (28) a capacitance due to the two S separated by a barrier and a resistive quasiparticle current. The current flow over a physical JJ thus can be modeled by a circuit of a parallel resistance R, capacitance C and the idealized JJ (equation 28) as depicted in figure 2(a). The individual current components over the circuit parts of a JJ are

$$I_J = I_c \sin\phi(t); \quad I_R = \frac{V(t)}{R}; \quad I_C = C\frac{\mathrm{d}V(t)}{\mathrm{d}t}; \quad V = \frac{\hbar}{2e}\frac{\mathrm{d}\phi(t)}{\mathrm{d}t}. \tag{34}$$

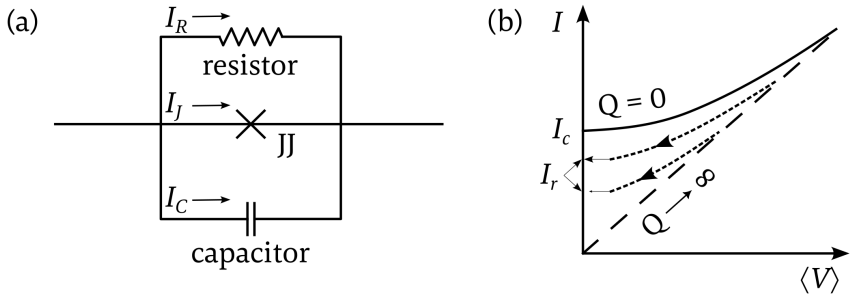

Figure 2: (a) Resistively and capacitively shunted junction (RCSJ) model of a JJ with a parallel current over a resistor I_R and over a capacitance I_C. (b) critical current I_c of a JJ and the re-trapping current I_r vs mean voltage $\langle V \rangle$ for different quality factors $Q = \omega_p RC$ of the JJ.

These currents through the JJ are superimposed and form the total current as follows.

$$I(t) = I_c \sin\phi(t) + \frac{\hbar}{2eR}\frac{\mathrm{d}\phi(t)}{\mathrm{d}t} + \frac{\hbar C}{2e}\frac{\mathrm{d}^2\phi(t)}{\mathrm{d}t^2} \tag{35}$$

The superconducting Josephson current is now shunted by a resistance R and a capacitance C giving this model the name "resistively and capacitively shunted junction" (RCSJ) model. By introducing the dimensionless time variable $\tau = \omega_p t$ with the plasma frequency

$$\omega_p = \sqrt{\frac{2eI_c}{\hbar C}}, \tag{36}$$

the current-phase relation in equation (35) can now be written as follows.

$$\frac{I}{I_c} = \sin\phi(t) + \frac{1}{Q}\frac{\mathrm{d}\phi(t)}{\mathrm{d}t} + \frac{\mathrm{d}^2\phi(t)}{\mathrm{d}t^2} \tag{37}$$

with the quality factor of the JJ

$$Q = \omega_p RC. \tag{38}$$

*I-V*s for different Q values are qualitatively depicted in figure 2(b). The upper solid curve represents the current voltage curve for a JJ when the bias current is swept from low to high values (up sweep). For a $Q = 0$ the current voltage behavior is the same when the bias current is swept from high to low values

(down sweep). A JJ with $Q = 0$ is called an over-damped junction. The important case for the present thesis is an under-damped JJ with $Q \neq 0$. In such a case numerical solutions of equation (35) provide the dotted lines in figure 2(b). If Q is large, R and C are large, respectively, The I-V curves of the down sweep (dotted lines) differs from the up-sweep curve (solid line). The $V = 0\,\mathrm{V}$ state of the under-damped JJ is not reached until the bias current drops below the so-called re-trapping current $I_r < I_c$. If the bias current is sweeping up again, the under-damped JJ reaches the resistive current branch for bias currents larger than I_c. A hysteretic I-V loop between the solid line and one of the dotted lines is formed. The amplitude of I_r is determined by Q. There is a correlation between the re-trapping current I_r of an under-damped Josephson junction and the damping Q [55].

$$I_r = \frac{4}{\pi Q} I_c \tag{39}$$

2.3 Microwaves

The electromagnetic spectrum between 300 MHz and 300 GHz is called microwave radiation. In our experiments we work with frequencies from 1 GHz to 30 GHz which correspond to photon energies of 4.1 µeV to 124 µeV. We are interested in the alternating magnetic field component of the MW to stimulate FMR. A simple picture to describe the propagation of the alternating magnetic field component of a MW, is a plane wave.

$$\boldsymbol{b}(r,t) = \boldsymbol{b}\mathrm{e}^{i(\boldsymbol{k}\cdot\boldsymbol{r}-\omega t)} \tag{40}$$

with amplitude $\boldsymbol{b}$, wave vector $\boldsymbol{k}$ and angular frequency ω at time t and at site $\boldsymbol{r} = (x, y, z)$.

To work with MWs in a practical manner, the MW propagation is treated on a logarithmic scale to the base 10. The unit of the MW power is then given in dBm which is the ratio of the power with respect to 1 mW as follows.

$$P[\mathrm{dBm}] = 10 \cdot \log_{10}\left(\frac{P[\mathrm{mW}]}{1\,\mathrm{mW}}\right) \tag{41}$$

To calculate the MW power in units of mW one simply has to invert the former equation.

$$P[\mathrm{mW}] = 1\,\mathrm{mW} \cdot 10^{\frac{P[\mathrm{dBm}]}{10}} \tag{42}$$

If a transmission measurement is performed, the output is a scattering parameter, or short S-parameter, S_{12} or S_{21}, in units of dBm. The two indices stand for the two sides of a device under test (DUT) in a two-terminal MW measurement circuit. S_{ij} relates an incident wave from side i and the transmitted wave at side j. S_{ii} (S_{jj}) hence relates the incident wave from side i (side j) with the reflected wave at the same side i (j). The quantity of interest actually is the so called "frequency response", or shortly "damping" of the incident MW. The damping in units of dB is calculated from the S-parameters in the following form.

$$A[\mathrm{dB}] = 20 \cdot \log_{10}\left(|S_{ij}|\right) \tag{43}$$

For a simple DUT, like a single-line microwave cabling, the S-parameters S_{12} and S_{21} are equivalent. Dealing with a logarithmic scale such as dBm may appear unhandy but has some advantages. The transmitted MW power is simply the power of the incident MW subtracted by the measured damping in the following form.

$$P_{\mathrm{out}}[\mathrm{dBm}] = P_{\mathrm{in}}[\mathrm{dBm}] - A[\mathrm{dB}] \tag{44}$$

For a DUT of homogeneous damping, like an ideal coaxial cable, the damping through half of the cable is simply half the measured damping $P_d[\mathrm{dBm}]/2$. In the case of the present work, where a nominally symmetric two terminal wiring on a wave guide (WG) is installed, the MW power at half of the way of the cabling, namely at the WG, can be calculated by the former two simple equations. This, however, can just be a simple estimation since the real cabling will never be perfectly symmetric due to joints of plugs and soldering connections, windings of the cables and so on.

2.4 Magnetism

Like superconductivity, magnetism is a macroscopic quantum state and can be expressed by the single quantity of magnetization $\boldsymbol{M}$.

$$\mu_0 \boldsymbol{M} = \chi \boldsymbol{B} \tag{45}$$

with the vacuum permeability μ_0 and the magnetic flux density $\boldsymbol{B}$, which is called throughout this thesis "magnetic field" or "B-field" for simplicity. The material specific magnetic susceptibility χ determines how much an external B-field magnetizes a material. For low B-fields and for ellipsoidal para- and

diamagnetic solids, where a $\boldsymbol{M}$ emerges parallel or antiparallel with respect to a B-field, χ is a constant value at a fixed temperature.

The magnetic material in the case of our samples is ferromagnetic Co. Ferromagnetism is characterized by a spontaneous magnetization without an external B-field. The spontaneous magnetization sets in below a transition temperature named Curie temperature T_{Curie}. Below T_{Curie}, χ is a complicated coefficient and becomes constant for a fixed $T > T_{\text{Curie}}$. For Co $T_{\text{Curie}} = 1388\,\text{K}$. The ferromagnetic magnetization has a upper saturation limit. The saturation magnetization M_s of Co is 140 mT to 145 mT at room temperature and 0 K respectively [54]. A ferromagnet can be demagnetized by applying a so called coercive B-field of opposite polarity compared to the magnetization direction. The coercive field of Co is of the order of 2 mT to 6 mT, depending on T and the geometry [59–62].

FM ordering occurs when the state of parallel atomic magnetic moments is energetically favorable. The atomic moment arise from a combination of orbital electron motions and their spins. This can be expressed by a positive exchange coupling J_{ex} between neighboring magnetic moments ($\boldsymbol{s}_1, \boldsymbol{s}_2$), resulting in a reduction of the energy per atom as follows.

$$E_{ex} = -J_{ex}\boldsymbol{s}_1\boldsymbol{s}_2 \tag{46}$$

E_{ex} is called exchange energy and is the relevant energy scale for FM, in analogy to sc gap energy Δ as the relevant energy scale for SC.

Co is known to form Bloch domain walls in bulk which transit into Néel domain walls for layers thinner than 30 nm [63]. The magnetization between two adjacent Néel domains turns in-plane and thus has no out-of-plane magnetization component in a perfectly flat Co layer. Considering the grain size of the underlying Al layer, our Co layers are most likely not perfectly flat. The thickness of domain walls in Co are of the order of 15 nm to 25 nm for a Co sample length of 10 nm to 1 µm, respectively. This means, there is a critical sample length below which just a single domain forms. For an aspect ratio of the length to the width of a flat Co structure of 2 to 10, the critical sample length is around 50 nm to 250 nm respectively [64]. The Co strip in our S-F heterostructures has a nominal geometry of 5 µ × 200 nm × 12 nm. In summary, we assume Néel domain walls to be formed just along the long axis of the Co strip. For Co thicknesses of less than five atomic layers an out-of-plane magnetization component emerges [65]. For such a thin Co, the spin polarization is around 30% and slightly rises to 34% for a thickness of 2 nm [59].

An alternating magnetic field component $\boldsymbol{b}(t)$ of MW couples to the magnetic moment of the spins in the F and alters the magnetization as a function of time $\boldsymbol{M}(t)$. The change of $\boldsymbol{M}(t)$ can be described by the Landau-Lifshitz-Gilbert (LLG) equation [66].

$$\frac{\mathrm{d}\boldsymbol{M}}{\mathrm{d}t} = \gamma[\boldsymbol{M}(t) \times \boldsymbol{B}(t)] + \frac{\alpha}{M_s}\left[\boldsymbol{M}(t) \times \frac{\mathrm{d}\boldsymbol{M}}{\mathrm{d}t}\right] \tag{47}$$

where α is the phenomenological Gilbert damping parameter, γ the gyromagnetic ratio and $\boldsymbol{B}(t) = \boldsymbol{B} + \boldsymbol{b}(t)$ with the static B-field $\boldsymbol{B}$. Hikino et al. [28] solved the LLG equation for a circular polarized $\boldsymbol{b}(t)$ propagating in z-direction leading to the time dependent absolute magnetization

$$M(t) = \frac{\gamma M_z b}{\omega - \omega_0 - i\alpha\omega} \mathrm{e}^{+i\omega t}. \tag{48}$$

The magnetization is now driven by the alternating $\boldsymbol{b}(t)$-field of frequency ω and describes a precession of $M(t)$ around the B-field pointing in z-direction. ω_0 is the material specific ferromagnetic resonance (FMR) frequency of the collective precession of the molecular magnetic moments. Taken together, the molecular magnets form $M(t)$. In the quantum mechanical picture this collective resonant motion of molecular magnetic moments is considered as a quasiparticle named "magnon" with quantized excitations $n\omega_0$. $M(t)$ gets maximal when $\omega = \omega_0$. On the other hand, MWs are absorbed by the F most strongly at ω_0. The band width of MW absorption around ω_0 (linewidth) is determined by the damping α of the magnetic system. In a S-F-heterostructure, a reduction of the linewidth can be a measure of the presence of S spin triplets [25] since the overall damping of the system is reduced in the presence of LRTs. On the contrary, the damping parameter α is enhanced for a spin singlet S in metallic contact to a F compared to α of a bare F [67]. In an increasing B-field, the FMR frequency ω_0 increases as described by the Kittel formula [68]

$$\omega_0 = \gamma\sqrt{(B + B_{\mathrm{ani}})(B + B_{\mathrm{ani}} + M_s)}. \tag{49}$$

B_{ani} is a potential anisotropy field and depends for example on the geometry, size and domain wall configuration of the F.

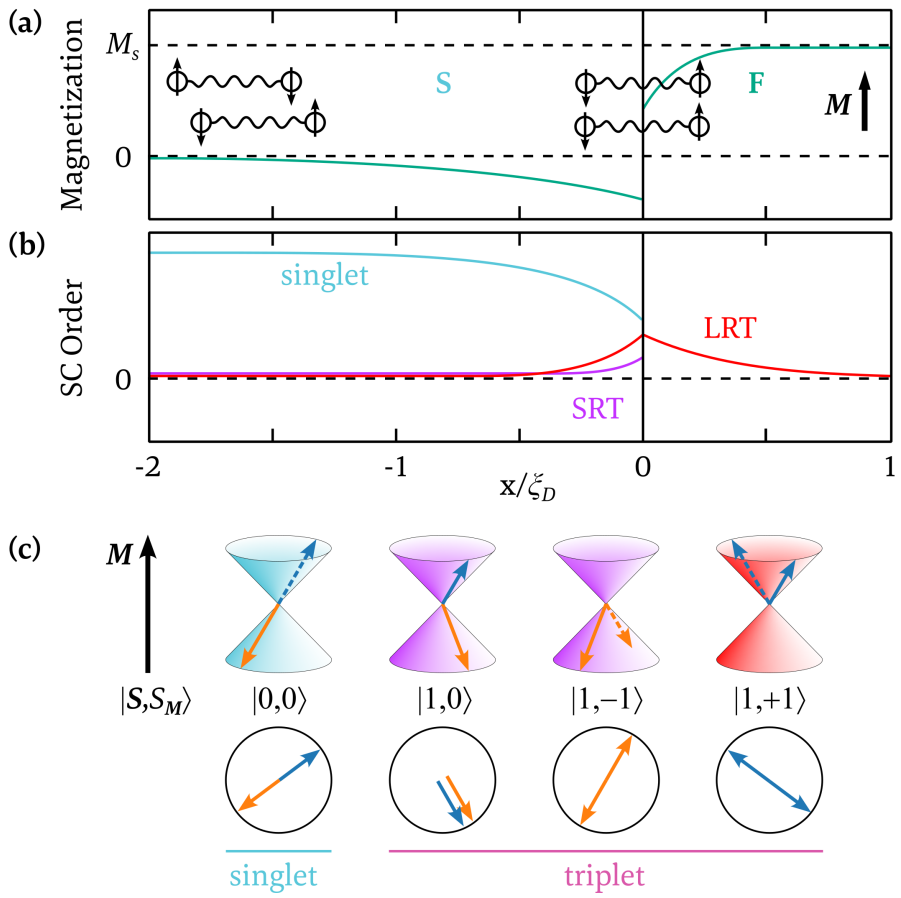

Figure 3: (a) Magnetic proximity effect in the superconductor (S) induced by the ferromagnet (F) with magnetization $\boldsymbol{M}$ and the saturation magnetization M_s in metallic contact to each other. (b) sc order parameter consisting of singlets in the bulk S. Short range triplets (SRT) and long range triplets (LRT) emerging at the S-F-interface. (c) Composition of Cooper pairs with respect to $\boldsymbol{M}$. Zero total spin ($S = 0$) with zero spin projection along $\boldsymbol{M}$ ($S_{\boldsymbol{M}}$) leads to the singlet sate $|0,0\rangle$. A total spin of $S = 1$ yields the two SRT states with either $S_{\boldsymbol{M}} = 0$ or $S_{\boldsymbol{M}} = -1$ and the LRT state with $S_{\boldsymbol{M}} = +1$. The triplet states with $S_{\boldsymbol{M}} = \pm 1$ require a spin flip event at the S-F-interface.

2.5 Microwaves, Magnetism and Superconductivity

2.5.1 Proximity Effects in S-F-Heterostructures

Bringing a S into close metallic contact with a normal metal N, the sc correlation is introduced in N over a length scale of

$$\xi^N(T) = \sqrt{\frac{\hbar D_N}{k_B T}}, \tag{50}$$

considering a diffusive system with the diffusion constant D_N in N. This is called the sc proximity effect. Replacing N with a F, the SC decays on the much shorter length scale

$$\xi^F(E_{\mathrm{ex}}) = \sqrt{\frac{\hbar D_F}{E_{\mathrm{ex}}}} \tag{51}$$

depending on the exchange energy E_{ex} in the F. According to Bergeret, Volkov and Efetov [8], those Cooper pairs, whose down electrons crossed the S-F interface, are suppressed in F at cost of a reduction of the absolute magnetization M in the layer depth $\xi^F(E_{ex})$ in F. The reduction of M is depicted in figure 3(a) with the green line deviating from the saturation magnetization M_s in F. The Cooper pairs with a spin-up electron in F persist as long as the down-spin counterpart is in S. These down spin electrons lead to a magnetization in the S which is opposite to $\boldsymbol{M}$. This magnetic proximity effect penetrates the S on the length scale ξ_D and is illustrated in figure 3(a) by the sketches of Cooper pairs and the green line in S which deviates from the zero magnetization line. One now can imagine a total suppression of SC in a thin S in close contact to a F. On the other hand, $\boldsymbol{M}$ in a thin F, which is sandwiched by two S, might be weakened to the extent that SC in the S layers is not suppressed completely. Both S-F combinations are present in our S-F-heterostructures, which are discussed in detail in the next sections.

At the S-F interface, the electrons of a Cooper pair experience a spin dependent phase shift. In consequence, the sc order parameter oscillates between spin-singlet Cooper pairs, with zero total spin ($S = 0$) and short-range spin triplets (SRT), which have a total spin $S = 1$ but their spin polarization along $\boldsymbol{M}$ is also $S_{\boldsymbol{M}} = 0$. The spin orientations along $\boldsymbol{M}$ of a singlet and a SRT with $S_{\boldsymbol{M}} = 0$ are depicted by the two leftmost illustrations in figure 3(c). A weakly spin-polarized F hosts such oscillations over the length scale of $\xi^F(E_{\mathrm{ex}})$ while they are heavily suppressed in a strongly spin-polarized F where $E_{\mathrm{ex}} >> \Delta$. Those

oscillatory states are called FFLO states, named after Fulde and Ferrell [69] and Larkin and Ovchinnikov [70]. For different literature values of $E_{ex} = 309\,\text{meV}$ from [71] and $E_{ex} = 32\,\text{meV}$ from [72] for Co, E_{ex} is two to three orders of magnitude higher than our measured $\Delta = 212\,\mu\text{eV}$, which leads to a coherence length in Co of at most $\xi^F(E_{\text{ex}}) = 3\,\text{nm}$ [71].

The phase shift in the S leads to a so called spin-mixing state at the S-F-interface composed of singlet and SRT states with $S_{\boldsymbol{M}} = 0$, indicated by the increase of the violet SRT curve in figure 3(b).

If a spin flip at the S-F interface happens, Cooper pairs with a magnetization projection along $\boldsymbol{M}$ can emerge. They are illustrated in figure 3(c) by the two rightmost sketches. States with antiparallel $S_{\boldsymbol{M}} = -1$ are also of the short range type with the decay length $\xi^F(E_{\text{ex}})$ in F, whereas Cooper pairs with $S_{\boldsymbol{M}} = +1$ survive in F over the length scale $\xi^N(T)$ and thus are called LRT. The cause for a spin flip can be an inhomogeneously magnetized S-F interface, by spin orbit scattering or by dynamic spin flip mediated by microwaves (MW).

2.5.2 Ferromagnetic Josephson Junction under MW Irradiation

The present thesis investigates the interplay of the sc Al, the ferromagnetic Co and MW irradiation. Particularly our S-F-heterostructures consist of bare Al parts, Al parts which are proximitized by the Co and of a fJJ where two layers of Al are sandwiching a Co layer. MWs consist of an alternating E-field and B-field component. Both of them have different impact on JJs.

An ac E-field of frequency ω couples to the JJ phase ϕ in such a way that the critical current step I_c in the current voltage characteristic of the JJ is reproduced at certain dc voltages when the condition $2eV/\hbar = n\omega$ is fulfilled. For example, a frequency of 483 MHz yields a jump in a I-V at integer multiples of 1 µV. These jumps in the current are called Shapiro steps.

Theory of Hikino et al. [28] predicts a change of the Shapiro steps when the frequency of an ac B-field matches the FMR frequency ω_0 of the F layer in a fJJ. The change of the Shapiro step heights is a signature of sc LRTs. The B-field frequency of $\omega = n\omega_0$ induces n magnons. Each of it is able to cause a spin flip scattering of Cooper pairs at a S-F interface because magnons are of bosonic nature with spin 1. A sc spin singlet which is scattered at a magnon, transits into the F as a LRT and the Josephson coupling vanishes if no second magnon scattering event would transform the LRT back to a singlet on the other side of the F barrier in the fJJ. An odd number of magnons hence suppresses the Josephson coupling. An even number of magnons even enhances the transport

of Cooper pairs over the F barrier. In consequence, the Shapiro step height is reduced at voltages corresponding to the energy of an odd number of magnons $V = n\hbar\omega_0/2e$ and enhanced at an even n. If the B-field frequency ω is detuned from the FMR frequency ω_0, the Shapiro steps remain as expected for an ac E-field irradiation.

3 Experiment

The following sections summarize the experimental components which are necessary to perform transport measurements on our S-F-heterostructures under MW irradiation and B-field. The first section 3.1 shows how the samples and the two methods of integrated WGs look like and how they are prepared. The second section 3.2 gives an overview of the experimental setup. It consist of a cryostat with dc measurement lines, a magnet and MW cabling.

3.1 Samples and their Preparation

The models for a theoretical consideration of a S-F-S junction normally assume two superconducting wires with perfectly square-shaped cross sections separated by a F spacer of a few nanometers thickness, like illustrated in figure 1. Within this work the best approach to this ideal picture was to use a shadow evaporation technique to separate two Al strips of thickness 50 nm by a thin Co spacer of nominally 12 nm thickness. The latter is reduced to around 1 nm to 2 nm due to geometrical reasons explained in the following. One end of each Al strip is attached to two Al leads, thus, the sample is connected in a four-point geometry. Figure 4(e) shows sample A1 with the aluminum leads as a representative for all samples, since they are fabricated with the same procedure. Figure 4(f) shows the cut out of figure 4(e) around the S-F-S heterostructure.

An 8 mm × 8 mm Si substrate with a Si oxide top layer hosts two samples. Before preparing the actual samples, macroscopic Au pads are created at the edges of the substrate with big Au leads which reach into the center of the substrate. This is depicted in figure 4(a). Photolithography is used to make the pads and big leads following the recipe in table 1.

The shape of the samples and the Al leads are defined by a mask whose shape is shown in figure 4(d). This shape is patterned into a two layer resist by electron beam lithography, illustrated in figure 5(a), (b) and (c). The corresponding recipes for coating, exposing and developing the two resists are shown in table 1. Figure 5(d), (e) and (f) show the principle of the three shadow evaporation steps needed to create the S-F-S heterostructure by metal vapor deposition. In figure 5(d) the first Al layer is coated by an incident angle θ which we varied from 40° to 35° during the evaporation process to create a ramp at the faces of the Al layer. This shall provide a continuous overlap of the two layers coated subsequently. The gray plane in the coordinate systems in figure 5 represents the plane which is perpendicular to the rotation axis of the sample

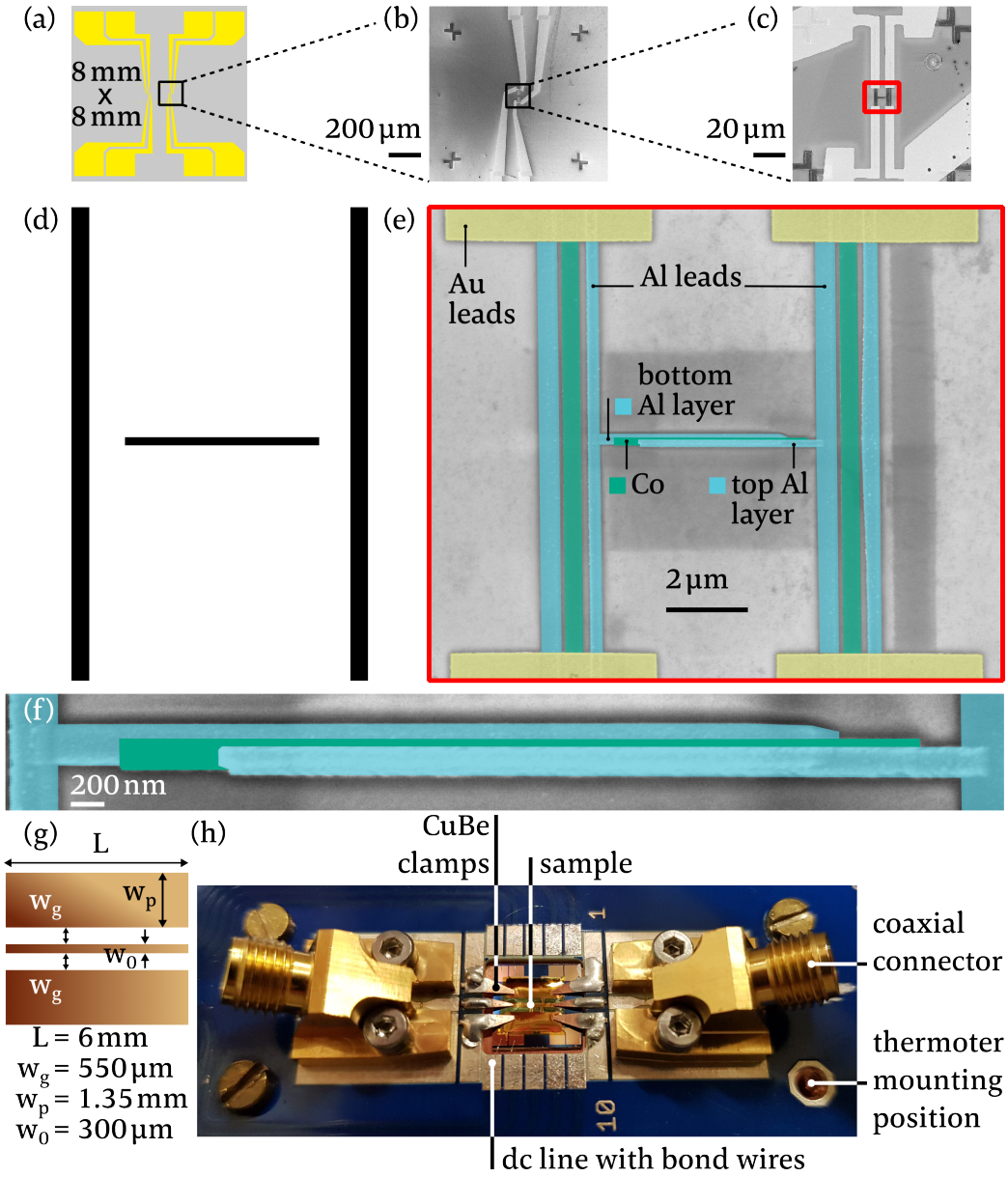

Figure 4: (a) Substrate with big Au leads. (b) Small Au leads and big markers (c) Small Au leads and small markers. Sample Al leads in red frame. (d) Template for photo resist mask. (e) Sample A1 (center part) (f) Sample section. (h) Sample holder with ac coaxial plugs and dc measurement lines.

holder in the metal vapor deposition chamber (evaporator) and thus is called rotation plane. The angle φ provides a diagonal shift of the single layers which is necessary to prevent the two Al layers from being shorted and is realized by turning the Si substrate on the sample holder by the angle φ. A more detailed explanation of the angular relations from the sample's point of view is given in the next paragraph. Figure 5(e) shows the vertical deposition of Co and figure 5(f) the coating of the top Al layer under an incident angle of $\theta = -40°$. After the coating, the sample gets immersed in acetone to remove the resist together with the residual metal coating on top of the resist. This is called the lift-off process and takes around 15 to 20 minutes. A subsequent rinsing of the samples with isoproyl alcohol (IPA) and a blowing-dry with nitrogen gas finalizes the preparation of the S-F-S heterostructures. A last photo lithography step connects the big Au leads (figure 4(a)) and the Al leads (figure 4(e)) with another set of Au leads which are shown in figure 4(b) and (c). The WG dimensions are depicted in figure 4(g) which is placed on top of the sample in figure 4(h). Figure 4(h) shows an image of the sample holder. The dc lines are connected to the big Au pads on the Si substrate with Al bond wires. The substrate is held by CuBe clamps which also act as electrical contacts of the coaxial connectors and the WG. The thermometer is mounted around 3 cm apart from the sample. The sample holder allows to connect the two samples on one substrate at the same time.

Shadow evaporation basically is a simple technique. However, the resulting S-F-S heterostructures are quite complex. Figure 6 provides a more realistic picture of how the the three layers are arranged with respect to each other. In figure 6(a) there is a schematical drawing of the first Al layer with top, front and side view. The side view is a sectional view along the line A-A (in the front view), the front view is a sectional view along the line B-B (in the top view). The slopes of the faces of the Al bar are true-to-scale, the length and width of the bar is not. The blue diagonal bar in the lower left is a true-to-scale model of the first Al layer. The coordinate system depicts the direction of the incident Al vapor beam (blue) and is equivalent to the coordinate system in the previous figure 5. The beam direction is rotated by the angle θ around a rotation axis which is perpendicular to the gray rotation plane. This rotation axis, thus, is twisted by the angle φ around the z-axis. Changing the angle θ from 40° to 35° during the evaporation process leads to the ramps at the faces of the bar. Figure 6(b) shows the deposition of the Co layer (green) with a vertical direction of incidence. In figure 6(c) the top Al layer coating is illustrated with an incident angle of $-\theta$. Having a close look on the side views in figure 6(b) and (c), one

Table 1: Recipe for the photolithography and the electron beam lithography steps.

Photolithography		
coating	resist	AR-P 5350
	spin coating	5000 rpm for 60 s
	post bake	hot plate 100°C for 4 min
exposing	device	mask aligner
	time	20 s
developing	developer	AR 300-26
	time	15 s
	post process	~30 s in DI water
electron beam lithography		
coating	bottom resist	MMA MAA EL11
	spin coating	2500 rpm for 90 s
	post bake	hot plate 150°C for 75 s
	top resist	PMMA A4
	spin coating	5000 rpm for 60 s
	post bake	hot plate 180°C for 75 s
exposing	acceleration voltage	20 kV
	aperture	10 µm
	dose	440 $\mu C \cdot cm^{-2}$
developing	developer	MIBK 1:3 IPA
	time	20 s
	post process	10 min in IPA

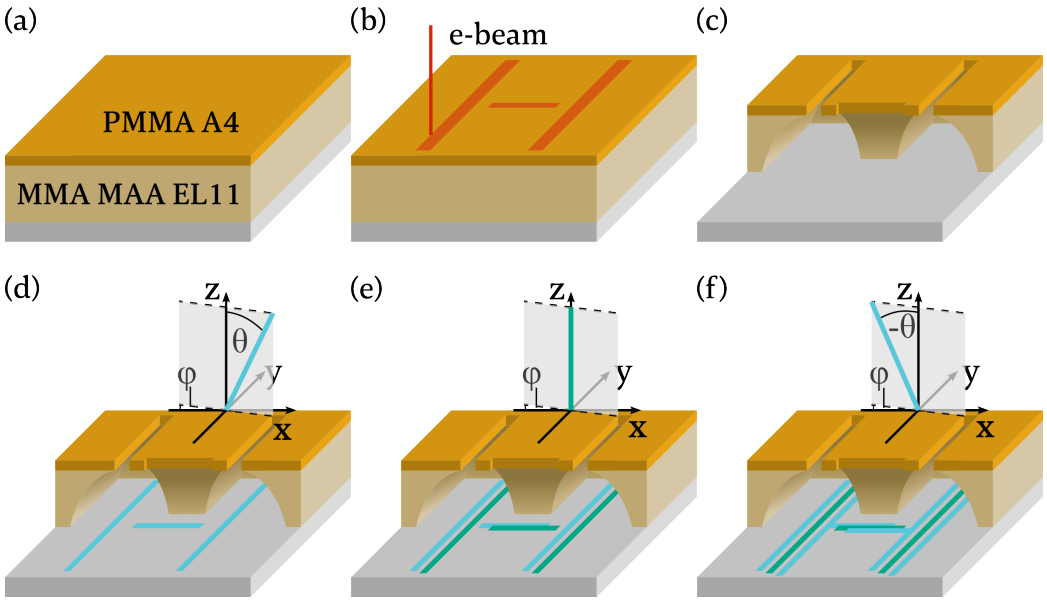

Figure 5: Electron beam lithography and metal vapor deposition with the shadow evaporation technique. (a) Two-layer resist on a Si substrate. (b) Electron beam patterning of the mask. (c) Developed and under-etched mask (sectional view). (d) Evaporation of Al (blue) under the angle θ whose rotation axis is twisted around the z-axis by φ. φ is obtained by rotating the sample by φ around the z-axis on the sample holder of the evaporator. (e) Perpendicular evaporation of Co (green). (f) Evaporation of Al (blue) under the angle $-\theta$.

can see a reduction of the Co layer thickness at the side face of the lower Al layer. A nominally 12 nm thick Co coating leads to a 1.5 nm Co spacer along the whole side face of the lower Al layer. This value was measured on the 3D model (true-to-scale model in figure 6), which was made out of the real geometrical conditions, like evaporation angles and layer thicknesses. The top view in figure 6(c) shows the diagonal shift of the three layers due to the rotation φ. This shift ensures a separation of the two Al layers by the Co spacer. A short between the two Al layers thus can be excluded by geometry. To achieve the angle φ in practice, one must first place the Si substrate with the long side of the sample structure (x-axis in figure 6) in the rotation plane (perpendicular to the rotation axis) of the evaporator before the substrate is rotated by around $\varphi = 5°$ out of this rotation plane.

The final step of the sample preparation is the integration of a WG. The WG consists of an inner conductor of width 300 µm. Two ground pads are placed with a distance of 550 µm on each side of the inner conductor. The shape of the WG can be seen in figure 7(e) in green and is patterned by means of photolithography. It consists of 50 nm Au with a 3 nm Ti bottom layer. Two different methods of integrating a WG were used. One is to pattern a WG on a Kapton™ foil and placing it on top of the substrate (ext. WG). The foil gets fixed together with the substrate by the CuBe clamps. The other method is to coat the substrate partially with an insulating layer and patterning the WG directly on top of that layer (int. WG). This process is depicted in figure 7. Sticky tape (figure 7(b) and (c) in blue) on the Au contact pads hinders the subsequently spin coated polyimide to cover the contact pads (figure 7(c) and (d) in orange). After the bake out of the polyimide in a vacuum oven, the WG can be patterned on top of the substrate by means of photolithography, like shown in figure 7(e). The sticky tape needs to have a very low adhesion to not lift off the Au pads while removing the tape. We chose a wafer dicing tape of type 1009 from the company Ultron Systems, Inc. For both methods of integrating a WG, the inner conductor has to be above the samples to ensure that the ac B-field direction is aligned perpendicular to the external B-field direction, as illustrated in figure 8.

The samples under investigation are listed in table 2 and SEM images of them are depicted in figure 9. The table 2 shows whether a WG on a Kapton™ foil was put on the substrate (ext. WG) or a integrated WG on a polyimide layer was used (int. WG). The values for T_c, B_c, I_c and R_N stem from the measurements discussed in the next sections. Sample A1 and A2 are the same but measured with the two different WGs and therefor labeled differently. On sample

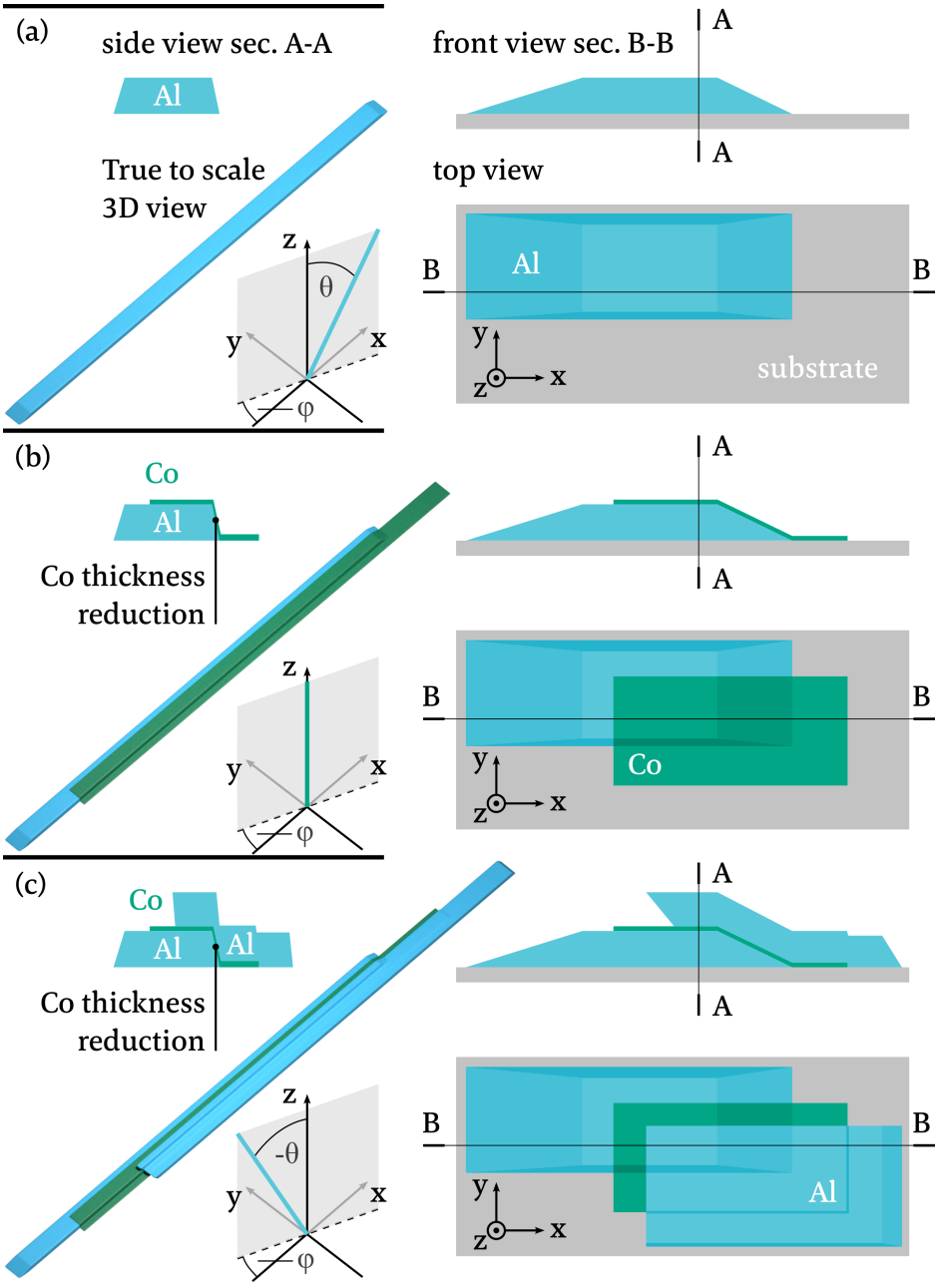

Figure 6: Schematic of the three steps (a), (b) and (c) of the shadow evaporation technique. See main text for further description.

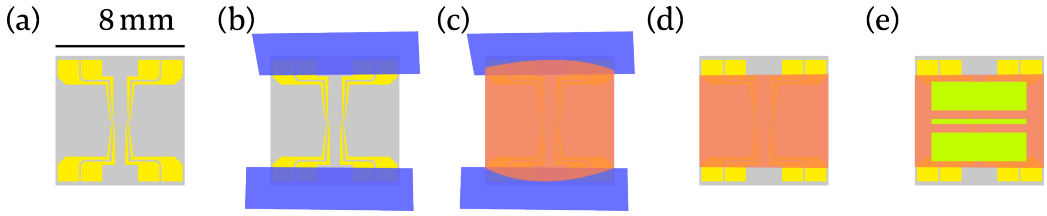

Figure 7: Integration of a WG (green) on top of the sample. (a) Au leads (yellow) on the substrate (gray). Two samples are placed in the center of the substrate. (b) Coverage of the Au contact pads with sticky tape (blue). (c) Spin coating of polyimide (orange) on the substrate. (d) Removing the sticky tape and bake out of the polyimide. (e) Patterning the Au WG by means of photolithography.

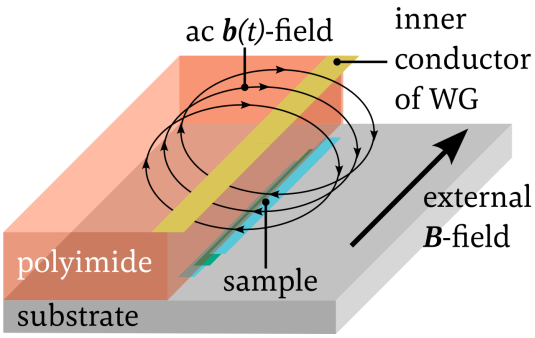

Figure 8: Schematic of the sample underneath the inner conductor of the WG (not to scale). The WG has a distance to the sample of around 1 µm due to the polyimide. An ac current in the inner conductor creates circular $\boldsymbol{b}(t)$-field lines which are perpendicular to the external $\boldsymbol{B}$-field.

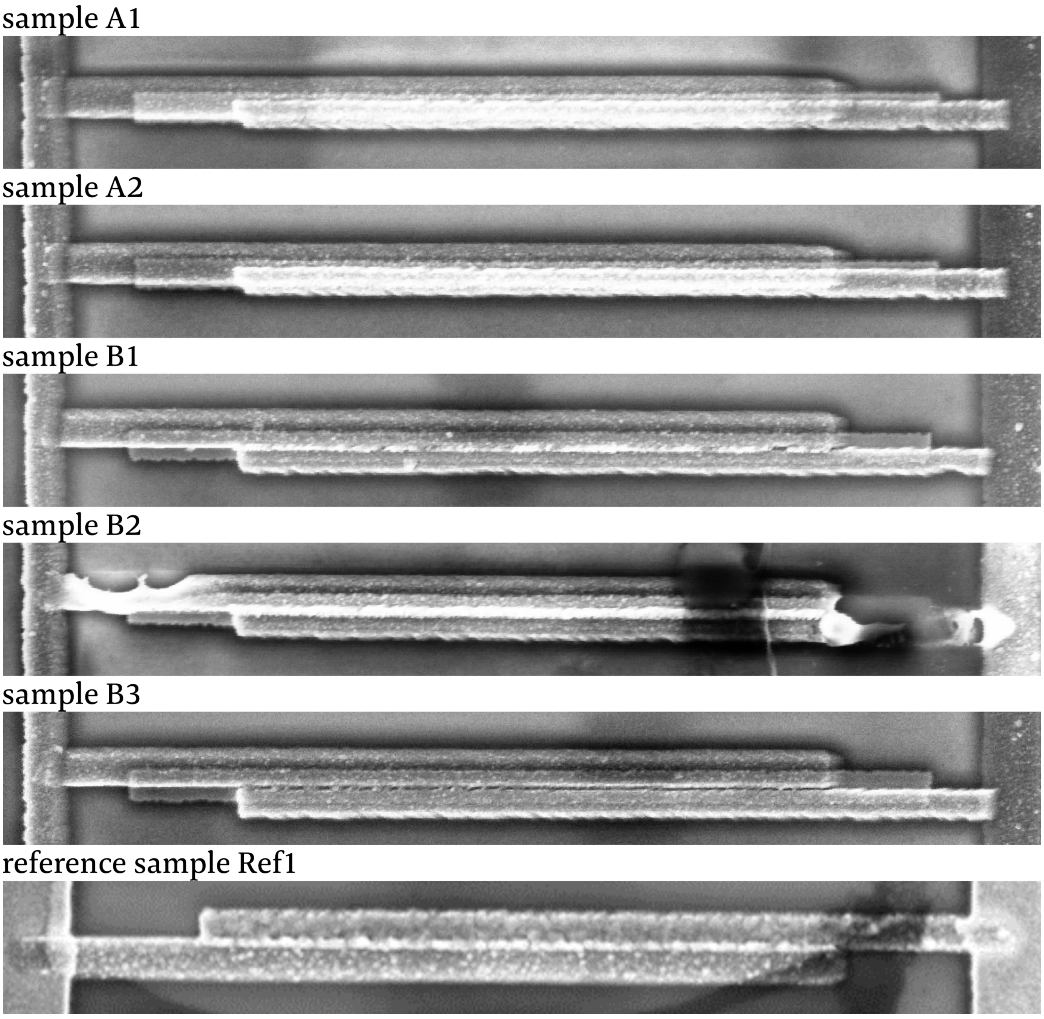

Figure 9: SEM images from top to bottom of sample A1, A2, B1, B2, B3 and Ref1. The image of sample B2 was taken after measurement during which the sample suffered a static discharge, as can be seen at the left and right molten ends. The dark black bar laying on the right part of sample B2 and Ref1 is most likely residual resist.

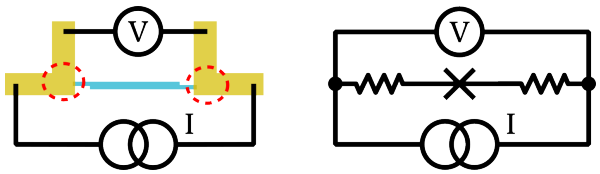

Figure 10: Schematic of the probing of reference sample Ref1 (blue bars). 5 µm wide Au leads are connected to either side of the sample. The intersection of two leads on one sample side leads to an Au island of $5 \times 5\,\mu m^2$ (red dashed circle). These islands act as series resistors to the S-S junction between the four probes.

Table 2: Basic information about the samples under investigation. The column "Co gap" distinguishes between an assumed effective Co thickness between the Al layers of 1 nm to 2 nm (small) and > 10 nm (big). In the column "AC", "ext. WG" stands for a WG patterned on a Kapton™ foil laying on the samples and "int. WG" for a micro fabricated on chip WG. T_c, B_c and I_c result from measurements.

sample	Co gap	AC	T_c (K)	B_c (mT)	I_c (µA)	R_N (Ω)
A1	small	int. WG	1.5	318(3)	4.3	60
A2		ext. WG		297(3)	5.7	45
B1	small	ext. WG	1.6	–	4.5	97
B2	small	ext. WG	1.6	325(25)	4.5	73
B3	big	ext. WG	1.55	318(6)	5.4	150
Ref1	-	-	1.45	320(20)	0.05(1)	6000

A1 an integrated WG was fabricated. A2, B1, B2 and B3 were measured with the Kapton™ foil WG placed on the substrate. The reference sample Ref1 is made out of two Al bars separated by AlOx. The nominal geometry for Ref1 is the same as for the actual samples. After the evaporation of the first Al bar, the sample was set under oxygen pressure of 3.5 mbar for 4 minutes and finally the second Al layer was evaporated. The sample is connected to four Au leads of width 5 µm. As a result, a part of the Au leads act as a series resistances to the S-S junction which are also probed by the four Au leads. This is illustrated in figure 10. Theoretically the Au series resistors contribute maximum 1 Ω which lies within the uncertainty.

3.2 Setup

Measuring our S-F-heterostructures requires low temperatures T, high frequency noise reduced dc measurement lines, a magnet and microwave (MW) cabling. The following sections give a brief overview of the different components needed. The standard cryogenics and wiring we use is described in detail by Jack W. Ekin [73].

3.2.1 Cryogenics

To measure our S-F-heterostructures at temperatures well below the critical temperature T_c of Al, we use an Oxford Instruments Heliox™VL cryostat [74]. With the installed measurement cabling but without any current or MWs applied, the cryostat reaches a base temperature of around 360 mK. The base temperature can vary by a few mK, depending on the liquid ^{4}He level of the dewar in which the cryostat is placed. The dewar is equipped with a superconducting magnet. A Heliox™VL cryostat is a sorption pumped ^{3}He insert. The cooling cycle, which is illustrated in figure 11, starts with out-gassing the adsorbed ^{3}He from the sorption pump (sorb) by heating the sorb to 30 K. In parallel ^{4}He from the surrounding bath gets pumped through a needle valve causing the 1 K plate to cool down to around 1.8 K. At this temperature all the gaseous ^{3}He condenses within 30 minutes and drops down into the ^{3}He pot. After this condensing phase the sorb is left to cool and starts adsorbing ^{3}He which evaporates from the ^{3}He pot. This evaporation causes the ^{3}He pot to cool down to the base temperature and cools the sample holder which is thermally anchored to the ^{3}He pot.

3.2.2 Electronics

Measuring a voltage drop at the samples down to several µV under MW irradiation requires special dc and ac electronics, which is shown in figure 12. The dc electronics, illustrated in figure 12(a), consists of a Yokogawa 7651 dc source [75], BNC cables outside of the cryostat and twisted pair manganin™ cables inside. The data acquisition system (DAQ) consists of the analog to digital converter ADwin-Gold from the company Jäger and a computer. With our configuration of the ADwin software, it is capable of taking 20 k data points per second. Normally, 1000 data points are averaged before they are transferred to the computer. The number of data points over which is averaged can vary and depends on the desired measurement resolution. A LabView™ software by the company

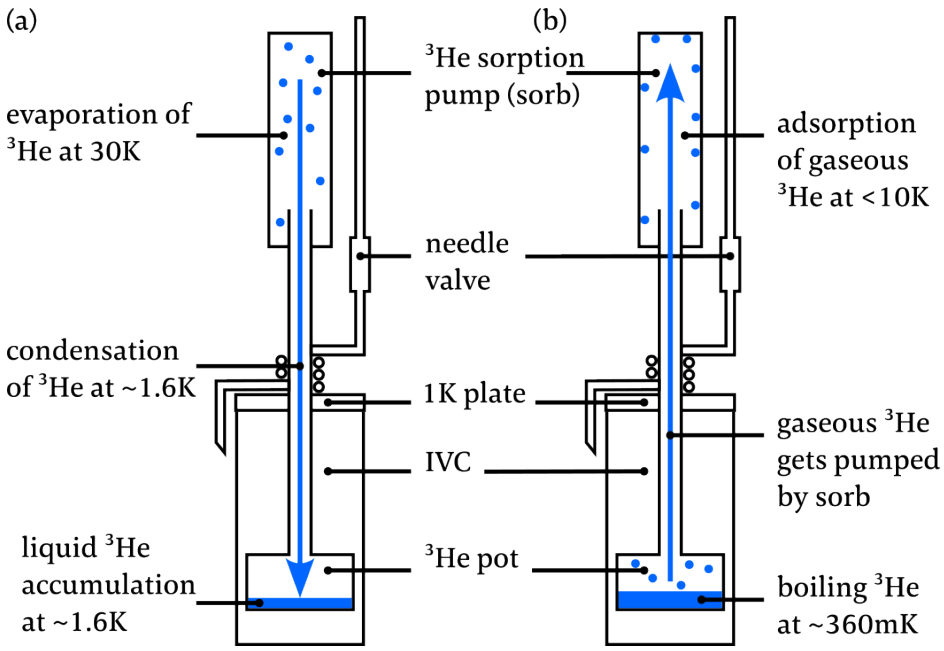

Figure 11: Schematics of the Oxford Instruments Heliox™VL ^{3}He cryostat and its functionality. (a) Condensation: Sorption pump (sorb) heated to 30 K releases gaseous ^{3}He which condensates at the 1 K plate. Cooling of the 1 K plate well below the condensation $T = 3.19\,\mathrm{K}$ of ^{3}He by pumping ^{4}He through the needle valve. (b) Cooling: After turning off the sorb heater the cooled sorb adsorbs ^{3}He which evaporates in the ^{3}He pot. The evaporation cools the ^{3}He pot to the base temperature $T_{\mathrm{base}} \approx 360\,\mathrm{mK}$.

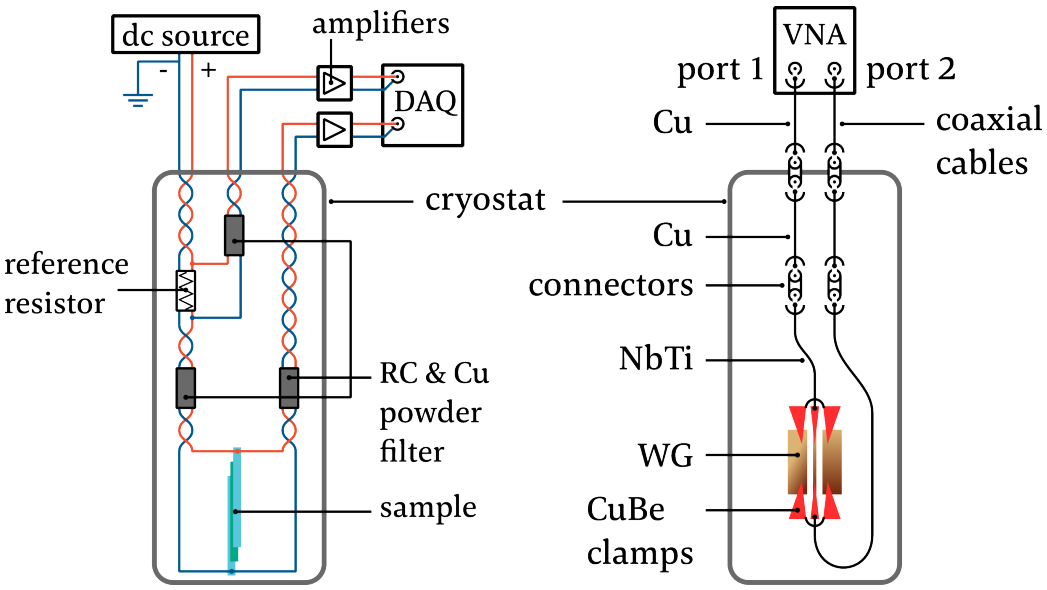

Figure 12: (a) dc electronics of the setup. The sample is dc-current sourced and four-point probed. The voltage drop at the sample and at the reference resistor is amplified and processed by the DAQ (data acquisition system composed of analog to digital converter, computer). The RC and Cu powder filters and the reference resistor are thermalized at the ^{3}He pot base temperature. (b) ac electronics. MWs are transmitted by coaxial cables from a vector network analyzer (VNA) to the WG. From the VNA to the cryostat, Huber & Suhner Sucoflex™ Ag plated Cu coaxial cables are used. Inside the cryostat Cu coaxial cables run down to thermally anchored connectors at the ^{3}He pot. From there to the CuBe clamps superconducting NbTi coaxial cables are mounted.

National Instruments controls the devices. The output terminal of the Yokogawa 7651 dc source consists of five ports. The upper two (tagged with "Hi") and the lower two (tagged with "Lo") are short-circuited, respectively. Additionally the chassis of the output panel (tagged with "G" is connected to ground and short circuited to the two Lo ports. This is the normal operation mode advised by the manufacturer to reduce noise when an output port is grounded (see manual [75]). BNC coaxial cables connect the dc source outputs and the input ports of the ADwin-Gold with a breakout box which is connected to a 24 pin Fischer connector to the cryostat. The dc measurement lines need to be thermally coupled to the cryostat at the ^{4}He bath temperature of 4 K and at the ^{3}He pot base temperature to reduce the heat load to the sample. This is achieved by winding the wires around the metal parts of the cryostat. Because of the relatively low cooling power of the ^{4}He pumped 1 K plate, the wires must not be wound around it. When the dc wires pass the 1 K plate, a loose touch cannot be avoided, but does not interfere the cooling significantly. The dc wires are made out of manganin™ which has a four orders of magnitude lower thermal conductivity than Co [73]. Twisting each dc line pair together (see figure 12(a)) reduces pick-up noise [73]. In the dc bias-current line there is a 240 Ω reference resister to measure the actual current through the lines. The voltage drops at the reference resistor and is amplified by a voltage amplifier of the series DLPVA-100-F from the company Femto, before the signal is passed to the DAQ.

The ac electronics, illustrated in figure 12(b), consists of the vector network analyzer (VNA) ZNB 40 from the company Rohde & Schwarz and several MW coaxial cables of different material. The VNA is run in the constant-wave mode (CW mode). This means the VNA sources a constant frequency at port 1 or 2, if the measurement channel of the VNA is set to measure either S_{21} or S_12 respectively. The bandwidth (BW) of the source can be set from 1 Hz to 10 MHz with an output power from -30 dBm to 0 dBm. From the VNA to the cryostat, Ag plated Cu coaxial cables of the model Sucoflex™ 102A are used. Within the cryostat Cu coaxial cables are mounted between room temperature down to the ^{3}He pot where a thermally anchored connector links the Cu cable with a NbTi coaxial cable. The latter are mounted to coaxial connectors which are placed on the sample holder's printed circuit board (PCB). From there the MW are transmitted to the sample by means of the solder-connected CuBe clamps on the PCB which are connected to the WG. This can be seen in figure 4(h). The microwave cabling is nominally symmetrically constructed but the impact of the MW on the transport measurements differ for the two possible output

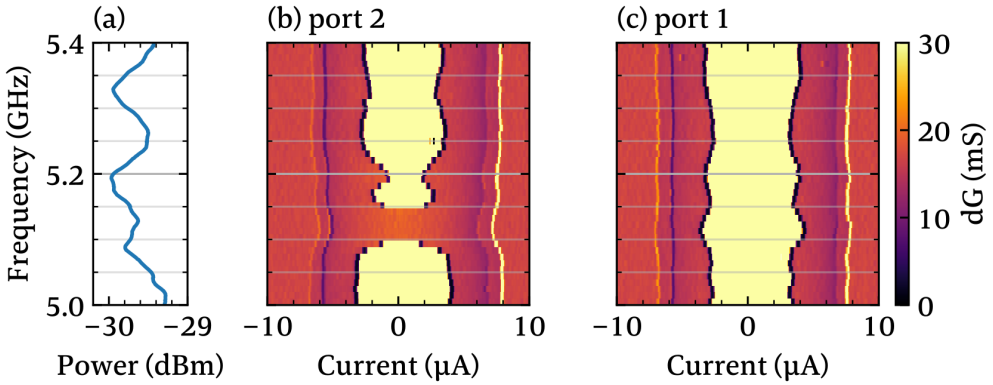

Figure 13: (a) Calculated power for frequencies between 5 GHz to 5.4 GHz in steps of 10 MHz at the WG assuming a symmetric MW cabling. (b) Differential conductance vs bias current vs frequency with microwave power output at port 2 of the VNA. (c) Data taken with same specifications as in (b) but with power output at port 1.

ports of the VNA. It even appears that for some frequencies the superconductivity is suppressed the most for port 2. This leads to the assumption that some frequencies are reflected or absorbed in the cabling on either side of the sample. An example of the difference in the transport measurements due to the different output ports is shown in figure 13. Figure 13(a) depicts the MW power at the WG. The power is calculated from the frequency response measurement through the whole cabling as described in section 2.3.

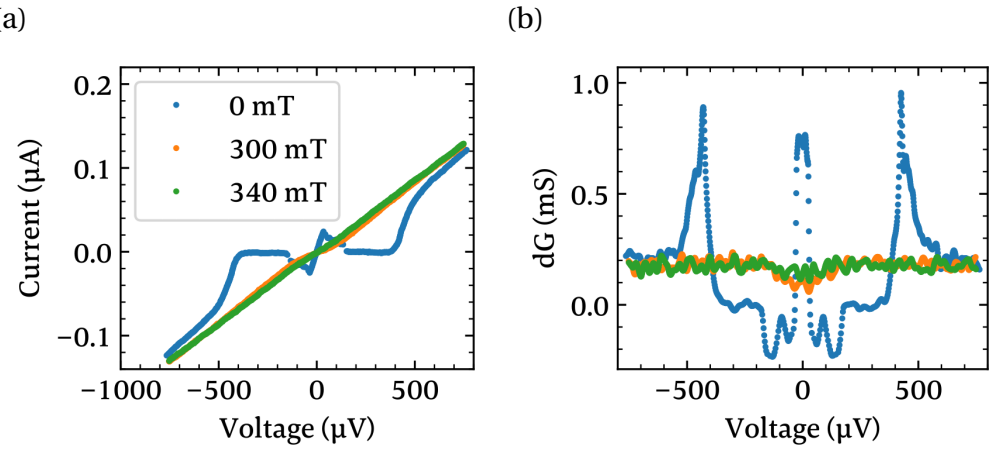

Figure 14: (a) *I*-*V*s of the reference sample Ref1 for a 0 mT *B*-field (blue), 300 mT (orange) and 340 mT (green) taken at 385(17) mK. (b) Differential conductance d*G* calculated from the values in (a).

4 Static Transport

4.1 Fundamental Sample Characterization

Since the samples under investigation in this thesis are quite complex, it is necessary to perform basic measurements on a simpler sample composition to analyze the sc properties of Al under the geometrical confinements. B_c and Δ can directly be determined by transport measurements on the reference sample Ref1. They are shown in figure 14 for temperatures below 400 mK and for different *B*-fields of step size 20 mT. The bias current was swept from negative values to positive values. This procedure is called up-sweep. A down-sweep hence is defined by the bias current being swept from positive to negative values. The *B*-field is aligned perpendicular to the long axis of the Al bar. The differential conductance curve in figure 14(b) at $B = 0$ mT (blue) shows a $\Delta = 212$ µeV for Al bars with a nominal shape of 5 µm·200 nm·50 nm. This is in good agreement with literature values on films [45] and bars of similar shape [76]. The actual shape of the two Al bars, however, is slightly different and lead to slightly different Δ. This fact may be the reason for the in-gap feature with a negative differential conductance (d*G*), what have been reported in literature for Al tunnel junctions with a relatively low resistance as well [76].

B_c is considered to be the lowest field at which the *I*-*V*s become linear. This

Table 3: Measured B_c for various samples. ξ_D is calculated from B_c by means of equation (26). D is calculated from the measured conductivity σ by means of equation 15.

	Ref1	A1	A2	B2	B3
B_c (mT)	320(20)	321(3)	297(3)	325(25)	318(6)
ξ_D (nm)	32(1)	32.0(1)	33.3(2)	32(1)	32.2(3)
λ (nm)	723(23)	724(3)	697(4)	728(28)	721(7)
D (cm^2s^{-1})	-	24(1)	24(1)	20(3)	10(1)

is the case for 340(20) mT and can be seen in figure 14 at the green curve. ξ_D and λ can be calculated from B_c. To do so it is necessary to know if the samples are of tpye I or II. As an estimation, ξ_D can be calculated from the equation (9) where the diffusion constant D can be calculated from the conductivity σ with the help of the modified Einstein relation from equation (15). The conductance is calculated from the measured R_N of the S-F-heterostructures in Table 2 and gives a range of $\sigma = 5(3) \cdot 10^6\,\Omega^{-1}m^{-1}$. This value is in the middle of a wide distribution of literature values, collected in [77], ranging from $1 \cdot 10^8\,\Omega^{-1}m^{-1}$ to $1 \cdot 10^5\,\Omega^{-1}m^{-1}$ what suggest that the Al-Co interface of our samples is highly transparent. With our calculated σ and the values for $E_F = 11.63\,eV$ and $n = 18.06 \cdot 10^{22}\,cm^{-3}$ for Al taken from [54], the diffusion constant is $D = 17(7)\,cm^2s^{-1}$. This value is reduced by a factor of 4 compared to pure Al with $D = 66\,cm^2s^{-1}$ [78] but it is in good agreement with literature values on S-F-heterosturcures made out of thin Al and EuS [79]. With our calculated D and measured Δ, equation (9) provides a range for $\xi_D = 75(25)\,nm$ which is 15 to 30 times smaller than ξ_0 for bulk Al. Furthermore, $\lambda = 350(116)\,nm$ can be calculated from $\xi_D = 75(25)\,nm$ and the theoretical values for ξ_0 and λ_L in (8) and (18) respectively, using equation (22). Even though this estimation leads to a wide range of ξ_D and λ values, the conditions in equation (24) for a S of type II is fulfilled.

A more accurate calculation of ξ_D can now be made by the B_{c2} equation (26). Table 3 shows the calculated ξ_D from the individual B_cs of various samples and lead to a mean $\xi_D = 32.3(14)\,nm$. λ can again be calculated from equation (22) leading to a mean value of $\lambda = 719(32)\,nm$. The individual values are shown in table 3. The deviations may be due to slight variations in the geometry or the vapor deposition parameters for the individual samples.

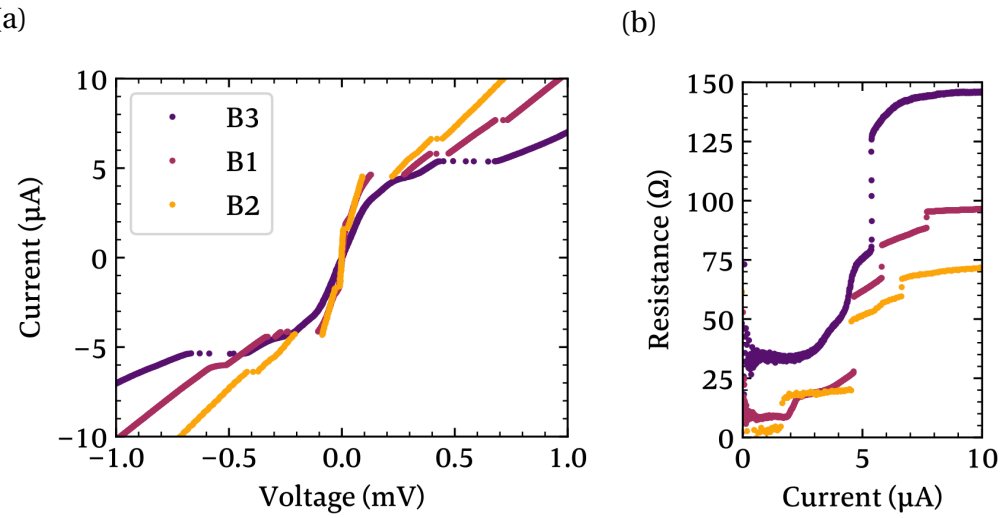

Figure 15: *I-V* up-sweeps of the samples B1, B2 and B3 taken at 348(2) mK, 349.4(1) mK and 297(1) mK respectively in (a). Resistance calculated from the *I-V* data

4.2 Transport Characteristics

Samples B1, B2 and B3

Heaving a set of samples helps to assign the different transport features to the different parts in the samples, which are depicted in figure 17(a) and further described in section 4.3. Although they are made by the same nominal procedure the samples are visually distinguishable. SEM images of the samples B1, B2 and B3 are depicted in figure 9 in the samples section. These different geometries lead to different *I-V*-characteristics shown in figure 15. The sample B1 and B2 show the highest number of steps in their *I-V*s. There are five steps in the down-sweep of sample B1. This is shown more clearly in figure 16(a). Figure 16(b) depicts the corresponding *R-I*-curve which is calculated from the *I-V* data . The most striking difference is the vanishing residual resistance R_{res}^{B2} and low $R_{res}^{B1} = 0.09 \cdot R_N$ of sample B2 and B1 respectively, whereas sample B3 has a higher residual resistance of $0.22 \cdot R_N^{B3}$ with an overall higher $R_N^{B3} = 150\,\Omega$ compared to $R_N^{B2} = 73\,\Omega$ and $R_N^{B1} = 97\,\Omega$. The R_{res} and R_N clearly match with the geometries of the respective samples. Sample B3 has a visible Co gap due to the large lateral shift of the two Al layers compared to the samples B1 and

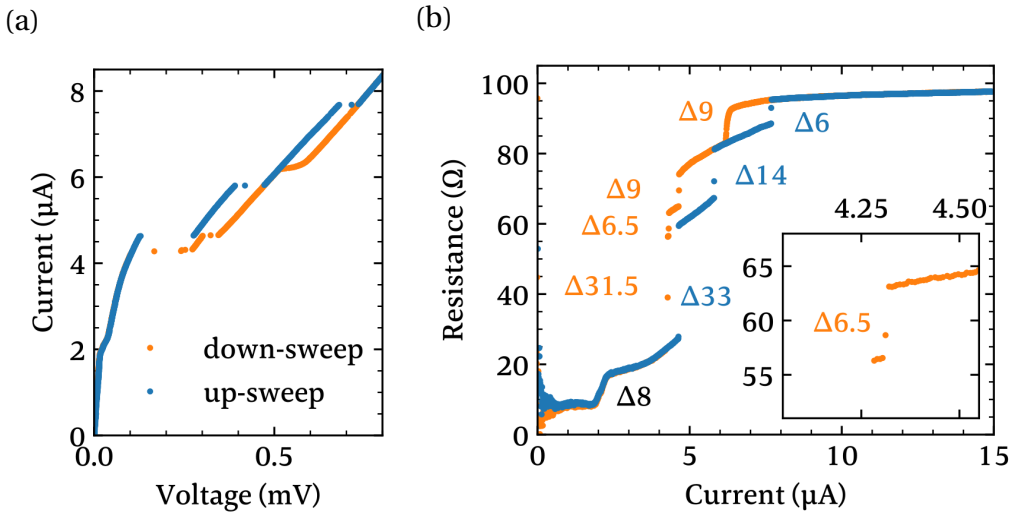

Figure 16: I-V-characteristics of sample B1 in (a) taken at 348(2) mK. Corresponding resistance over current in (b) calculated from the I-V data. Blue data points indicating a bias current sweeping from negative to positive values (up-sweep) and orange data points a current sweeping from positive to negative values (down-sweep). The Δ-values are indicating the change in the resistance for each step in Ω. Note that there is a tiny I-V-branch around 60 Ω leading to an additional step in the down-sweep curve (see inset).

Table 4: Resistance ratios R_{geom} calculated from the samples geometry. The R_{geom} values were applied to the total sample resistances R_N from table 2 what leads to the semi theo. R values of the separated sample parts.

parts	S	S/F	S/FS	S/F	S
relative R_{geom} [%]	8.6	15.1	47.4	18.1	10.8
semi theo. R^{B1} [Ω]	8.3	14.6	46	17.6	10.5
semi theo. R^{B2} [Ω]	6.3	11	34.6	13.2	7.9
semi theo. R^{A1} [Ω]	5.1	9	28.3	10.8	6.4

B2 where the Al layers lie on top of each other when viewed from the vertical perspective (see fig. 9). Therefore, a sandwiching of the Co layer by the two Al layers is ensured in sample B1 and B2 but not in B3. This, on the other hand, means that at least sample B2 must host a ferromagnetic Josephson junction (fJJ) because of a vanishing R_{res}. This is the proof that current can flow through the Co layer without dissipation. Due to the geometrical considerations on the Co thickness in figure 6 (sec. 3.1), R_{res}^{B1} of sample B1 comes from a suppressed SC in the S/F parts and R_{res}^{B3} of ample B3 manly from the large Co spacing between the two Al layers.

To correlate the *I-V* features with the sample geometry in the next section, one can calculate the resistance ratios of the different sample parts relative to R_N of the whole sample. Sample B1 shall serve as a template to extract a simplified geometry of the parts defined by the colored dashed boxes in figure 17(b). The dashed boxes define the length of the different sample parts, labeled with Li. The rectangles of respective colors in figure 17(c) sketch the cross section of the individual sample parts which are used to calculate the resistance R_{geom} of a sample.

$$R_{geom} = \left(\underbrace{\frac{\mathrm{L1}}{\mathrm{A1}}}_{\mathrm{S}} + \underbrace{\frac{\mathrm{L2}}{\mathrm{A2}}}_{\mathrm{S/F}} + \underbrace{\frac{\mathrm{L3}}{\mathrm{A3+A4+A5}}}_{\mathrm{S/FS}} + \underbrace{\frac{\mathrm{L6}}{\mathrm{A6}}}_{\mathrm{S/F}} + \underbrace{\frac{\mathrm{L7}}{\mathrm{A7}}}_{\mathrm{S}} \right) \cdot \rho \tag{52}$$

For simplicity the sample was assumed just to be made out of Al. It means the Co layer and a potential interface resistance between Al and Co is neglected. The resistivity for pure Al hence cannot be calculated out of the transport measurements. Therefore the value $\rho = 6.2 \cdot 10^{-8}\,\Omega\mathrm{m}$ for 50 nm flat Al at 8 K was taken from [80] to calculate the theoretical resistance R_{geom} out of the geome-

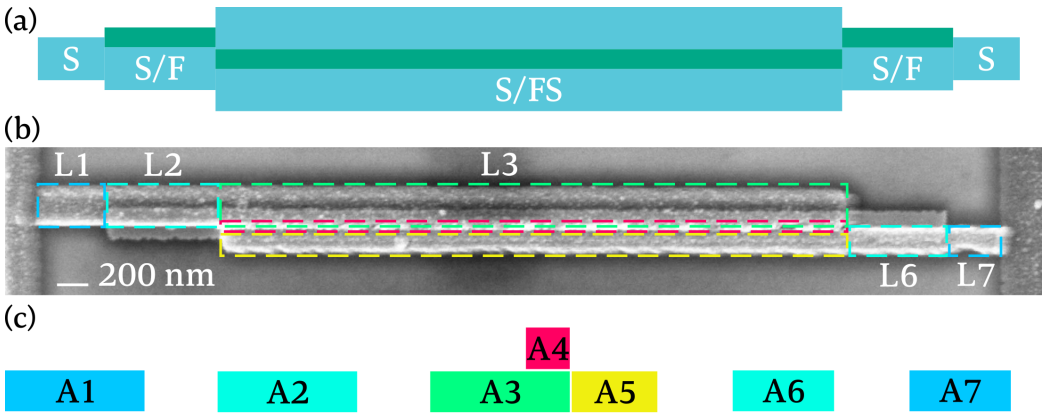

Figure 17: (a) Cartoon of the different sample parts. S consists of bare Al (blue). S/F is a piece of Al strongly magnetically proximitzed by Co (green). S/FS is weakly magnetically proximitzed by Co, whose magnetization is itself weakened by two layers of Al. (b) SEM image of sample B1 with colored dashed frames around the individual sample parts and their lengths Li. (c) Colored rectangles depict the simplified cross sections Ai of the respective parts. The products of R=Li/Ai $\cdot \rho$ are used to calculate a theoretical value for the sample resistance (see main text for further description).

try. Dividing equation (52) by R_{geom} gives the relative resistance ratios of the different sample parts which are under-braced and tagged in equation (52). These values are depicted in table 4 as "relative R_{geom} [%]". Applying these ratios to R_N^{B1} of sample B1 leads to the resistance values "semi theo. R^{B1} [Ω]" in table 4. This acts as an example for all samples since the geometries are nominally the same. If the whole S/FS part, defined by equation 52 and figure 17(a), turns normal conducting, it contributes the highest ratio to R_N because this is the longest part in the samples. This leads to the assumption that the biggest steps in the *I*-*V*s are related to the fJJ which is formed in the S/FS part. The current at which these steps appear thus is considered to be the I_c of the fJJ, except for sample B3 which does not have the weakly proximitized S/FS part. It consists only of bare S and S/F parts. Table 4 shows that the strongly proximitized S/F parts contribute relatively small resistance ratios. The fact of a strong suppression of the SC in the S/F part plus the small resistance contribution of the same leads to the assumption that the first step at lowest bias currents in the *I*-*V*s and *R*-*I*-curves has its origin in a Josephson junction (JJ) formed by the S/F part. This would mean that only the S/F part in sample B2 becomes SC, while it stays normal conductive (N) in B1 and B3.

If a JJ coupling between two parts vanishes, at least one part must have turned N, what is visible as a voltage jump in the *I*-*V* or as a resistance jump in the corresponding *R*-*T* curves. Since the parts are not sharply distinguishable, sub-parts of the parts may become normal conductive before the JJ collapses. The sub-parts can be defined by weak spots in the geometry, like deformations, constrictions or groves and lead to a gradual transition from a S to a N state in a narrow S wire, as described by Kadin, Skocpol and Tinkham [81].

This is illustrated in the equivalent circuit diagrams 20 in the next section as a constant growth of the resistive parts (⩘⩘) for an increasing bias current. The calculated resistances in table 4 can thus just be upper limits of a step in the actual measured resistance. The gradual change in the resistance hence is most likely due to a gradual change of the sub-parts from S to N as mentioned in section 4.3.

Summarizing the previous considerations, the steps in the *I*-*V*s and corresponding *R*-*V* curves, which appear at the lowest bias currents seem to originate from a S/F part. The biggest steps in the transport characteristics of sample B1 and B2 are assigned to the fJJ in the S/FS part. The steps appearing at the highest bias currents are assigned to the bare S parts.

All interfaces between adjacent parts in the samples seem to be able to form a JJ but do not necessarily have to, what can be seen in the *I*-*V*s of sample B3,

A1 and A2. They host a lower amount of I-V steps than one could expect from the considerations of the following section 4.3.

Samples A1 and A2

Figure 18(a) shows a typical I-V-characteristic of the sample A1 without a B-field or microwaves (MW) applied. The blue curve shows an bias current up-sweep from negative to positive values and the orange one a down-sweep measurement. The resistance over the positive bias current in Figure 18(c) is calculated from the I-V data in figure 18(a). According to the analysis the previous sections, the hysteretic part of the I-V in figure 18(a) at $\pm 4\,\mu A$ is considered to be the critical current of the fJJ.

There are positive (from low to high values) and negative voltage jumps (from high to low values) around $\pm 360\,\mu V$ to $\pm 480\,\mu V$. The close-up of that I-V-characteristic is depicted in figure 18(b). The calculated $R(I)$ in figure 18(d) shows clearly that these voltage jumps lead to an increase of R beyond $R_N = 59.6\,\Omega$. An increase of R can be explained by a spin alignment process at a ferromagnet (F) superconductor (S) interface [82]. The spin polarized current in F needs to be aligned to the spin-less current in S. At the onset of the SC, an additional contact resistance can overcompensate the reduction of R in S. Thus the jump at $I = 7.7\,\mu A$ marks the onset of SC in our S-F-heterostructre.

The samples A1 and A2 are the same. After the measurement on A2 a WG was integrated on chip and the sample was then labeled A1. All the differences in the I-V-characteristics may be due to a mechanical stress on the sample during the integration of the WG and the exposure to ambient environment for over one month. Figure 19 shows the deviations of the I-Vs between sample A1 and A2. The most striking difference is the over all increase of the resistance. R_N raised by $15\,\Omega$ from $45\,\Omega$ to $60\,\Omega$ while the R_{res} in the low bias current branch increased by around $5\,\Omega$. This can be explained by an partial oxidation of the sample. Considering the sample's cross section with an increased thickness of an oxidized outer shell, the effective metallic and hence superconducting cross section reduces. This leads to an increase in R. Following the theory of a JJs I_c of Ambegaokar and Baratoff from equation (29) it is a necessity for I_c to reduce when R_N increases. The critical currents of our samples containing a JJ are in reasonable agreement with the theoretical value as is compared in table 5. The prediction for the tunnel junction in Ref1 is more accurate than for the fJJs, as one would expect since equation (29) is just an approximation for weak links at low T.

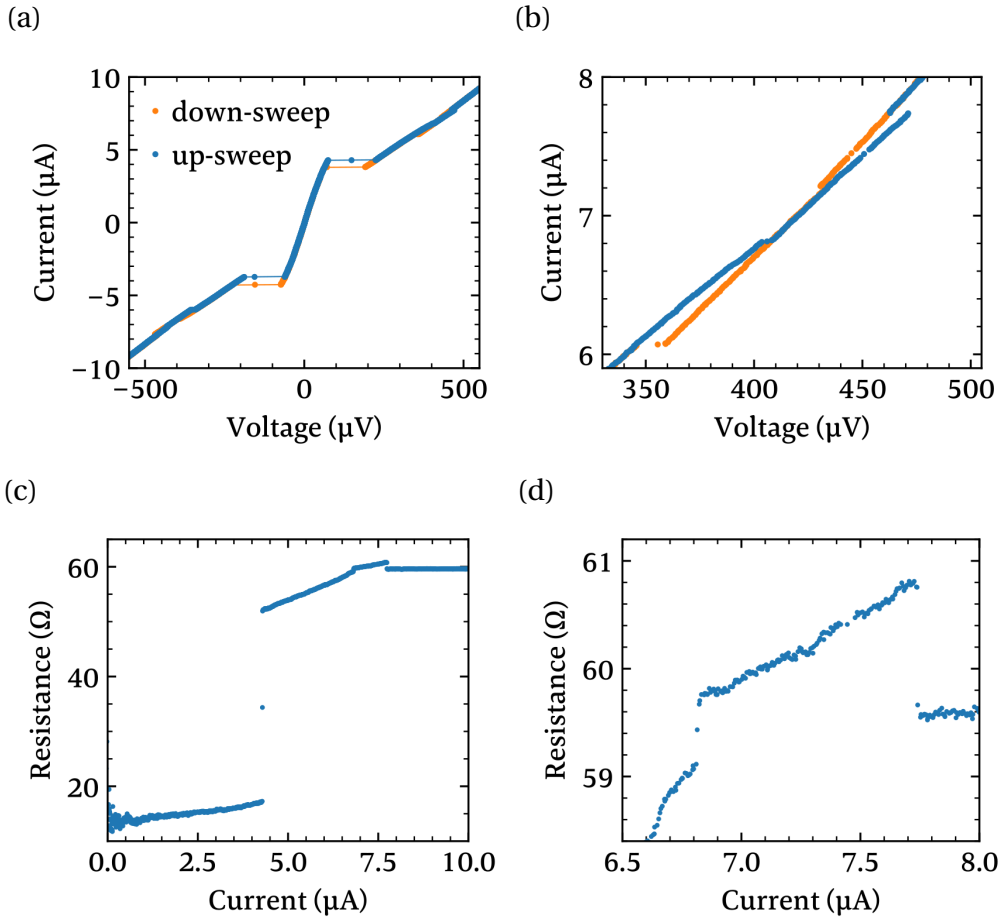

Figure 18: Transport characteristics of sample A1 taken at 370(2) mK. (a) *I*-*V* curves with bias current up-sweep (blue) and down-sweep (orange). Thin solid line serves as a guide for the eye. (b) Close-up of the positive high voltage part of the *I*-*V*s. (c) Resistance vs bias current calculated from the up-sweep *I*-*V* data for the positive voltage branch. (d) Close-up of the resistance vs bias current corresponding to the region of figure (b).

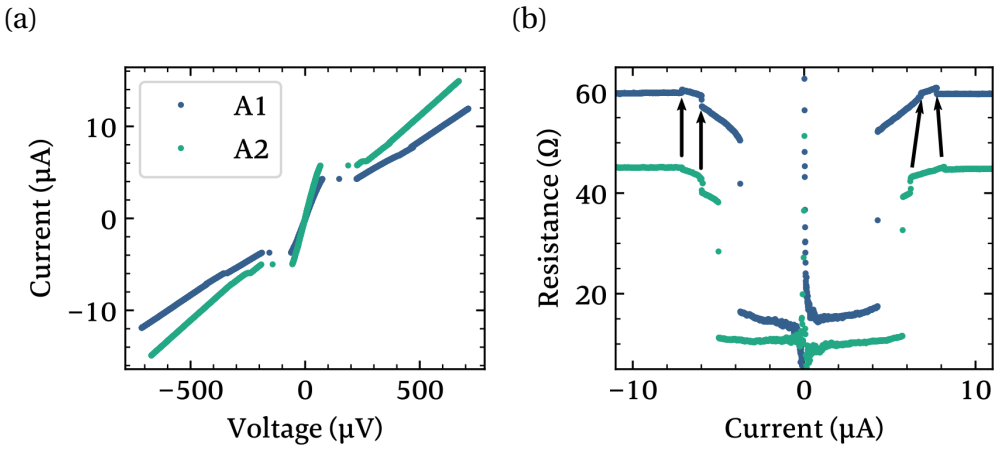

Figure 19: A1 and A2 are the same sample. After the measurement on A2 a WG was integrated on chip which was then labeled A1. a) shows the *I-V*-characteristics of the samples A1 and A2 at 370(2) mK and 345(1) mK respectively. I_c has been reduced from 5.7 μA to 4.3 μA. The resistance in b) is calculated out of the data in a). R_N increased by 15 Ω while the R_{res} in the low bias current branch increased by around 5 Ω. The small resistance steps appear at the same bias current when sweeping from high to low values indicated by the two left arrows. The left most step was going up in sample A2 and changed to a step down in A1. Sweeping from low to high currents the steps are shifted by 0.6 μA and -0.5 μA indicated by the two right arrows. The resistance peaks and dips around 0 μA are numerical artifacts.

Table 5: Experimental and calculated (theory) critical currents I_c of the samples with a JJ.

I_c (μA)	A1	A2	B1	B2	Ref1
experiment	4.3	5.7	4.6	4.5	0.05(1)
theory	4.7	6.2	3.4	4.6	0.056

4.3 Correlating Transport Features to Sample Geometry

The relatively simple procedure of shadow evaporation leads to a quite complex sample structure. The different distinguishable parts of the samples are labeled in figure 20(b) together with the current path x_I through the sample, depicted as dark blue arrows. There are bare superconducting parts S, parts which are proximitized by the ferromagnet S/F, superconducting parts stacked with an FS layer, denoted as S/FS and parts where F is sandwiched by two layers of S, forming a ferromagnetic Josephson junction (fJJ). The latter is the region where the current has to cross the F barrier. Figure 20(d) is a sketch of the cross section of the S/FS part with the current path x_I crossing F. The black B_{stray}-field lines shall illustrate the weakening of S due to the inverse proximity effect which is outlined in figure 20(c) as a reduction of I_c. The vertical black dashed lines in figure 20(b) and (c) delimit the different parts of the samples.

Figure 20(c) shows a sketch of the supposed evolution of the I_c along the current path x_I. The bare S parts are expected to have the highest I_c because these parts are not disturbed by anything. All other parts have a reduced S because of the proximity effect and its inverse counterpart, as explained in section 2.5.1. The lowest I_c is in S/F and it even appears that that region almost never becomes superconducting in our experiments. This is reflected in a residual R in most of the samples at any conditions. Note that the cross section of the right S/FS and S/F parts is smaller than the corresponding one on the left side. This leads to smaller I_cs in the JJs of the right side of the samples. For example a bias current of I_3 exceeds the I_c of almost all JJs but the leftmost.

Almost all steps in the I-V curves of any sample show a hysteretic behavior, like shown in figure 16. This leads to the assumption that the interface regions at the black dashed lines act as JJs. The intersection of the blue I_c line with the black dashed lines defines the critical currents of the JJs in the present explanatory model. In the S-F-S part the current has to go through the F layer and thus forms a ferromagnetic Josephson junction (fJJ). The green dashed line indicates how the fJJ is represented in the different figures 20(a), (b), (c) and (d).

If one applies no or a small bias current I_0, the right hand S/F part stays mostly normal conductive. This is represented in the lowest equivalent circuit diagram in figure 20(a) as a resistor symbol ⩘. Superconducting parts of the sample are drawn as straight lines and JJs as ×. In 20(c) the resistive S/F appears as the blue I_c line laying underneath the straight gray I_0 line. This means the bias current has overcome the I_c of the respective sample part. If the bias

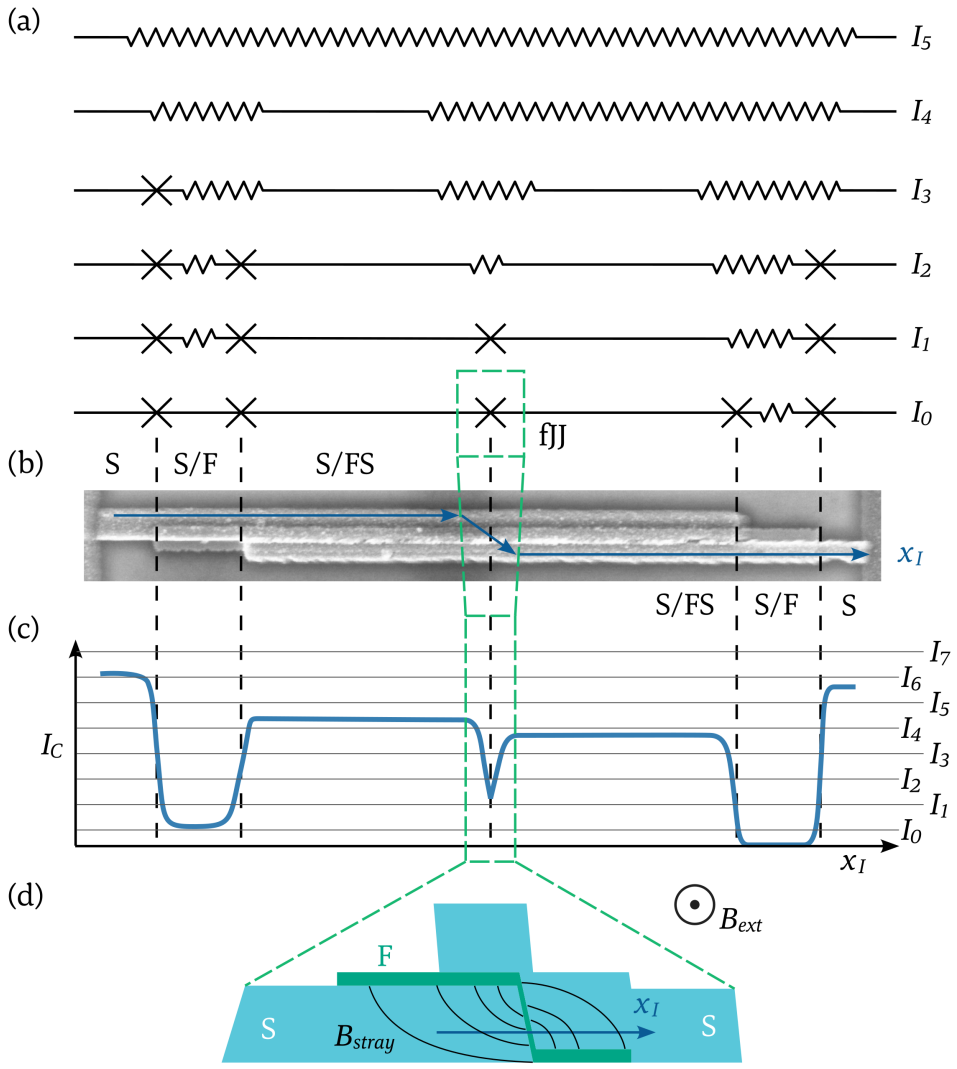

Figure 20: (a) Equivalent circuit of the samples for different bias currents I_i. ✕ denotes a JJ, —- is a S region and ⩘ denotes a resistive part. (b) SEM image of sample B1 with current path x_I (dark blue arrows). (c) Qualitative curve of I_c along the current path x_I through the sample. (d) Cross section through the S-F-S region with current path x_I and indicated magnetic stray field B_{stray} in S. Green dashed lines act as a guide to the eye where in the corresponding figures (a), (b) and (c) the S-F-S region is reflected. S/F stands for a S strongly weakened by an adjacent F. S/FS stands for an intermediate weakening of an adjacent FS layer.

current rises to I_1 the JJ collapses, which is formed by the right S/F and S parts. In the second lowest equivalent circuit diagram in figure 20(a) this is depicted as a resistor ⩘ at that position where the junction symbol ✕ was for the lower bias current I_0. By increasing the bias current further, more and more parts of the samples become normal conductive. This is represented as more parts of the blue I_c line lay under the respective bias current I_i and more resistive parts ⩘ add up in the equivalent circuit diagrams. The smooth transitions of the blue I_c line across the black dashed lines, meaning between one sample part to another, is expected to be the reason for a gradual increase of the resistance of the samples when the bias current is increased. Every time the I_c of a JJ is exceeded, a step appears in the *I-V*s.

Although this is a rather simple picture the amount of steps in the *I-V*s fit to the number of possible JJs which makes this phenomenological model quite powerful when it comes to correlate single *I-V* features to the different sample parts. The real current path, however, is unknown and may alter the *I-V*s markedly. If the S, the S/F and the S/FS parts are in the superconducting state, it is quite clear that the current will flow through the S regions of the different parts. The current path through F will be where F is thinnest, what defines the fJJ. Its exact position along the S/FS parts is unknown and probably widely spread due to parallel paths through F. The actual shape of the fJJ hence is unpredictable and may be accompanied by parallel current path or even host inductive components as literature shows [83]. They claim that most of the common JJs have some kind of parallel inductance paths when no effort is made to suppress it. The inductance leads to additional kinks and non-linearities in the *I-V* characteristics.

In the following section the transport measurements will be analyzed step by step to correlate the transport features to the sample geometry. All nonlinear transport features different from the normal state are expected to be correlated to a superconducting states of at least one sample part. This should help to find out what are the physical effects causing the transport features. The following subsections guide through the transport measurements taken without a magnetic field applied and without irradiation of microwaves. Subsequently the application of a magnetic field followed by microwave irradiation give deeper inside to the physical phenomena.

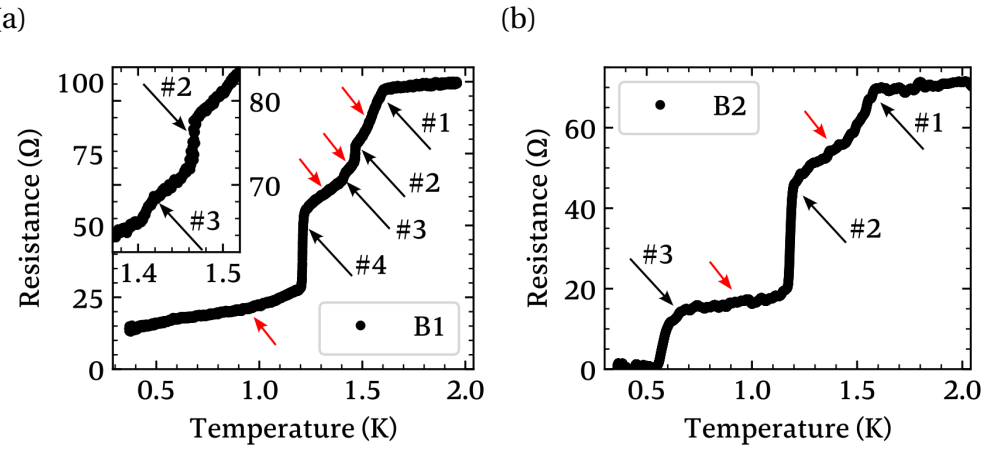

Figure 21: Resistance vs temperature of sample B1 measured with 2 µA bias current in (a) and of sample B2 measured with 1 µA. The numbered arrows (#i) indicate the different steps in the resistance and the red arrows indicate the regions where R changes gradually.

4.4 Temperature Dependence

Samples B1 and B2

One would expect so see the same amount of steps in the $R(T)$-measurements as in the I-V-curves. For sample B1 the R-T-measurement is depicted in figure 21(a). The equality of the amount of steps is not obvious at first glance. The first step (#1) at highest temperatures $T_c = 1.6\,\mathrm{K}$ is related to the step at highest bias current at $I = 7.7\,\mu\mathrm{A}$ and marks T_c of a bare S part of the sample B1. The $T_c = 1.6\,\mathrm{K}$ is around 400 mK higher than for clean bulk Al and in good agreement with previous measurements on Al nanostructures [51, 52]. Since R was measured with 2 µA bias current, the corresponding I-V-step at $I = 2\,\mu\mathrm{A}$ is not visible in the R-T-curve. Its R_{res}^{B1} at 365 mK is 17 Ω and is comparable to the onset of the resistance drop at 2 µA from the R-I measurement in figure 16(b). Two of the less prominent steps (#2 and #3) are separated by 55 mK visible in the inset of figure 21(a). They are probably corresponding to the Δ6.5 Ω and Δ9 Ω steps in the down-sweep curve in figure 16(b). The more pronounced step #2, which appears at $T = 1.465\,\mathrm{K}$, is rather fluctuating between two levels within 4 mK whereas the smaller step #3 appears at $T = 1.412\,\mathrm{K}$ with a gradual transition within 6 mK. According to the table 4, the biggest jump in R in the $R(T)$

plot in figure 21(a) as well as in the I-V-curve in figure 16(b) is caused by the S-N-transition of the S/FS part. The theoretical value of the jump in R is expected to be half of R_N. If one considers sub-parts of the S/SF part to undergo a S-N-transition gradually, still a major part seems to jump. For the up-sweep in figure 16 the biggest jump is 30% of R_N.

The regions in the $R(T)$ plot in figure 21(a) which undergo a gradual reduction of R are marked with red arrows. This gradual change in R is explained by a similar principle like the gradual resistance change in the transport measurements depicted in figure 20, if one exchanges I_c in the qualitative plotting in figure 20(c) by T_c. Along the sample the superconductivity in the different sub-parts is weakened by the Co gradually, indicated by the blue line in figure 20(c). By gradually increasing or decreasing the temperature, more and more sub-parts will become normal- or superconductive.

The whole R-T measurement was taken during a cool-down process and took 32 minutes. The cooling at around 1.4 K was the fastest with a speed of 57 mK/min. A time delay of 2 seconds is estimated between the actual temperature at the sample and the reading of the thermometer. The delay would cause the temperatures in the cool-down curves to be shifted by 3 mK to higher temperatures. In other words the steps in the R-T plots have happened at actually 3 mK lower temperatures than shown in the figures. This shift in the temperature occurs in all R-T plots presented because the cooling was quite the same during all the cool-down measurements.

Sample B2 exhibits three jumps in the transport measurements shown in figure 15. The corresponding cool-down-curve in figure 21(b) shows three distinct steps in R as well. This measurement was taken with 1 µA bias current leading to the appearance of the last step at 580 mK. The transition happens within 40 mK and is expected to be correlated to a S/F part. The biggest jump $\Delta R = 25\,\Omega$ happens at 1.18 K within a range of 30 mK and is attributed to the S/FS part of sample B2. The onset of the resistance drop is around $T_c = 1.58$ K.

Sample A1

Figure 22 shows the $R(T)$ of sample A1 from 4 K down to 420 mK. There are three prominent features in this graph. The first one is the enhancement of R_N before the R drops for lower temperatures, which is marked by the green arrow and shown more detailed in the inset of figure 22. The resistance in the normal-state at 4 K is 60 Ω and starts rising at 1.5 K before reaching its maximum of 61.7 Ω at 1.45 K. The onset of the rising resistance at 1.5 K is considered to be the T_c

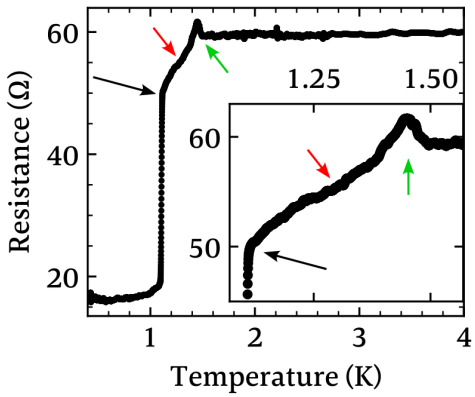

Figure 22: Resistance vs temperature measured on sample A1 with 2 µA bias current. The arrows mark a spin valve effect at the SC-N transition (green), a continuous reduction of R due to SC-N transitions of sub-parts of the sample at different T (red) and a sudden drop in R due to the formation of the fJJ (black).

of the bare S parts of sample A1. The magnitude of the resistance change is the same for the present (T) measurement and the transport measurement in figure 18(d) and hence is attributed to the same origin, i.e. a spin alignment process at an S-F interface during the transition of a N to a S state. The second feature is an almost sudden drop of the resistance within 10 mK at 1.1 K from 50 Ω to 19 Ω. It is marked with the black arrow in figure 22. This relatively huge drop is due to the S/FS region. Its counterpart in the transport measurement (fig. 18(a)) is the pronounced hysteretic voltage jump around ±4 µA. The third feature is the gradual decrease of $R(T)$ for decreasing T which is tagged with red arrows in figure 22.

4.5 Magnetic Field Dependence

For a thin superconducting Al layer below a thickness of 200 nm, the gap energy Δ reduces strictly monotonically with respect to an applied parallel B-field [45, 84] due to the orbital effect. And so does I_c because of its linear dependence to Δ which is shown in equation (16).

For sample A1 the dependence of I_c on B is depicted in figure 23. The lowest I-V curve in 23(a) is taken under the same conditions as the blue up-sweep I-V curve in figure 18(a), i.e., without any B-field or MW applied. The I-Vs

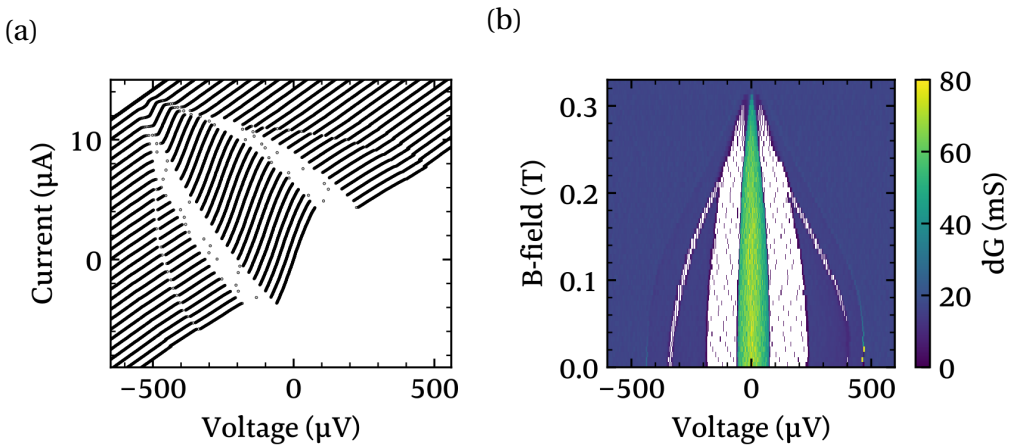

Figure 23: *I*-*V* measurements for *B*-fields from 0 mT to 330 mT at 379(11) mK in (a). The bias current was swept up from negative to positive values. Lower right curve taken at 0 mT, upper left curve taken at 330 mT. The curves are shifted by -20 µV and +500 nA for clarity. (b) Differential conductance d*G* vs bias current calculated from the *I*-*V*s in (a).

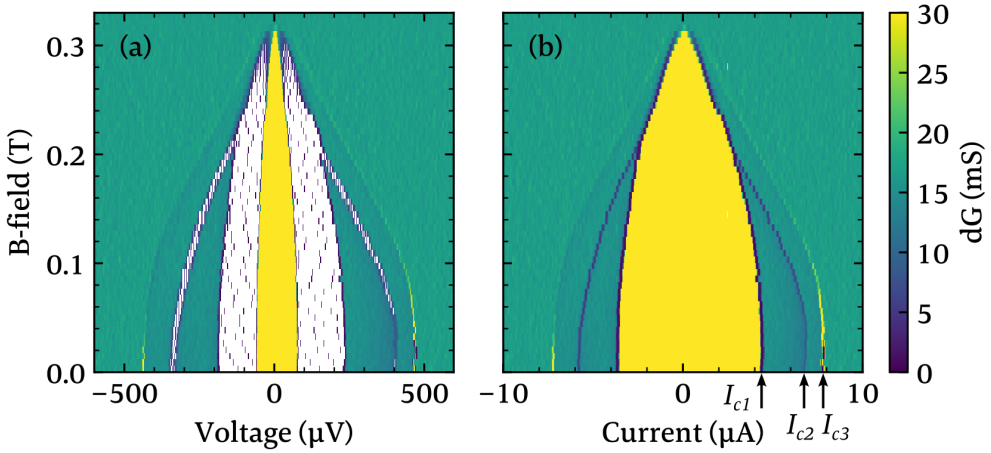

Figure 24: Differential conductance d*G* calculated out of the very same data as in figure 24. The data is plotted against a parallel in-plane *B*-field with a step size of 6 mT and the voltage in (a) and against the bias current in (b). d*G* is cut off at 30 mS to highlight the line-like features at $I_{bias} \approx \pm 7.5\,\mu A$. The black arrows mark the critical currents I_{c1}, I_{c2} and I_{c3} of the different sample parts.

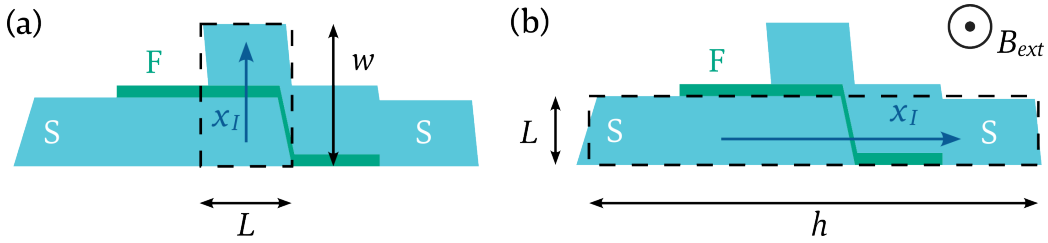

Figure 25: Sketch of the cross section of the sample A1. The length L and width w of the effective fJJ area (dashed frame) for an assumed vertical current path x_I in (a) and for an assumed horizontal current path x_I in (b).

developing to the upper left of the figure are shifted by -20 µV and +500 nA for clarity and are taken under a gradually increasing B-field in steps of 12 mT from 0 mT to 330 mT.

Figure 24(a) shows the same dG color plot as in figure 23(b) but with a cut off at dG = 30 mS to highlight the small line-like features at high voltages. Because of the voltage jumps this plot style looks rather scattered. For a clearer visualization of the development of the critical currents, dG is plotted against the bias current in figure 24(b). This is the preferred plot style throughout the thesis for dG data. The cut off of dG is used if we want to put the focus on the line-like features which we attribute to the critical currents of the sample parts. They are marked as I_{c1}, I_{c2} and I_{c3} in 24(b) (with the black arrows). This notation for the different I_cs of sample A1 and A2 is used throughout the following sections. If the high conductive region is worth a deeper discussion, the full color scale for dG is shown. For low B-fields the I_cs stay almost constant and start decreasing monotonously until they go to zero linearly, like expected for thin Al films [45] at the critical field B_c = 318(3) mT.

According to section 2.2.1, a JJ in a B-field is expected to give rise to a Fraunhofer pattern in $I_c(B)$. This is unique to the I_c of a JJ, a bare S does not show this behavior. However, the measurements in figure 24 do also not show any obvious minima of I_c for B-fields below B_c. To investigate the reason for this, one needs to estimate the effective area A of the JJ's interface. The geometry of our samples allows for two conceivable current paths through the F barrier as depicted in figure 25, each defining A differently, like depicted in figure 25 as the black dashed boxes. Since the dimensions of the cross section are smaller than $\lambda \approx 720$ nm, A is no longer defined by the F thickness and by λ but rather by the samples dimensions itself. The actual position in the sample where the current

passes the F barrier also defines A.

The current path x_J through the F barrier may be through the side face of the lower Al layer as depicted in figure 25(b). There the nominal Co thickness of 12 nm is reduced to 1 nm to 2 nm as was measured from the 3D model in figure 6 (sec. 3.1). Since in Co $\xi_D = 3$ nm [71], even a singlet supercurrent should be able to cross the F barrier and form a fJJ. This assumption of a vertical x_J through the samples cross section defines the length L of A as the thickness of the lower Al layer and the width w of A is equal to the horizontal dimension of the cross section, because this dimension is smaller than λ. The effective Josephson area for sample A1 then is $A \approx 50\,nm \cdot 270\,nm = 13.5 \cdot 10^{-15}\mathrm{m}^2$ which leads to the first minimum of the Fraunhofer pattern at $B_0 = \Phi_0 / F \approx 153$ mT. However, this does not consist with the findings in figure 24 where no Fraunhofer pattern in $I_c(B)$ could be observed. The effective Josephson area A might be smaller what would potentially leads to a first minimum of the Fraunhofer pattern which is higher than $B_c = 318(3)$ mT.

A simpler assumption of a vertical current path x_J along the stack direction of the S-F-S layers, like shown in figure 25(a), leads to a length $L \approx 93$ nm and is defined by the overlap of the S-F-S stack along the vertical projection and the width $w \approx 112$ nm is defined by the stack height. The resulting area $A \approx 10.4 \cdot 10^{-15}\,\mathrm{m}^2$ leads to a $B_0 = 199$ mT what is still lower than B_c.

It might be that the S-F-S interface does not form a fJJ at all. On the other hand, the previously made assumptions are quite rough. Theory shows a strong deformation of the Fraunhofer pattern in a fJJ with an inhomogeneus magnetization. Börcsök et al. [85] predict nonzero minima in the Fraunhofer pattern. In a S-F-I-S junction with an additional insulating layer I, Alidoust, Sewell and Linder [86] predict a shift of the first Fraunhofer minimum up to $B = 1.7 \cdot \Phi_0$ accompanied by a reduction of $I_c(B = 0)$ for a strong F in a long JJ. A more trivial reason for not seeing a Fraunhofer pattern could be a more complex current path x_J through the F barrier which leads to a smaller effective A.

The yellow high-conductive part in figure 26 can visually be separated in two parts. The one starting at 0 mT to 250 mT is hysteretic to the inversion of the bias current sweep direction. The hysteresis becomes clear by comparing the up-sweep measurement in figure 26(a) and the down-sweep measurement in figure 26(b). The respective other directions are sketched by the blue and orange dashed lines. However, the part from 250 mT to the critical magnetic field at 318 mT is not hysteretic. Furthermore, the extrapolation of the curvature of the hysteretic part by eye vanishes at approximately 300 mT instead of at the critical magnetic field.

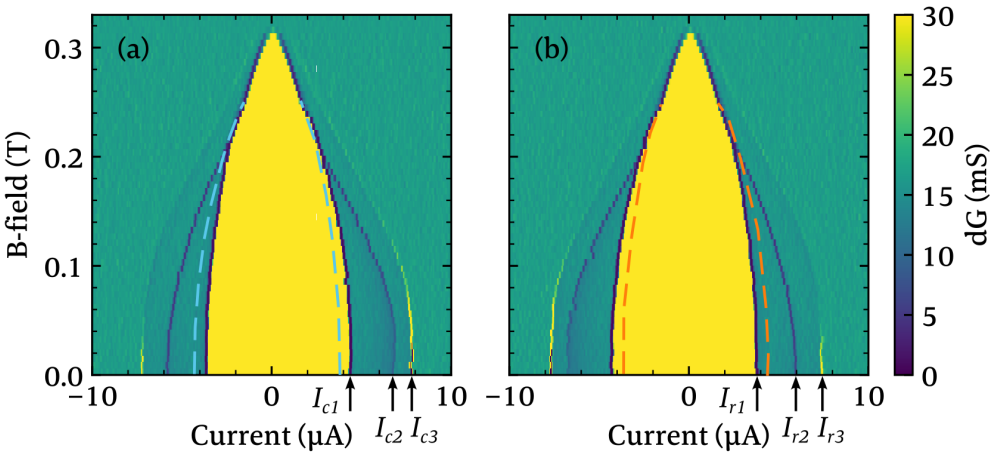

Figure 26: The color code represents the differential conductance dG calculated from the data shown in figure 23. Comparison of the transport properties for a bias current down-sweep in (a) and up-sweep in (b) to distinguish hysteretic from non-hysteretic parts. The measurement was performed at 379(11) mK and with a magnetic field resolution of 6 mT. The black arrows in (a) mark the critical currents I_{c1}, I_{c2} and I_{c3} and the black arrows in (b) the respective re-trapping currents I_{r1}, I_{r2} and I_{r3} of the different sample parts.

I_{c3} is clearly vanishing at B_c = 318 mT, whereas I_{c2} seems to vanish at a lower B-field. It seems that the apparent I_{c1} (red arrow) is a superposition of at least two superconducting parts of the sample. Under this consideration we posit that the hysteretic part follows the Fraunhofer pattern with a minimum at around 300 mT. A subsequent increase of the critical current would be counteracted by the orbital suppression of the applied B-field and finally vanish at B_c = 318 mT.

5 Dynamic Transport

When MW are irradiated into sample A1, various effects occur. For a high enough MW power, a trivial, monotonous reduction of S due to heating is expected. Although a S in equilibrium is free of dissipation, it is not for nonzero frequencies. There is always an electromagnetic field response of normal state QP and hence a finite dissipation. For a given MW frequency at a constant power, one would expect a constant dissipation in an ordinary S. That dissipation is visible in the reduction of I_c. The MW induced heating in our S-F-S heterostructures is discussed in section 5.1. Another suppression of S may be caused by a MW induced ac current in S which adds up to the transport current. A lower I_c should then be detected and may not be distinguishable from ordinary heating. The reduction of I_c by the amplitude of an ac current is called rectification. A direct break of Cooper pairs can be excluded because the photon energy $E_p = 165\,\mu\text{eV}$ of the highest possible MW frequency of 40 GHz, is below $\Delta \approx 212\,\mu\text{eV}$. The astonishing effects found in the present work are anomalous progression of $I_c(P)$, $I_c(B)$ and $R(T)$ under MW irradiation.

5.1 MW Induced Heating

To get a feeling how a potential ordinary MW heating would affect the various parts of the samples, a transport measurement for different temperatures, up to T_c without a B-field or MW, was performed on sample A2 as shown in figure 27. The dG values are cut off at 30 mS to highlight the line-like features. The bright region is in the range of dG = 100(20) mS. Besides the S/F parts, the SC in the fJJ region (S/FS part) is assumed to be weakened by the magnetic proximity effect the most and hence is expected to show the lowest T_c. The observation of the low T_c = 1.20(25) mK of the inner, high conductive part with I_{c1} of the fJJ, in comparison to the high T_c = 1.5 mK of the S part with I_{c3}, fits to the picture of the different samples parts. T_c of I_{c2} is around 20 mK lower than T_c of I_{c3}. The T_cs align with the steps in the R-T-measurements in section 4.4. I_{c2} and I_{c3} have a non-monotonous behavior with respect to T and a maximum at T = 675(75) mK which are 1% to 4% higher compared to the I_cs at T_{base} = 365 mK. Up to now we have no explanation for that behavior. Besides the slight increase of I_{c2} and I_{c3}, the trend is a reduction of the same for increasing T.

Another method to check for a MW induced heating is to track the thermometer at the sample holder during a MW irradiation on the sample. Figure 28 shows the color coded differential conductance dG of sample A2 for differ-

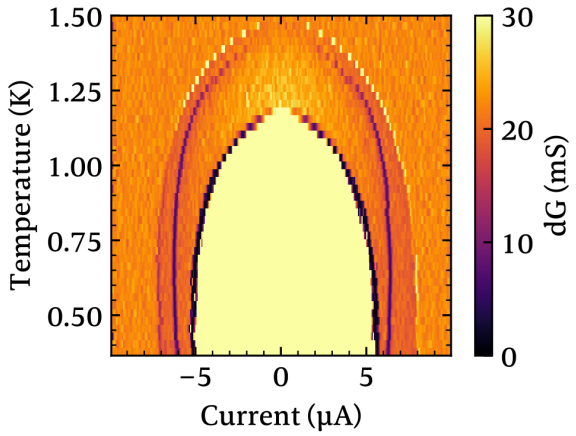

Figure 27: Sample A2: Differential conductance dG vs bias current for different temperatures of step size $\Delta T = 25(13)$ mK. The dG values are cut off at 30 mS to highlight the line-like features. The bright region is in the range of dG = 100(20) mS.

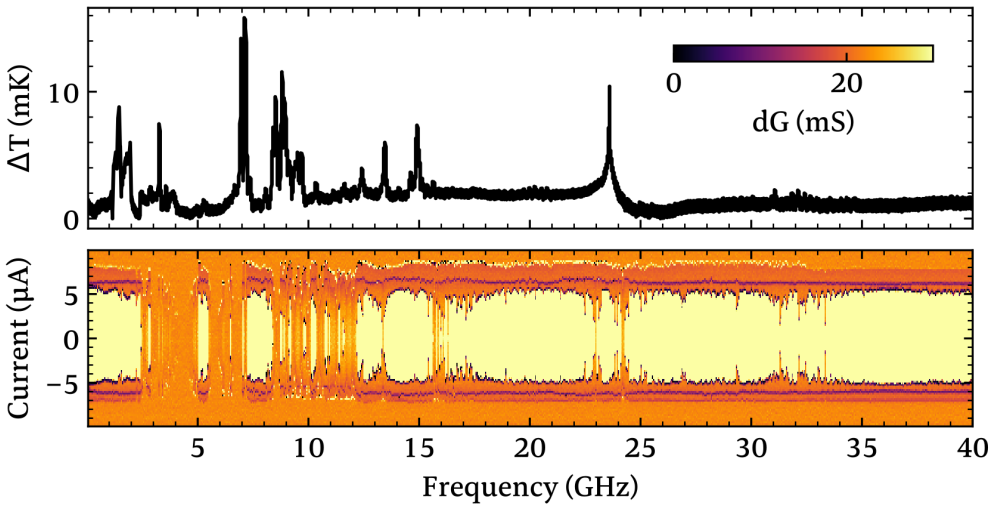

Figure 28: The temperature difference ΔT with respect to T_{base} of the sample holder during irradiation of various MW. Each frequency was irradiated on sample A2 for 30 seconds.

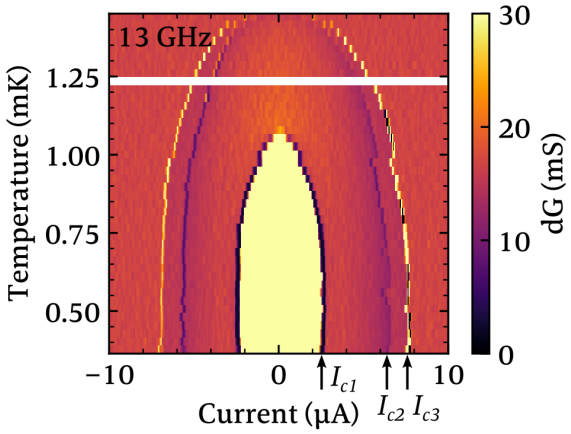

Figure 29: Sample A1: dG vs bias current for different temperatures of step size 25(3) mK and constant $B = 10$ mT and constant MW of 13 GHz, BW 1 kHz, power -20 dBm. White line is a lack of data points for $T = 1.25$ K. Black arrows indicate the critical currents I_{c1}, I_{c2} and I_{c3} of different sample parts.

ent frequencies of 50 MHz to 40 GHz in 50 MHz steps. Each frequency was irradiated for 30 seconds with the same MW output power of $P = -25$ dBm. ΔT is the temperature difference with respect to the base temperature T_{base}. There is no clear correlation between the increase in T with the suppression of S, for example between 10 GHz and 12 GHz. ΔT does not show pronounced peaks but the high conductive part is suppressed, whereas the line-like features are not. This speaks against an ordinary heating effect. In contrast to that, the suppression of S around 4 GHz might be due to local heating because all dG features are suppressed simultaneously, although, the global temperature of the sample holder is not increased significantly.

As a comparison, figure 29 shows dG for a 13 GHz MW irradiated on sample A1 for different temperatures as well. The general trend of $I_c(T)$ is the same as in figure 27 without MWs. Comparing the I_cs in figure 29 at $T = 364$ mK with the I_cs in figure 18 without any MW, one finds a reduction I_{c2} of 1% to 4%, whereas I_{c1} of the high conductive part (yellow area) is reduced by 34%. If the MW irradiation would already introduce some heat into the sample, figure 29 should be comparable to the higher T-range of figure 27. This means an immediate reduction of the I_cs could be expected for increasing T. But this is not the case. The I_cs stay constant up to 750 mK and it even looks like I_{c1} of the

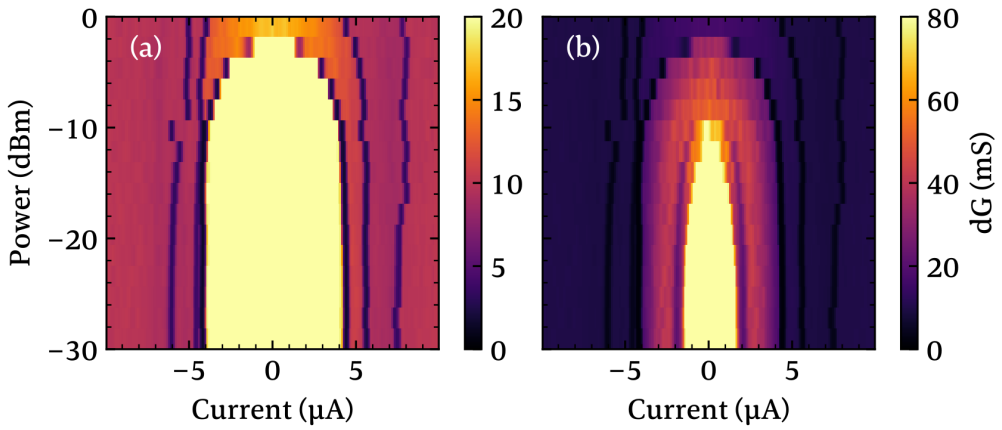

Figure 30: Sample B1: Differential conductance dG vs bias current for different MW powers of 40 GHz taken at $T = 354(6)$ mK. (a) and (b) are the same data but different scale of the color code for dG to highlight different features.

high conductive part rises a bit with a maximum at around $T \approx 600$ mK. With a MW frequency of 13 GHz applied, the sample seems to be in a different but stable state up to a temperature of 750 mK. On the other hand, the coupling of the MW into the different sample parts seems to be different as we related the high conductive regime with I_{c1} to the S/FS part (fJJ) and the line-like feature with I_{c2} and I_{c3} to the bare S parts in section 4.3.

For a 40 GHz irradiation on sample B1, shown in figure 30, the impact of the MW power on I_{c1} looks like the temperature dependence in figure 27. The line-like features do not follow a clear trend. There is some increase in $I_c(P)$, some steps and even some slight oscillations. The latter are produced by the 13 GHz in figure 29 as well. Besides that, the MW power below -20 dBm output power seems to be too weak for an impact and not high enough at 0 dBm to suppress the SC in the sample B1.

All in all the MWs reduce I_{c1} of the fJJ in the S/FS region monotonically when a certain MW power is exceeded. This is most likely due to local heating because the reduction of $I_{c1}(P)$ follows the same trend as $I_{c1}(T)$ in figure 27. The influence of the MW power on the line-like features I_{c2} and I_{c3}, which originate from the bare S parts, is non-monotonous. The next section deals with this effect in more detail.

5.2 Microwave Stimulated Superconductivity

The previous section gave a hint towards a non-monotonous $I_c(P)$ correlation. For almost all $I_c(P)$ measurements in this section 10 mT were applied. The idea of that is a preferential direction of the magnetization of Co along the external B-field and hence perpendicular to the alternating b-field component of the MW. This ac b-field then might stimulate the magnetization of Co to precess around the external B-field. According to [23], stimulated magnons cause an enhancement of the supercurrent through the fJJ and is an indirect measure of spin triplet superconductivity. Besides that, the 10 mT are not expected to alter the S state in a significant manor.

Under certain conditions an increase of I_c with respect to the MW power can be observed for the sample parts which are not related to the fJJ. Especially sample A2 shows a clear increase of I_{c2}, and, for some frequencies under special circumstances, also for I_{c3}. A selection of data for different parameters is given in figure 31. Figure 31(a) shows a clear increase of I_{c2} of 11%, whereas I_{c3} stays pretty constant over a wide range of MW power. This behavior persists for a B-field of 100 mT depicted in figure 31(b), although the increase of I_{c2} reduces to 4%. Both measurements were taken with the VNA output port 1, a MW BW of 1 MHz and a MW frequency of 21.8 GHz. The same parameters but for a different MW frequency of 6 GHz lead to the qualitatively same behavior of I_{c2} and I_{c3} in figure 31(d) with an increase of I_{c2} by 6%.

A remarkable change occurs when the BW is set to 10 Hz, what is shown in figure 31(c). I_{c2} rises even higher by 17% but only for increasing bias currents and I_{c3} rises by 18% for an increasing MW power until it drops to 0 immediately at -12 dBm. The simultaneous change of the output port of the VNA might play a minor role in the change of the I_{c3} behavior, although the different ports lead to a different MW coupling to the sample, as shown in figure 13 (sec. 3.2), because changing the BW with steady output port gives a reliable transition of a non-monotonous I_{c3} behavior to a monotonous one. This can be seen in figure 32 for a MW frequency of 21 GHz. Figure 32(a) shows a dG measurement with 10 Hz BW which is pretty much the same as for a BW of 10 kHz, shown in figure 32(b). However, a BW of 10 MHz does not increase I_{c3} for an increasing P. The emergence of a non-monotonous I_{c3} thus depends on a BW $\leq$ 10 kHz.

Around -14 dBm in figure 32(b), the conductance is reduced compared to -15 dBm, what is marked with a white arrow. This feature appears due to the fact that the bias current was swept from -10 µA to +10 µA in combination of I_{c3} exceeding the maximum bias current. The almost equivalent data in figure

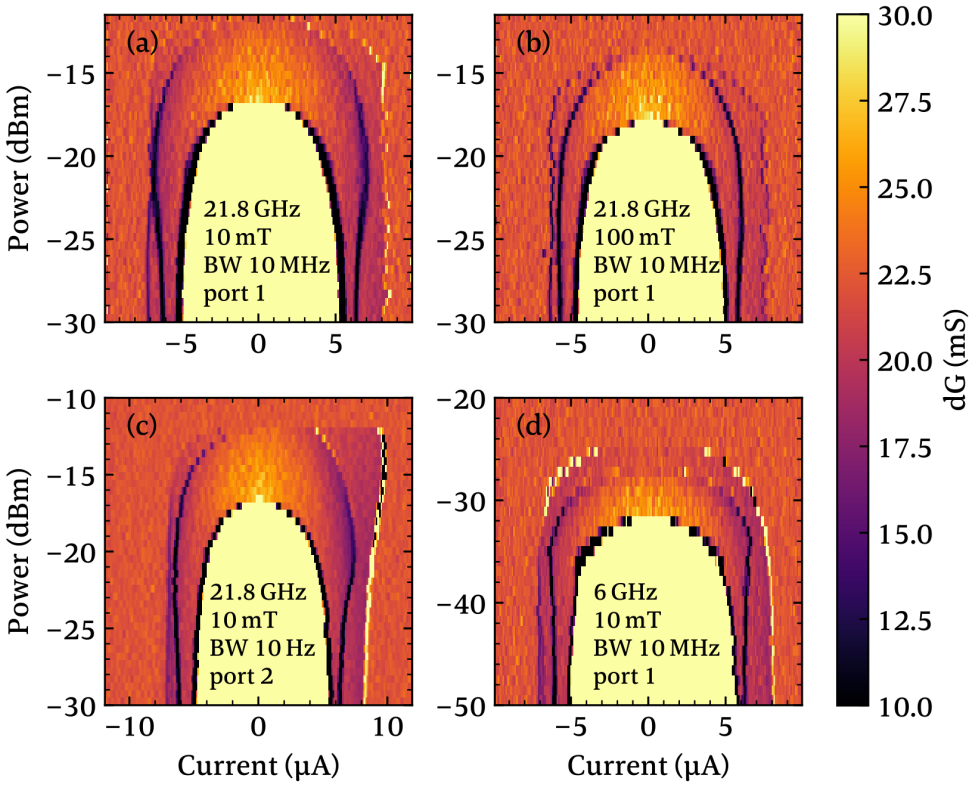

Figure 31: Differential conductance dG measurements on sample A2 for different MW frequencies, band widths (BW), B-fields and MW power output ports of the VNA (port 1/2). All measurements were performed below 361 mK and with a bias current up sweep. dG vs MW power of 21.8 GHz (BW 10 MHz) and B = 10 mT in (a) and B = 100 mT in (b). Change of BW to 10 Hz and port 2 in (c). 6 GHz at port 1, B = 10 mT and BW 10 MHz in (d). Figure (a), (b) and (d) were taken with a bias current sweeping from -10 μA to +10 μA and (c) from -12 μA to +12 μA. The color code of dG is confined between 10 mS to 30 mS to highlight the line-like features.

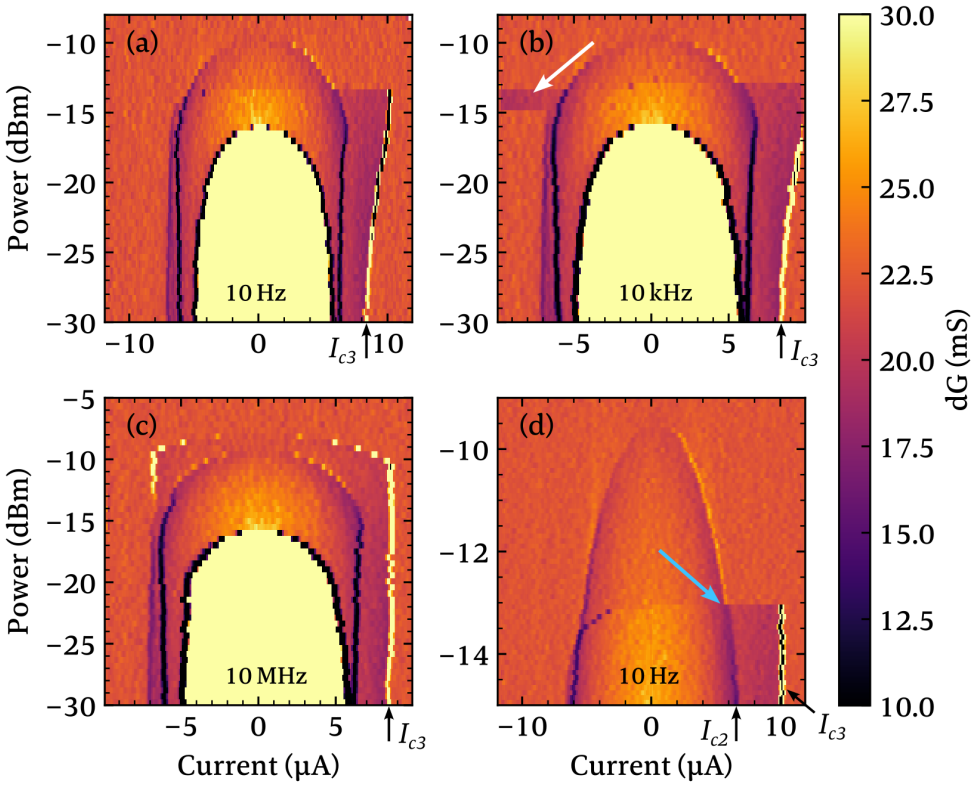

Figure 32: dG vs bias current and MW power with a 21 GHz MW irradiated into sample A2 for a BW of 10 Hz in (a), for 10 kHz in (b) and for 10 MHz in (c). (d) shows a measurement with the same parameters as in (a) around $P = 13$ dBm, where I_{c3} vanishes abruptly accompanied by a change of dG (blue arrow) along $I_{c2}(P)$. The step size is $\Delta P = 0.1$ dBm. The color code of dG is confined between 10 mS to 30 mS to highlight the line-like features. The critical current I_{c3} is marked with black arrows. The white arrow in (b) indicates a measurement artifact explained in the main text. All data were taken below 361 mK.

32(a) does not show that feature because it was taken with a bias current sweep from -12 µA to +12 µA.

To check if $I_{c3}(P)$ drops to 0 abruptly around $P \approx -13\,\mathrm{dBm}$, a measurement was performed with the same parameters as in figure 32(a) but with a power step size of $\Delta P = 0.1\,\mathrm{dBm}$, what is shown in figure 32(d). I_{c3} vanishes abruptly for increasing P within $\Delta P = 0.1\,\mathrm{dBm}$ at $P = -13\,\mathrm{dBm}$. The line-like feature, which is related to I_{c2}, appears to undergo a sudden change in dG from low (violet color code) to high values (orange color code) at $P = -13\,\mathrm{dBm}$. That change is marked with the blue arrow figure 32(d).

Plotting the data from figure 32(d) as I-V-curves, one obtains figure 33. The lowest I-V in figure 33(a) is taken with $P = -15\,\mathrm{dBm}$ and the topmost with $P = -9\,\mathrm{dBm}$. The curves are shifted by $\Delta I = 25\,\mathrm{nA}$ for clarity and the red I-V represents the data taken with $P = -13\,\mathrm{dBm}$. $I_{c2}(P)$ is assigned to the positive voltage jump for $P \leq -13\,\mathrm{dBm}$ which transits to a negative voltage jump for $P \geq -13\,\mathrm{dBm}$. This becomes more clear in the close-up in figure 33(b) where the I-Vs are shifted by $\Delta I = 18\,\mathrm{nA}$. Positive and negative voltage jumps lead to a step in R as shown in the transport measurements in figure 18(d). In summary, a step like increase of R at $I_{c2}(P)$ for low P turns continuously into a step-like decrease of R around $P = -13\,\mathrm{dBm}$ where I_{c3} vanishes abruptly. The step in R at highest bias current was assigned to a spin valve effect when SC sets in. The different sample parts seem to be correlated and not strictly independent of each other. This makes sense if one recalls the explanatory model in section 4.3. Three adjacent sample parts in series are able to form two JJs, wherein one part is shared by two JJs. This means, if one sample part turns N, the spin valve effect emerges at another sample part. The emergence appears continuously for increasing P and not abruptly as the color plot in figure 32(d) suggested.

Figure 32(c) shows the same $I_{c2}(P)$ and $I_{c3}(P)$ behavior as the measurements for other frequencies with a BW of 10 MHz in figure 31. $I_{c2}(P)$ is non-monotonous whereas $I_{c3}(P)$ stays rather constant except for slight fluctuations until it drops quite rapidly for increasing P.

A non-monotonous $I_c(P)$ has been reported for the first time already in the '60s by Wyatt et al. [30] on 200 nm thick tin films, on a 100 nm constricted tungsten wire by Dayem and Wiegand [31] and has been theoretically explained three years later by Eliashberg [32]. The effect could be confirmed on 100 nm Al strips by Pals and Dobben [87, 88].

If QP absorb additional energy from a photon, the Fermi distribution in equation (2) leads to an increase of Δ. Moreover, an increase of the QP energies moves the QPs away from k-states around the Fermi level which are now avail-

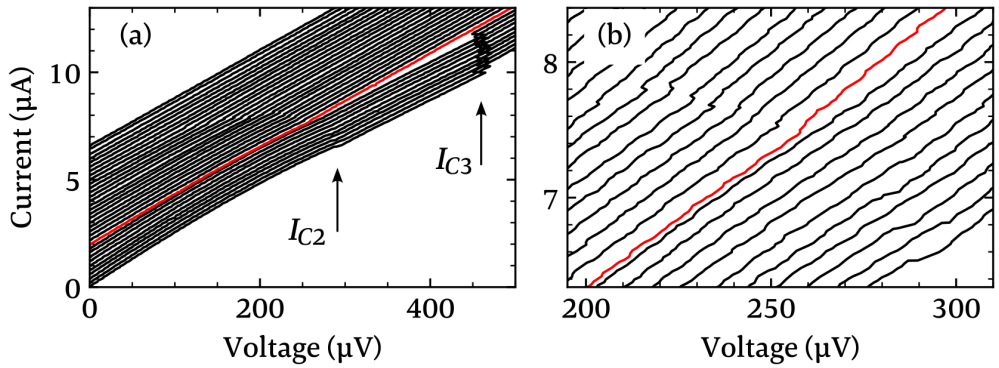

Figure 33: *I-V* measurement on sample A2 with 21 GHz MW (BW 10 Hz) irradiation for powers from -15 dBm (lowest *I-V*) to -9 dBm (topmost *I-V*) and a constant *B*-field of 10 mT. The data is the same as in the d*G* color plot in figure 32(d). The red line represents the *I-V* taken at -13 dBm MW power. (a) shows the positive bias current branch where the *I-V*s are shifted with respect to each other by $\Delta I = 25$ nA for clarity. (b) shows the green section from (a) around I_{c2} with an shift of $\Delta I = 18$ nA.

able for the electrons, which form Cooper pairs, to scatter into. This manifests itself in an increase of the condensation amplitude κ_k in equation (2) and additional k-states over which the summation is performed. Note that for $\hbar\omega < \Delta$ the Cooper pair density stays the same. Otherwise breaking of Cooper pairs would counteract the increase of Δ. A more visual description is a widening of the possible k-space over which Cooper pairs can be formed when the QPs are moved away from the Fermi level by the MWs. This stabilizes the S state without breaking it.

Eliashberg [32] calls this effect "MW stimulated superconductivity" and predicts a critical frequency ω_c over which this effect occurs and assumes a photon energy of $\hbar\omega < \Delta$. This could mean that there is an intermediate frequency at which the MW stimulated S is most pronounced. In fact Dayem and Wiegand [31] see a maximum of the increase of I_c for a certain frequency. This frequency seems to move to lower values for higher T. To see if the present measurements on sample A2 follow this trend, the maxima of $I_{c2}(P)$ and $I_{c3}(P)$ from a variety of transport measurements were plotted against the MW frequency and are shown in figure 34. The upper two figures (a) and (b) show $I_{c2}(f)$, the lower two (c) and (d) show $I_{c3}(f)$. The measurements from the left two figures (a) and

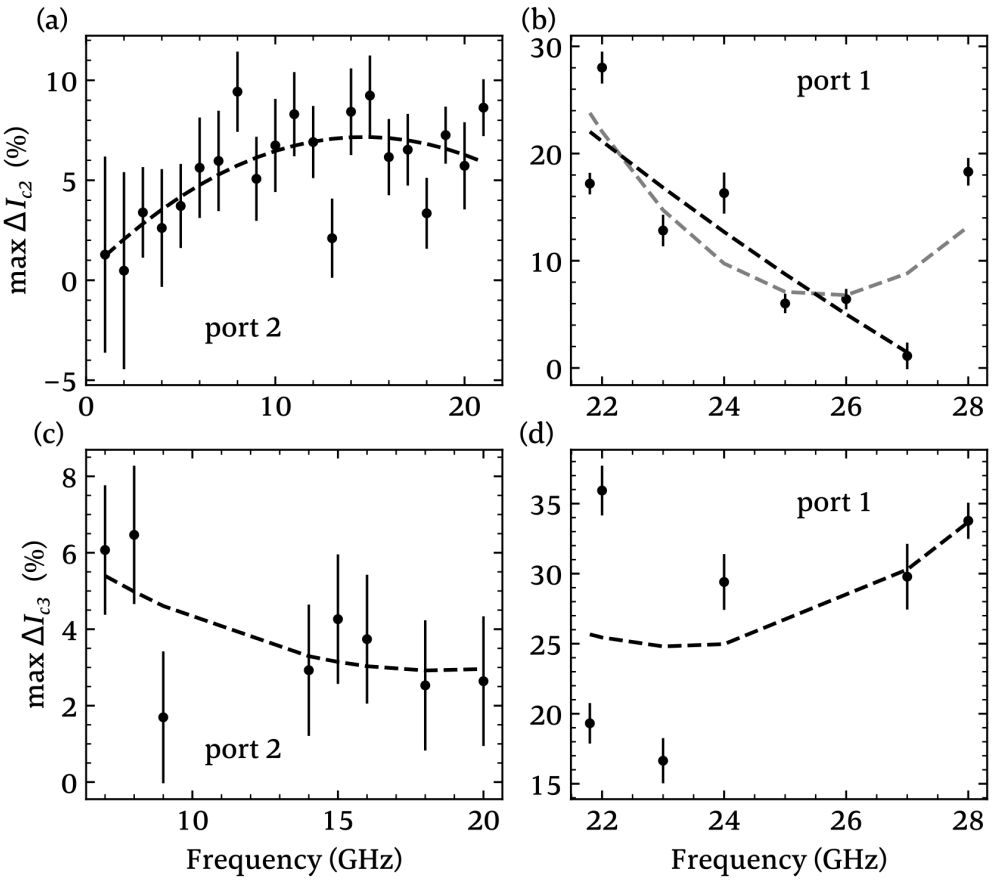

Figure 34: Maximum change of the critical current I_{c2} in (a) and (b) and I_{c3} in (c) and (d) for various MW frequencies. The dashed lines are quadratic fits to highlight the trend. The gray dashed line in (b) is a fit to all data points in (b) whereas for the black dashed line the data point at 28 GHz is excluded. The data in (a) and (c) were taken with VNA output port 2, the data in (b) and (d) with output port 1. The vertical lines at the data points represents the uncertainty.

(c) were performed with the VNA output port 2, whereas in the figures (b) and (d) port 1 was used. It appears that the two different ports lead to a different increase of $I_c(f)$ which we interpret as a different coupling of the MW to the sample. For low MW frequencies incident from port 2 in figure 34(a), I_{c2} is enhanced up to 10%. For higher frequencies and port 1 the increase is even higher, up to 28%. The maximum I_{c3} for high frequencies and port 1 exceeds 35%. Even within the same set of parameters, the data points seem to be randomly distributed at first glance. A quadratic fit shall reveal a trend of $I_c(f)$. Having a look on the data of $I_{c2}(f)$ in figure 34(a), the fit depicted in dashed lines suggests a maximum of $I_{c2}(f)$ between 10 GHz to 20 GHz. For higher frequencies in figure 34(b) the gray dashed fitting curve gives a minimum in $I_{c2}(f)$. This may be due to the low number of data points together with their high variation. Treating the last data point at 28 GHz as an outlier and neglecting it, leads to the monotonous black dashed fitting which continues the trend of figure 34(a) with a maximum $I_{c2}(f)$ value. This trend has also been reported by Dayem and Wiegand [31]. The present enhancement of I_{c2} seems quite clearly to originate from the MW stimulated superconductivity described by Eliashberg [32].

In contrast to that, the evolution of $I_{c3}(f)$ seems to follow the inverse trend of $I_{c2}(f)$. This means there is a minimum increase of $I_{c3}(f)$ between 17 GHz to 24 GHz. It appears as if the stronger the increase of $I_{c2}(f)$, the weaker the increase in $I_{c3}(f)$. This observation supports the assumption of coupled sample parts as discussed in figure 33. Up to now the actual mechanism of the coupling between the sample parts is unclear, though.

In summary, the former observations showed quite clearly an enhancement of I_c mediated by the MW Power. Yet it is not obvious to see this effect. Sample A2 showed the most pronounced increase in $I_c(P)$ whereas this effect is weaker in sample A1, although the nominal structure of sample A1 and A2 is the same. Remember the different integration of the WG on the samples and the temporary exposure to ambient conditions. This can explain the change of the $I_c(P)$ behavior from sample A1 to A2 since literature also reports a change of the $I_c(P)$ behavior for a varying immersion of their samples in vacuum, helium gas and liquid helium [87]. The sensitivity of $I_c(P)$ on the environment of the sample may also explain the huge variety of the data points in figure 34 because the different measurements were performed over days and within different condensing sessions of the cryostat. In contrast, an even more peculiar non-monotonous behavior of I_{c1} with respect to the external B-field was observed in sample A1 and is discussed in the following section.

5.3 Unusual Critical Current Behavior

5.3.1 Non-Monotonous Critical-Current-vs-B-Field Dependence

Applied B-fields of the order of a few percent of B_c are not affecting the critical currents in a detectable way, like shown in figure 35(c) when no MW is applied. This figure depicts the section around -20 mT to +20 mT and is comparable to figure 35(a), where B goes from 0 mT up to 237 mT. This is an extraction from the data set discussed already in figure 26(a). When additionally MW of 13 GHz are irradiated, sample A1 shows a strong suppression of I_{c1} for B-fields from 0 mT up to 17 mT, as depicted in figure 35(b). Figure 35(c) shows the section around $B = \pm 20$ mT of the same data set as in (b). The black dashed line indicates $B = 0$ mT to highlight the shift of the I_{c1} suppression by 1.5 mT. This suppression is due to a magnetization of Co. The coercive field of thin Co is expected to be at least around 2 mT since this is the typical size at room temperature for Co thicknesses of 15 nm to 100 nm [60]. Lower thicknesses are expected to keep this coercive field since literature shows a bulk behavior of Co down to 1 nm [59]. For low temperatures the coercive field of Co is around 6 mT [61]. In figure 35(b) and (d), I_{c1} grows for rising B-fields from 0 mT to 17 mT and stays constant at $I_{c1} = 2.5$ µA up to 70 mT. This is highly unusual since an additional B-field is expected to suppress S even further. I_{c2} shows a similar trend but weaker while I_{c3} stays almost unchanged.

Before we analyze this effect more deeply, a more profound correlation between the I_cs and the different sample parts can be made already with the present findings. Starting from the established assumption that I_{c1} stems from the fJJ, which is formed by the two S/FS parts, the logical conclusion is that I_{c2} is linked to a JJ formed by one of the S/FS parts together with a S/F part. Obviously, this must be the S/F part whose S is not suppressed completely. The $R_{res} = 13.5\,\Omega$ of sample A1 fits to the magnitude of the semi theoretically calculated $R_{S/F}^{A1} = 10.8\,\Omega$ of the narrower S/F part in table 4. This is the one expected to stay N under any condition and thus explains the reduced amount of steps in the I-Vs compared to the conceivable amount of JJs, discussed in section 4.3.

If the B-field in figure 35(b) rises even higher, another striking observation can be made. There is a sudden increase of I_{c1} at $B = 145$ mT (green arrow). Such steps appeared rather randomly throughout all $I_c(B)$ measurements performed within our work and their origin is not clear. Section 5.3.3 summarizes the observations on the steps. The kink in the $I_{c1}(B)$ at $B = 163$ mT, which is marked with the red arrow, stems from the concatenation of two different data

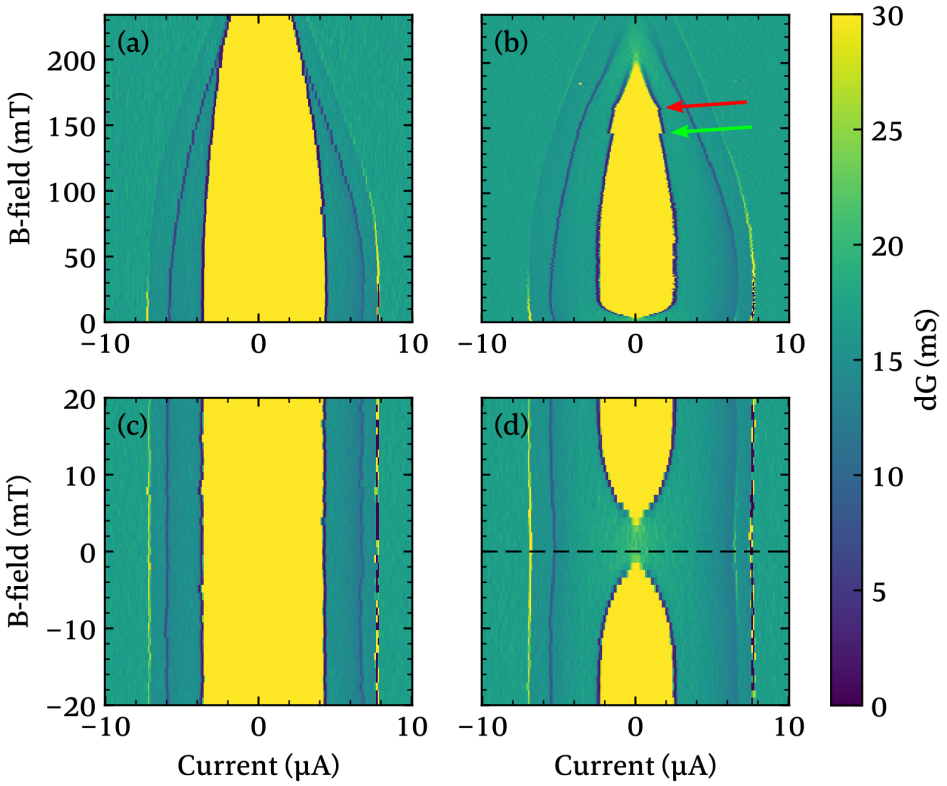

Figure 35: Sample A1. Differential conductance dG vs bias current and external magnetic field. (a) Same data as in figure 26 without any MW but limited to $B = 237\,\mathrm{mT}$ for a better comparability with (b). (b) Constant MW irradiation of 13 GHz, BW 1 kHz, port 2, power -19 dBm measured at $T \leq 389(25)\,\mathrm{mT}$. Red arrow marks $B = 163\,\mathrm{mT}$ where two measurements from two different days were concatenated. Green arrow marks a step in I_{c1} at $B = 145\,\mathrm{mT}$. (c) Measurement around $B = \pm 20\,\mathrm{mT}$ without MW, taken at $T \leq 374(3)\,\mathrm{mT}$ (d) Part of measurement in figure 35 around $B = \pm 20\,\mathrm{mT}$. Black dashed line marks $B = 0\,\mathrm{mT}$ to highlight the shift of the I_{c1} suppression by 1.5 mT.

sets, taken at different days.

The suppression of I_{c1} around $B = 0\,\mathrm{mT}$ can be observed for many frequencies but not for all. It even appears that there are certain frequency ranges for which this effect appears, while for other ranges, $I_{c1}(B)$ is monotonous. Some examples for a non-monotonous $I_{c1}(B)$ for different MW frequencies are depicted in figure 36. Figure 36(a), (b) and (c) show a complete suppression of I_{c1} around $B = 0\,\mathrm{mT}$, while in figure 36(d) a finite $I_{c1}(0)$ remains. The remaining $I_{c1}(0)$, however, can be suppressed completely for an increasing MW power as other measurements on sample A1 with a MW frequency of 15.5 GHz prove. It is a general trend that, as long as a non-monotonous $I_{c1}(B)$ behavior is observeded, $I_{c1}(B = 0)$ can be suppressed completely for a sufficent MW power, while I_{c2} and I_{c3} persist. Figure 37 shows the evolution of $I_{c1}(B)$ for a MW frequency of 5.2 GHz and varying power from -28 dBm in figure 37(a) to -31 dBm in 37(d). For -28 dBm, no high conductive branch and thus no I_{c1} can be observed, whereas I_{c2} and I_{c3} are visible. B_c for the latter two is reduced by around 30% compared to no MW irradiation in figure 26. For lower MW power in figure 37(c) and (d), $I_{c1}(B = 0)$ is reduced compared to its respective maximum.

All measured I_cs for any applied MW frequency never exceed the I_cs measured without MWs. We think that the MWs induce a local heating which is not necessarily reflected in the thermometry. This heat reduces the I_cs and especially I_{c1} the strongest. For most of the frequencies above 30 GHz, it appears that a MW heating destroys S before a non-monotonous $I_{c1}(B)$ behavior can be observed.

If the values for I_{c1} in the positive bias current branch are plotted against the B-field for different MW power, one obtains the graph in figure 38. The maximum I_{c1} is slightly shifting from 50 mT to around 43 mT for decreasing MW power. The $I_{c1}(B)$ graphs in figure 38 are comparable to a measurement performed by McCarthy and Warman in 1974. They investigated an Al bridge of similar dimensions as the samples at stake [34]. Their samples were made out of granular Al. However, they do not see the expected tunnel transport characteristics. Their explanation for an initial suppression of I_c for low B-fields goes as follows. An incident MW creates ac currents in the Al which are strong enough to overcome I_c. An additionally applied B-field creates quantized flux vortices through the Al. An increasing number of vortices for an increasing B-field will increase the surface impedance of the Al bridge which reduces the coupling of the MW into the Al. This reduces the ac currents and thus restores S. Their main measurements were shown with a B-field applied perpendicular to their Al bar, which easily could explain the creation of flux vortices. In our

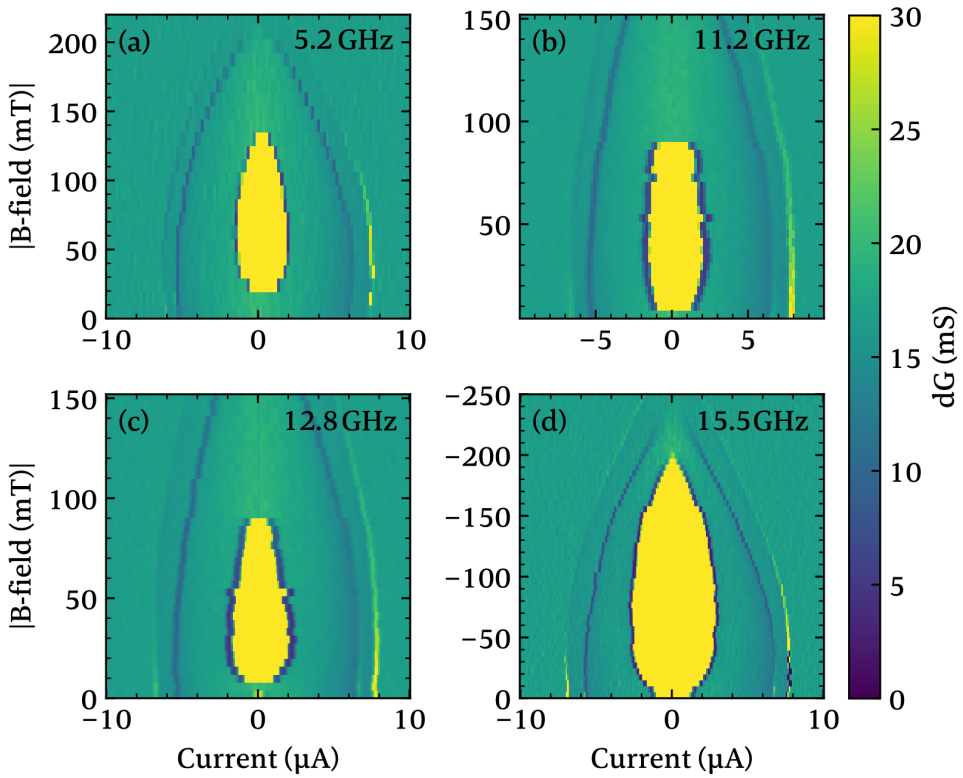

Figure 36: Sample A1. dG vs bias current and B-field for different MW frequencies at port 2 with BW 1 kHz. (a) 5.2 GHz, power -29 dBm, T = 367(7) mK. (b) 11.2 GHz, power -23 dBm, T = 362(10) mK. (c) 12.8 GHz, power -18 dBm, T = 366(6) mK. (d) 15.5 GHz, power -23 dBm, T = 360(11) mK. Measurement was performed with B-fields applied in opposite direction.

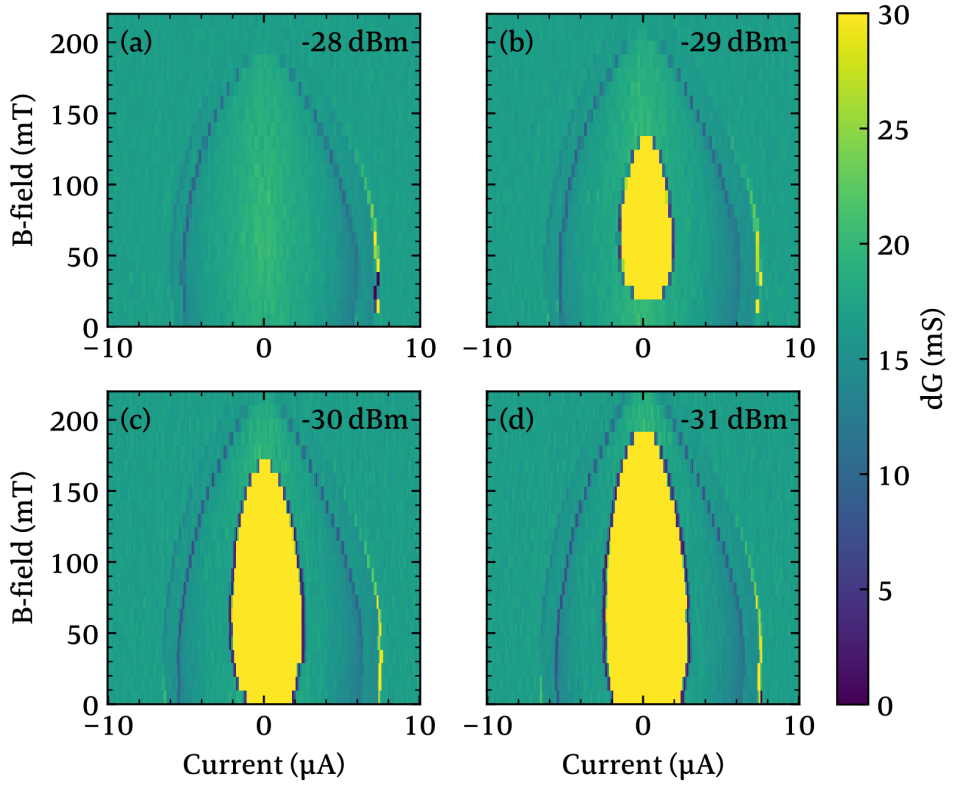

Figure 37: 5.2 GHz, BW 1 kHz, port 2 MW irradiation on sample A1 at T = 370(9) mK for decreasing MW powers from (a) to (d).

case the B-field is applied along the long axis of the samples. This makes flux vortices pining through the sample unlikely since our investigations showed $\lambda \approx 720\,\text{nm}$ compared to the 5 µm long sample. A slightly tilted sample against the B-field direction cannot be excluded, though. The change of the surface impedance and thus a worse MW coupling for an increasing B-field might be an unlikely but possible explanation for the non-monotonous $I_{c1}(B)$ behavior of our samples.

5.3.2 Anomalous Critical-Current-vs-B-Field Dependence

Whereas a MW frequency of 13 GHz clearly shows the non-monotonous $I_{c1}(B)$ behavior, an increase to 13.95 GHz somehow inverts this effect, as depicted in

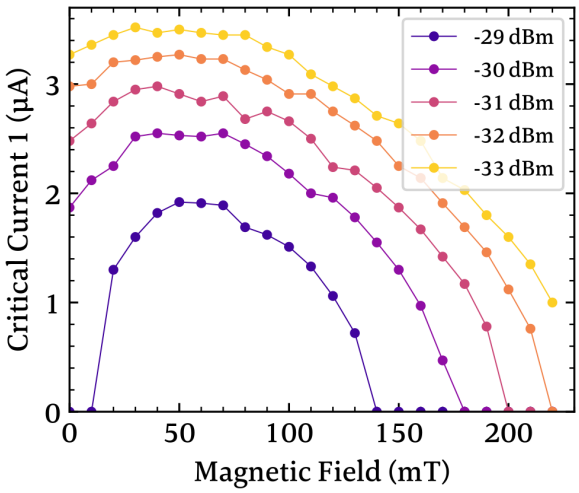

Figure 38: Critical current I_{c1} vs B-field measured at sample A1 for a 5.2 GHz MW irradiation with 1 kHz BW for different MW powers. The data was taken at $T = 370(9)$ mK.

figure 39. At $B = 0$ mT, I_{c1} is biggest but decreases quite rapidly for a rising B-field until I_{c1} is almost constant from $B = 35$ mT to 55 mT. Increasing the B-field even further, reduces I_{c1} in a smooth, monotonous way, like one would expect for no MW irradiation and an orbital depairing. The unusual rapid decrease of $I_{c1}(B)$ for low B seems to occur for frequencies from 13.9 GHz up to 14.2 GHz and counteracts the explanation of McCarthy and Warman. The sudden drop of I_{c1} at $B = 160$ mT in figure 39(d) is comparable to the sudden increase of I_{c1}, in figure 35(b) and yet to be discussed.

Similar to the B-field dependent transport measurements in figure 26 without any MW applied, the anomalous high-conductive part consists of a hysteretic and a non-hysteretic part, which is shown in figure 40, where a bias current up-sweep is compared to a down-sweep measurement with 13.95 GHz MW irradiation. Remaining with the assumption that sample A1 forms a fJJ in the S/FS part, the anomalous $I_{c1}(B)$ behavior seems to originate from that very fJJ.

Figure 36 and figure 39 showed that different MW frequencies lead to different d$G(B,I)$ characteristics with the two unusual $I_{c1}(B)$ behaviors of a non-monotonous or anomalous $I_{c1}(B)$. A possible functional dependence of I_{c1} from any parameter, such as B or the bias current I, is thus not obvious. To make the transport measurements comparable, we define a reference I_{c1}^{ref} for

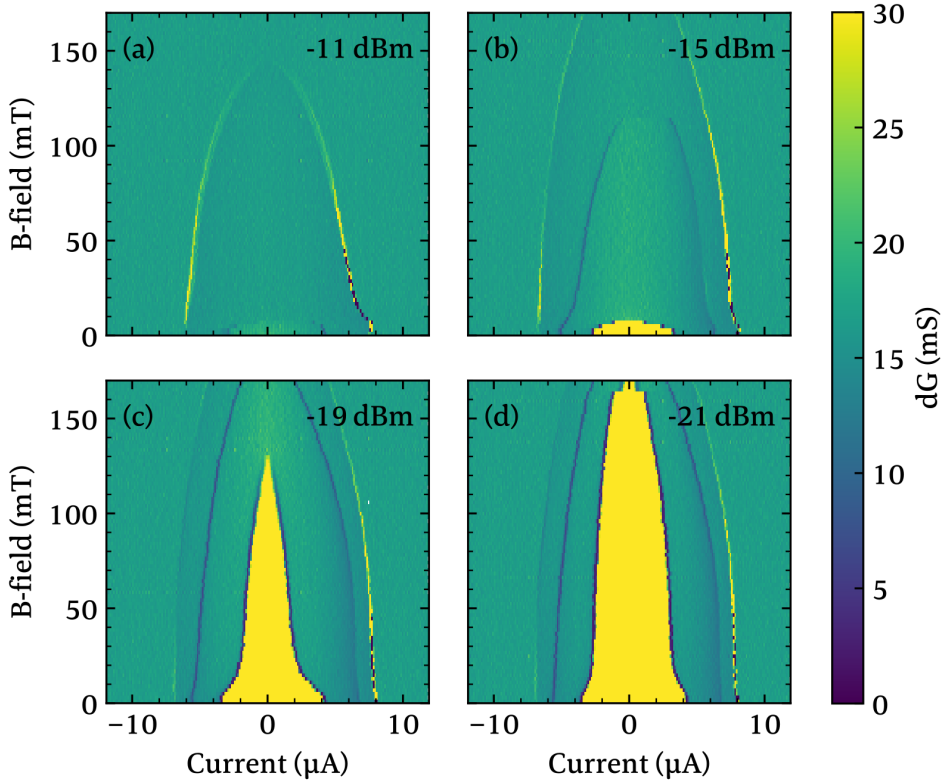

Figure 39: dG vs bias current and B-field for a MW frequency of 13.95 GHz and various power irradiated on sample A1 at $T = 384(14)$ mK.

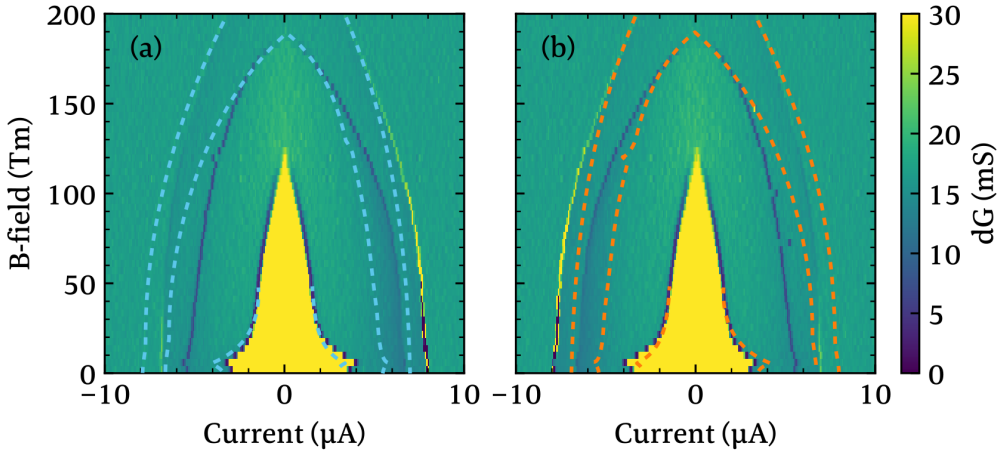

Figure 40: dG vs bias current B-field. Irradiation of 13.95 GHz at -19 dBm and 361(7) mK. Bias current up-sweep in (a) and bias current down-sweep in (b). The evolution of the $I_c(B)$s of (b) is drawn in (a) as blue dashed curves and the other way round in (b) with the orange dashed curve.

each individual MW frequency to normalize $I_{c1}(B=0)$. I_{c1}^{ref} shall be the $I_{c1}(B)$ value with the smallest slope. For example in figure 37, $I_{c1}^{\text{ref}} \approx 60\,\text{mT}$. The normalized $I_{c1}(B=0)$ thus is defined as $|I_{c1}(B=0)| = I_{c1}(B=0)/I_{c1}^{\text{ref}}$. If no unusual or non-monotonous I_{c1} behavior occurs for a specific MW frequency, the $|I_{c1}(B=0)|$ is 1. If a certain MW frequency leads to a non-monotonous I_{c1}, its $|I_{c1}(B=0)|$ is below 1 and even 0 if it is suppressed completely . A $|I_{c1}(B=0)|$ bigger than 1 means an anomalous decrease of $I_{c1}(B)$. The $|I_{c1}(B=0)|$ values for a variety of MW frequencies are plotted in figure 41(a). A blue bar reaching down to 0 corresponds to a dG signature like in figure 37(b), a blue bar between 0 and 1 corresponds to a dG signature like in figure 37(c) and a blue bar exceeding 1 corresponds to a dG signature like in figure 39(c).

Some measurements were conducted with a variation of the MW power. For some frequencies this leads to an evolution of the d$G(B,I)$ signature which is qualitatively comparable to the one in figure 37. In this case, the very measurement with the lowest MW power was chosen to calculate $|I_{c1}(B=0)|$, where $I_{c1}(B=0)=0$. For example, for an irradiation of 5.2 GHz, the data of figure 37(b) was chosen to calculate $|I_{c1}(B=0)|$ and take the respective MW power value for the comparison. If no complete reduction of $I_{c1}(B=0)$ was observed for any

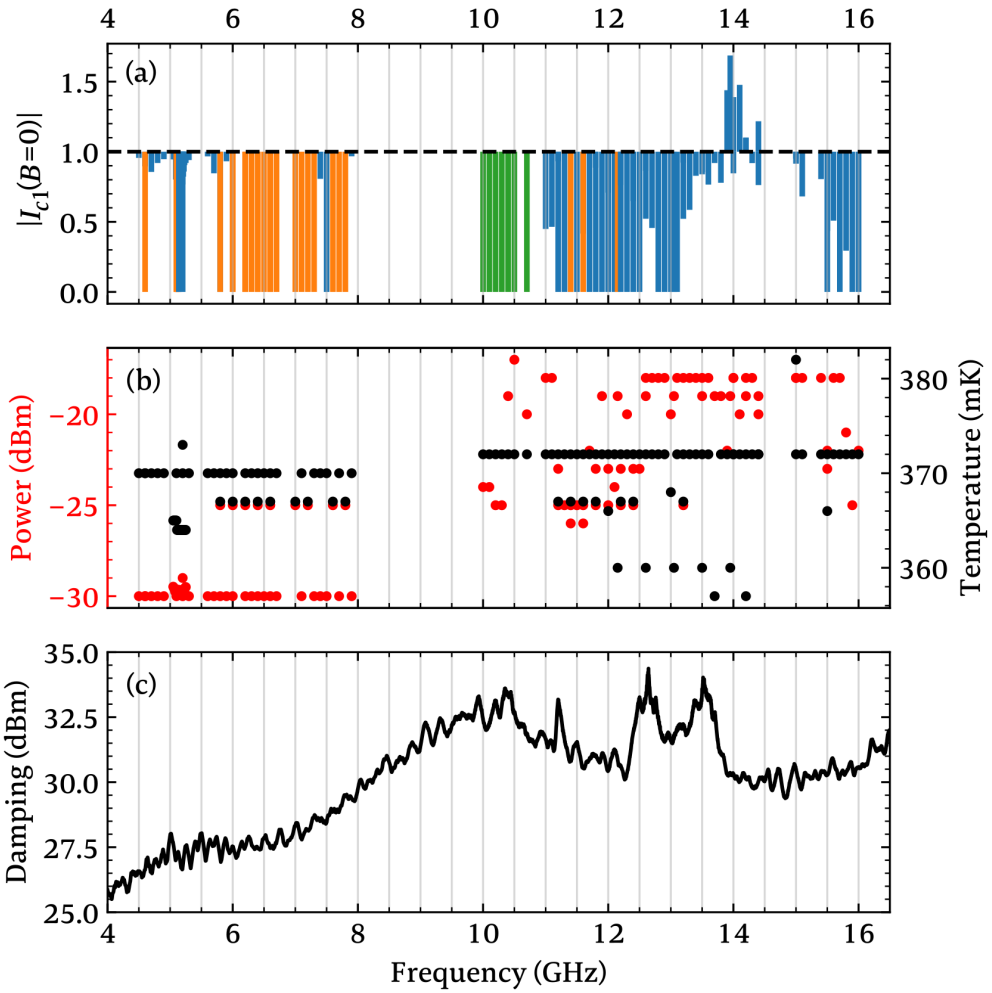

Figure 41: Normalized $|I_{c1}(B=0)| = I_{c1}(B=0)/I_{c1}^{\mathrm{ref}}$ of sample A1 for different MW frequencies in (a). A blue bar reaching down to 0 corresponds to a non-monotonous I_{c1} with $I_{c1}(B=0)=0$, a blue bar between 0 and 1 indicates a finite $I_{c1}(B=0)\neq 0$, a blue bar exceeding 1 represents an anomalous $I_{c1}(B)$, a green and orange bar stands for $I_{c1}(B)=0$ for all B-fields. The green indicated I_{c1}s evolve in a trivial monotonous way for decreasing MW power. See further descriptions in the main text. (b) MW power and temperature at which the corresponding data in (a) was measured. (c) Frequency response of the setup.

applied MW power, the power level was chosen at which $|I_{c1}(B=0)| = I_{c1}(B=0)/I_{c1}^{\mathrm{ref}}$ provides the biggest difference to 1. For some MW frequencies, no power level shows a non-monotonous I_{c1} but a complete reduction of I_{c1} for all B values, like shown in figure 42(a) and (b). These measurements are depicted as green bars in figure 41(a). The kinks in I_{c2} and I_{c3} and the steps in I_{c1} are artifacts from the concatenation of different data sets. These artifacts highlight the instability of I_{c1} when the MWs have weakened S drastically since the nominal parameters were the same for the different data sets but were taken at different days and between different cool downs of the cryostat.

Some measurements were performed just with a single MW power. If then a complete reduction of I_{c1} was observed, like in figure 37(a), its corresponding $|I_{c1}(B=0)|$ is plotted as an orange bar. This means for a decreasing MW power the corresponding frequency could either lead to a dG signature, like in figure 37(b), or I_{c1} would develop monotonously in a trivial way. Which evolution the d$G(B,I)$ signature of the sample would follow for a changing MW power is unknown. In any case I_{c2} and I_{c3} persisted.

In figure 41(b) the MW powers of the respective WM frequencies in figure 41(a) and the average T are plotted. Data points which lie on the same level normally stem from a measurement series where the same MW power was applied and the average T was calculated for the whole series. Deviations of T are normally in the range of a few mK.

Figure 41(a) shows a non-monotonous $I_{c1}(B)$ for the two ranges of MW frequencies from 4.5 GHz to 7.9 GHz and from 11 GHz to 16 GHz. The latter also shows a narrow frequency span of 13.85 GHz to 14.4 GHz where the anomalous $I_{c1}(B)$ behavior could be observed. For MW frequencies below 4.4 GHz down to the lowest measured value of 2 GHz, no unusual $I_{c1}(B)$ behavior was observed. One could think of 4.5 GHz to be the onset of the anomalous $I_{c1}(B)$ behavior. However, the ranges of 8 GHz to 10.9 GHz and 14.5 GHz and 14.9 GHz are also missing an unusual $I_{c1}(B)$. What instead can be observed in this ranges is the much stronger suppression of I_{c1} compared to I_{c2} and I_{c3}, like for 10.4 GHz in Figure 42(a). Here the I_{c2} and I_{c3} are reduced by around 11% for the negative bias current branch (current down-sweep) and around 2% in the positive bias current branch. A comparison to a transport measurement at $T = 1205(40)$ mK clearly shows a temperature dependent suppression of the different I_cs, what is depicted in figure 42(c). $T = 1205$ mK ist just 105 mK above the T_{c1} in figure 22. The high conductive part in figure 42(c) with the corresponding I_{c1} is suppressed completely while I_{c2} and I_{c3} persist but are reduced by around 25%. A homogeneous MW heating of the sample should lead to a stronger suppres-

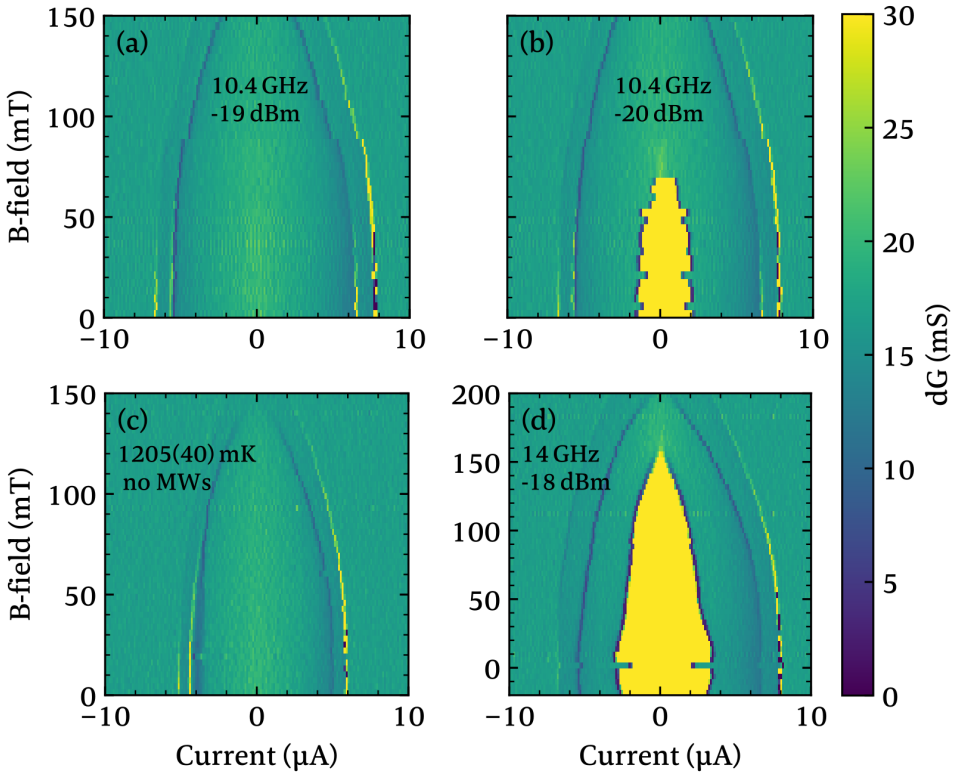

Figure 42: dG vs bias current and B-field for MWs of 10.4 GHz irradiated on sample A1 with a power of -19 dBm in (a) and in (b) with -20 dBm. Both data sets were taken at $T = 362(11)$ mT. The steps in $I_{c1}(B)$ in (b) are due to a concatenation of different data sets. (c) dG vs bias current vs B-field plot at $T = 1205(40)$ mK without any MWs applied. (d) Taken at 372(11) mK with MW of 14 GHz and -18 dBm.

sion of I_{c2} and I_{c3} comparable to figure 42(c). This supports the assumption of a local heating of the S/FS part by the MWs which suppresses I_{c1} the strongest.

Figure 42(d) is an example that around 14 GHz the I_{c1} withstands higher MW power up to -15 dBm compared to the low-frequency range with powers between -25 dBm to -30 dBm. A significant difference in the MW power, which is needed to drive sample A1 into an unusual $I_{c1}(B)$ regime, can also be seen in figure 41(b). Note that the power levels for frequencies higher than 12 GHz do not indicate the power where I_{c1} was suppressed completely, but rather were an anomalous I_{c1} was most pronounced. I_{c1} for 13.95 GHz for example is suppressed completely at -11 dBm (see fig. 39(a)). The damping of the MW cabling in figure 41(c) shows a difference between 6 GHz and 14 GHz of around 2.5 dBm and thus cannot explain the different power values of low and high frequencies needed to suppress I_{c1}. Literature reports a calibrated monotonically dependent I_c on the MW voltage [46]. This makes it reasonable to interpret the I_c reduction as a measure for the MW power coupled into the sample parts.

For the anomalous $I_{c1}(B)$ to occur, there must be an effect which stabilizes S in the S/FS part for frequencies around 14 GHz, whereas in the non-monotonous $I_{c1}(B)$ state, the MWs foster the suppression of I_{c1} for low B-fields even for low MW powers. Both effects are canceled for an increasing B-field. As both effects occur at $B = 0$ for any MW frequency, a magnetic resonant effect can be neglected. But they may depend on the magnetization of Co since its coercive field is in the low mT range. Kinsey et al. [61] report a shift of the critical current with respect to a B-field by the coercive field of Co in a Nb/Co bilayer structure.

To check if a magnetization plays a role in our samples, a demagnetized state needs to be defined. To do so the magnet and thus the Co were demagnetized by sweeping the B-field from negative to positive values and back and successively reducing the amplitude until the magnet ends up at $B = 0$ mT. Performing a transport measurement on the demagnetized sample with 5.2 GHz at -29 dBm for an increasing B-field results in the d$G(I,B)$ color plot in figure 43(a). This is basically the same result as in figure 37(b). A subsequent reduction of the B-field back to 0 mT reveals a slightly higher B_c by about 5(2) mT. Changing the B-field further to negative values, results in a shift of the $I_{c1}(B)$ onset to a lower B-field by 5(2) mT. This value is the coercive field of Co. A similar but smaller shift could already be observed in figure 35(d). Figure 43(d) is an overlap of the contours of the $I_{c1}(B)$ of the data in figure 43(a), (b) and (c) for a better comparability.

The black dashed line indicates a line cut through the data sets of (a), (b)

and (c) at 0.5 µA. The resistance is calculated out of the line cut data and depicted in figure 43(e). The colored arrows indicate the gradient of the B-field. In this representation, a hysteresis in R can be seen at the transitions between the high and the low resistive parts which we attribute to the magnetization of Co. Around 10 mT the hysteresis is expected because of the coercive field of Co. The hysteresis at $B \approx 130$ mT is a bit surprising. Changing the B-field from low to high values over this hysteretic part at 130 mT should not change the magnetization of Co anymore. Fluctuations of I_{c1} for such high B-fields have occasionally been observed and could cause the hysteresis at 130 mT to be an artifact.

5.3.3 Discontinuous Critical-Current-vs-B-Field Dependence

Some discontinuous steps in the $I_{c1}(B)$ characteristics appeared supposedly arbitrarily in the previously introduced results in figure 35(b), 39(d) and in figure 48(e), (f), (k) and (l). Since the SC was quite unstable in regimes where relatively high B-fields and MW where applied, the steps have been attributed to be fluctuations. This is most likely correct for the data shown in figure 42(b), since this data set is a concatenation of measurements from different days. However, a closer examination reveals a reproducibility of the steps for some parameter configurations. Figure 44 shows two different measurements with the same MW frequency of 15.5 GHz at -23 dBm and $T = 364(3)$ mK. This parameter set even reveals two steps at 152 mT (153 mT) and at 156 mT (157 mT) in figure 44(a) (figure 44(b)) which become visible due to the small B-field step size of $\Delta B = 1$ mT.

The majority of observed $I_c(B)$ steps jump from higher to lower I_{c1} values for an increasing B-field (positive step), like shown in figure 44. Some steps appear to jump from lower to higher I_{c1} values (negative step), especially for MW frequencies around 13 GHz as depicted in figure 35(b) (green arrow). Anticipating the results for the non monotonous $I_{c1}(B)$ behavior for different T in the following section 5.5, we refer to figure 48, where positive and negative steps appear and disappear as T increases. For 13.9 GHz a negative step appears at $T \geq 700$ mK, as can bee seen in figure 48(e) and (f). For 15.5 GHz and at low $T = 365$ mK (fig: 48(g)) there is a tiny positive step at $B = 115$ mT which moves to $B = 135$ mT for increasing T. This step disappears for $T \geq 600$ mK and a negative step appears for $T \geq 700$ mK.

Further measurements with 13 GHz reproduced the positive steps in figure 35(b) and display a shift of the steps to lower B-fields for an increasing MW

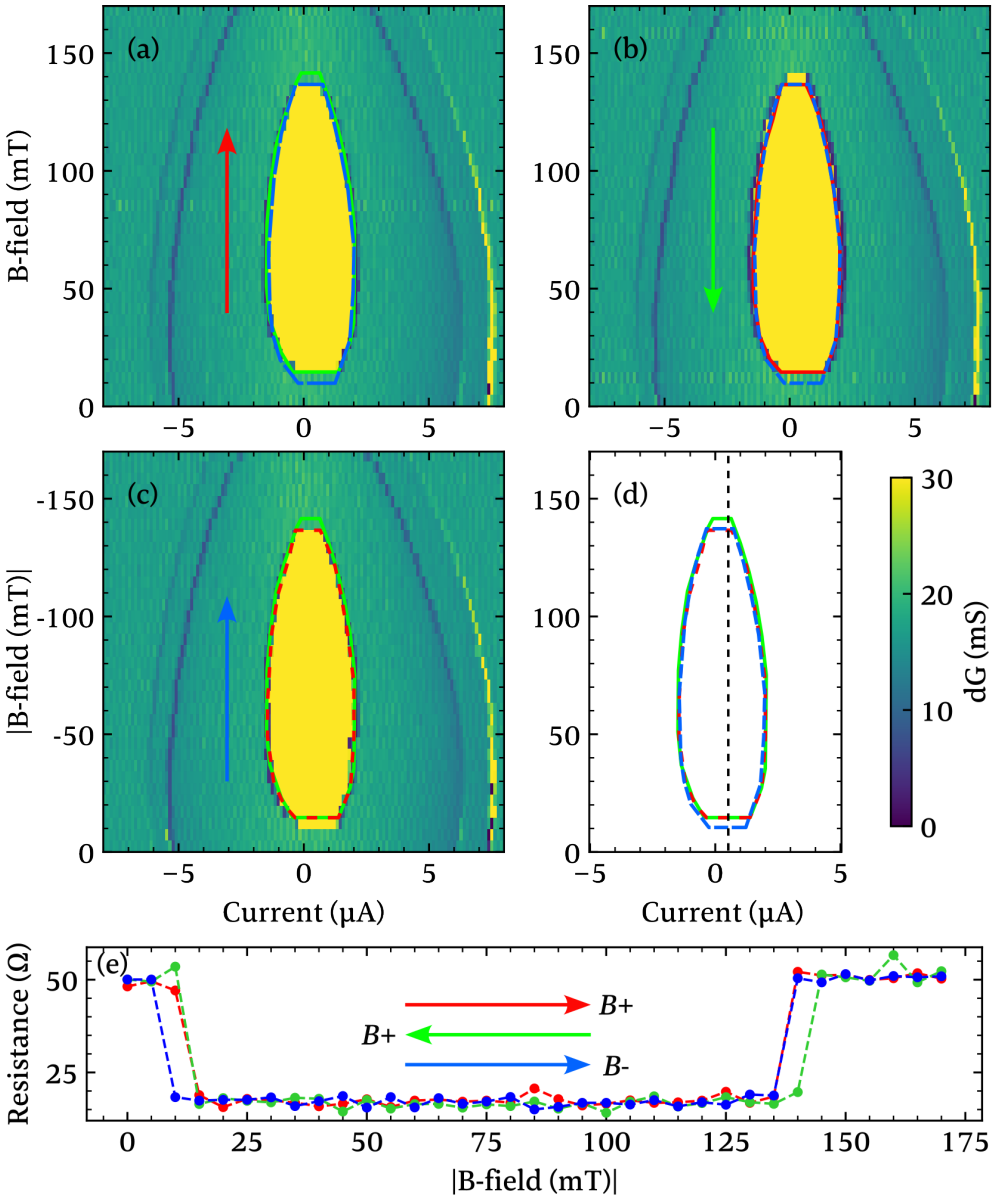

Figure 43: dG vs bias current and B-field in 5 mT steps under 5.2 GHz MW irradiation at 370(7) mK. Gradient of B-field change indicated by colored arrows. (a) Demagnetized sample measured for B-fields from 0 mT to 170 mT. (b) B-field change from 170 mT to 0 mT. (c) Opposite B-field direction change from 0 mT to -170 mT. (d) Overlap of I_{c1} contours from (a) in red, from (b) in green and from (c) in blue. (e) Line cut through (a), (b) and (c) at 0.5 μA.

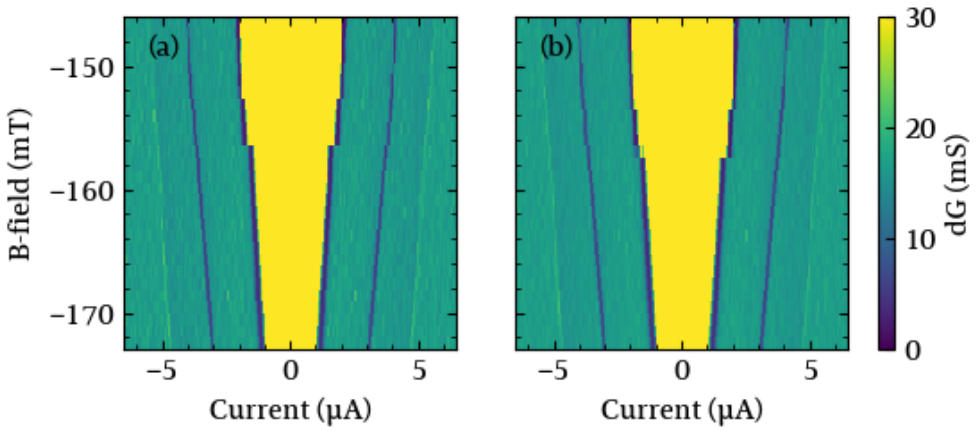

Figure 44: Differential conductance dG vs bias current and B-field under 15.5 GHz MW irradiation with $P = -23$ dBm at 364(3) mK in (a) and at 363(1) mK in (b).

power P as is depicted in figure 45(a) for $P = -20$ dBm and in figure 45(b) for $P = -19$ dBm. A extreme form of a discontinuous $I_{c1}(B)$ was observed for a MW frequency of 30 GHz which is depicted in figure 46 and confirms the P-dependent shift of the steps. Besides the P dependent shift, P also increases the step height. For -18 dBm in figure 46(a) a small step in $I_{c1}(B)$ appears at around 200 mT followed by a quite fast reduction of I_{c1} for an increasing B-field. The critical current of a S/F part (I_{c2}) of the sample also shows a discontinuous step. The step height of $I_{c1}(B)$ rises for increasing P until I_{c1} is completely suppressed for $P > -14$ dBm and $B > 185$ mT (figure 46(c) and (d)). This abrupt suppression of I_{c1} moves further to lower B-fields accompanied by an onset of a discontinuous step in I_{c3} at $P \geq -8$ dBm (figure 46(d)). For even higher P, all critical currents (I_{c1}, I_{c2}, I_{c3}) disappear abruptly at $B \lesssim 110$ mT (figure 46(e) and (f)). In figure 46(f), $P = 0$ dBm lead to an increase of $I_{c2}(B)$ for an increasing B-field until the complete suppression of all I_cs at $B = 80$ mT which is reminiscent of the MW stimulated SC in section 5.2. The difference, however, is a maximum of $I_{c1}(B)$ at higher B-field at constant P compared to a maximum of $I_{c2}(P)$ at higher P with low constant B-field in the MW stimulated SC. Measurements with 30 GHz at -18 dBm were performed with a decreasing B-field which led to the very same result as in figure 46(a). The B-field sweep direction hence has no influence on the discontinuous $I_{c1}(B)$ behavior.

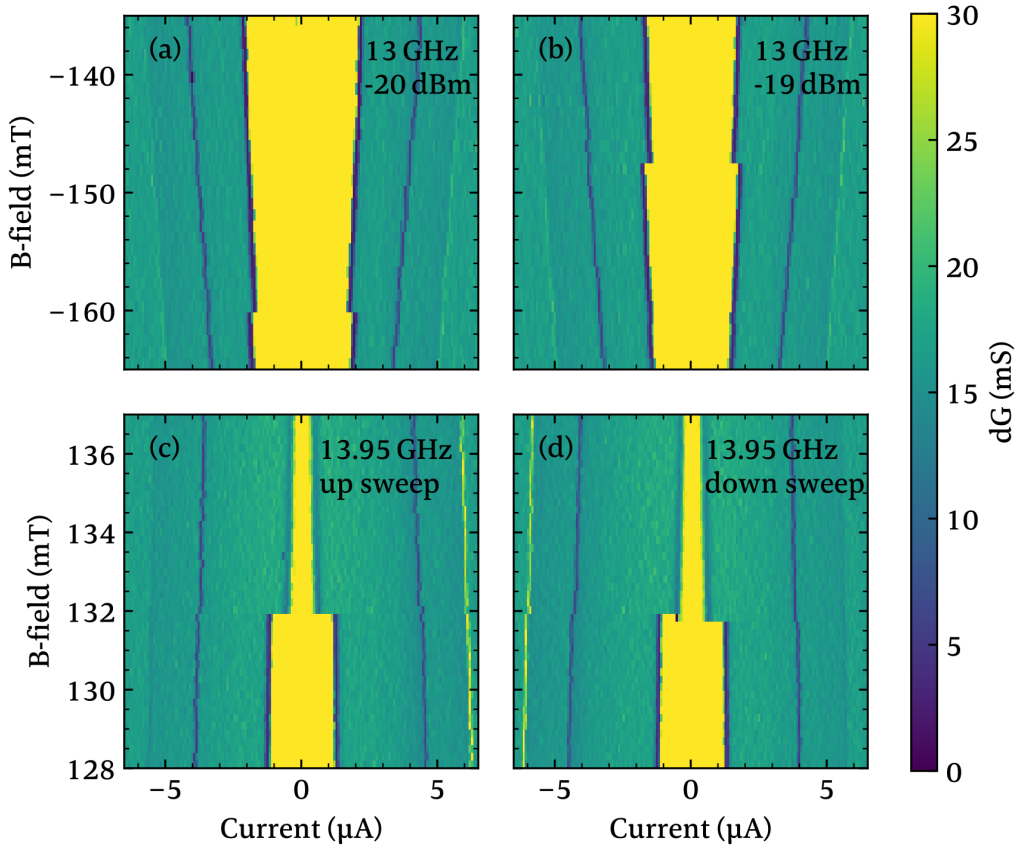

Figure 45: Differential conductance dG vs bias current and B-field for 13 GHz MW irradiation at -20 dBm in (a) and at -19 dBm in (b). 13.95 GHz at -19 dBm with bias current sweep from negative to positive values (up sweep) in (c) and with sweep from positive to negative values (down sweep) in (d).

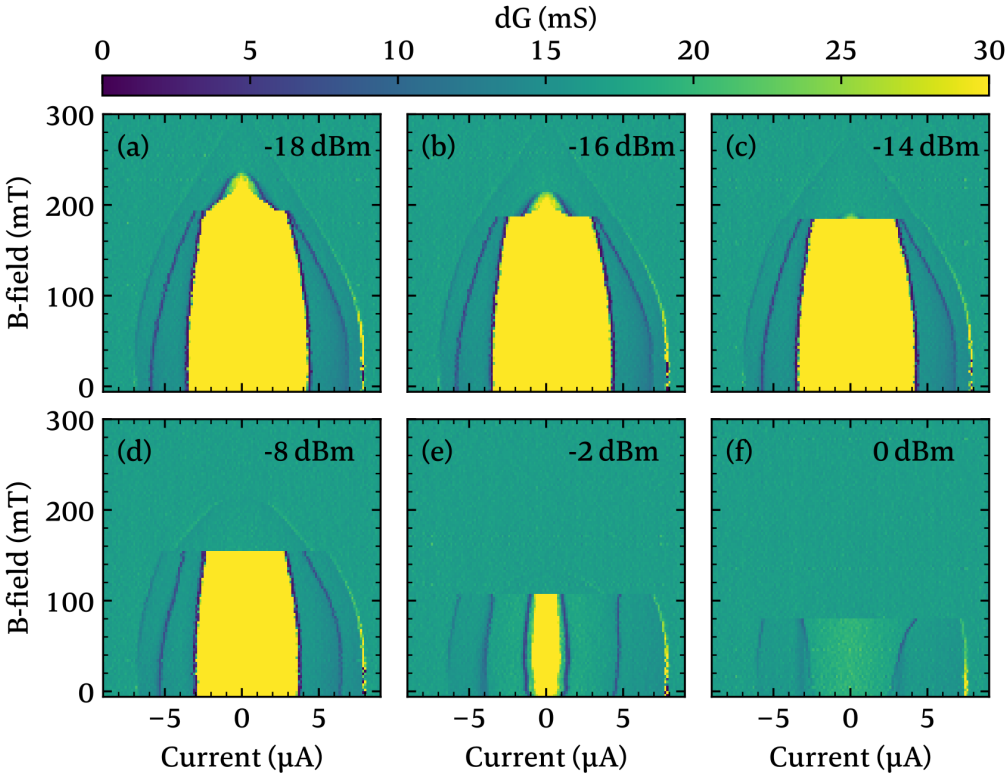

Figure 46: Differential conductance dG vs bias current and B-field under 30 GHz MW irradiation for different MW power with a temperature variation of (a) 370(9) mK, (b) 370(9) mK, (c) 372(9) mK, (d) 383(10) mK, (e) 406(11) mK and (f) 390(30) mK.

To check if the steps are really discontinuous or happen within a certain B-field range, a measurement with 13.95 GHz and a B-field step size of $\Delta B = 0.2$ mT was performed and is displayed in figure 45(c) for a bias current sweeping from negative to positive values (up sweep) and in figure 45(d) for a current sweep from positive to negative values (down sweep). Within $\Delta B = 0.2$ mT, no continuous change of I_{c1} is resolvable, thus the steps are discontinuous. The occurrence of the steps at slightly different B-field (± 0.4 mT) is most likely due to random fluctuations and not due to the sweep direction, because a repetition of the measurements in figure 45(a) and (b) with the same parameters led to a variation in the position of $\Delta B = 1$ mT. The same variation was observed in figure 44. The bias current sweep direction thus has no influence on the discontinuous steps.

The discontinuous steps in $I_{c1}(B)$ can appear or disappear for different T and evolve to higher B-fields for increasing T. In contrast to that, an increasing P shifts the steps to lower B-fields with an increasing step height. The steps could be observed for different MW frequencies but not for all. It seems that a special parameter set of MW frequency, T and P must be present for the steps to appear. A functional correlation between all parameters and the emergence of steps cannot be derived from our data. Therefore it is not clear if any MW frequency would lead to a discontinuous $I_{c1}(B)$ when the right T or P is set.

The physical origin of the steps is not clear. One could think of the magnetization of Co and its demagnetization with B-fields of the order of the coercive field of Co. Strambini et al. [89] have observed a step in the coherence peak of Al at the coercive field of -18.5 mT of their ferromagnetic insulator EuS which is in contact to Al. Their step evolves continuously within $\Delta B = 5$ mT. The fact that our steps occur at B-fields which are one order of magnitude higher than the coercive field of Co rather excludes the reorientation of magnetic moments in Co as a sufficient reason for the steps. Moreover, the steps should appear without MW applied as well, what is not the case in our studies. However, the dynamic magnetic configuration of Co under the influence of MW cannot be excluded as the reason for the steps. A measurement by Quay et al. [46] also shows a positive step of $I_c(B)$ in their S-F heterostructure made out of Al and Co under MW irradiation at $B \approx 185$ mT which seems to be discontinuous. Unfortunately, they do not comment on that step.

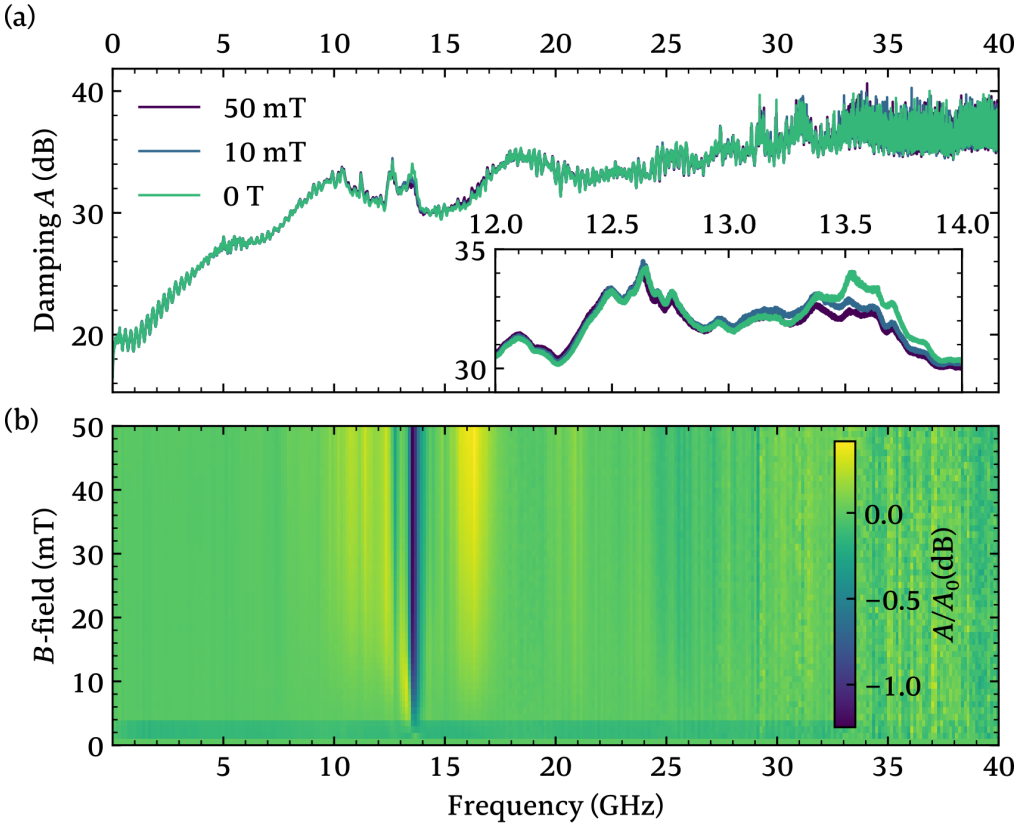

Figure 47: (a) Damping of the MW cabling in dB for B-fields of 0 T, 10 mT and 50 mT and for frequencies from 1 GHz to 40 GHz. The inset shows the section around 12 GHz to 14 GHz (b) Relative damping with respect to the damping at $B = 0$ T for B-field steps of 1 mT.

5.4 Microwave Response

The reason for the unusual critical current (I_{c1}) evolution in a magnetic field B is not known to us, as of today. One could think of a B-field dependent frequency response (damping) of the MW cabling, where the transmission is worse for high B-fields compared to the transmission at $B = 0\,\mathrm{T}$. In such a case the SC would be destroyed by the MW for low B-fields and recovered for high B-fields where the MW transmission is decreased. To check for such a trivial reason for the unusual $I_{c1}(B)$ behavior, a frequency response measurement was performed for various B-fields and is displayed in figure 47. In figure 47(a) the damping A of the MW frequencies from 1 GHz to 40 GHz through the whole MW cabling is plotted for B-fields of 0 T, 10 mT and 50 mT. The inset shows a section of the damping between 12 GHz and 14 GHz where a clear decrease of the damping at around 13.5 GHz is visible. Plotting the damping A/A_0 relative to the transmission spectrum for $B = 0\,\mathrm{T}$ in figure 47(b), illustrates the B-dependent decrease of the damping around 13.5 GHz by the false-color code black. The yellow stripes show an enhanced damping between 10 GHz and 17 GHz for $B \neq 0\,\mathrm{T}$. Three observations exclude the trivial B-field dependence of the damping as a reason for the unusual $I_{c1}(B)$ behavior. Firstly, an unusual $I_{c1}(B)$ was observed for frequencies where no pronounced $A(B)$ change is visible. Secondly, the P-dependent transport measurements in section 5.2 reveal that one needs to increase the MW power by at least 10 dB (e.g. from $P = -30\,\mathrm{dBm}$ to -20 dBm) to destroy the SC. The $A(B)$ spectrum shows a maximum change of around 1 dBm which would not be sufficient to destroy SC at $B = 0\,\mathrm{T}$ and recover it at higher B-fields. Thirdly, there is no clear correlation between the frequencies at which an unusual $I_{c1}(B)$ event occurs and those at which a pronounced $A(B)$ change happens. This can be seen by comparing figure 41 and figure 47.

5.5 Non-Monotonous Critical Current vs Temperature

In section 5.2, we have seen a maximum of I_{c2} and I_{c3} with respect to the MW power in sample A2. In sample A1, a maximum of $I_{c1}(T)$ can be observed for an increasing T. Figure 48 shows false-color plots of $\mathrm{d}G(I,B)$ for temperatures from $T = 365\,\mathrm{mK}$ to 800 mK with a MW frequency of 13.9 GHz in figure 48(a) to (f) and with 15.5 GHz in figure 48(g) to (l).

The green dashed line in figure 48(a) marks the B^{ref}-field at which the change of $I_{c1}(B)$ is minimal. The latter is marked with the red dashed lines and

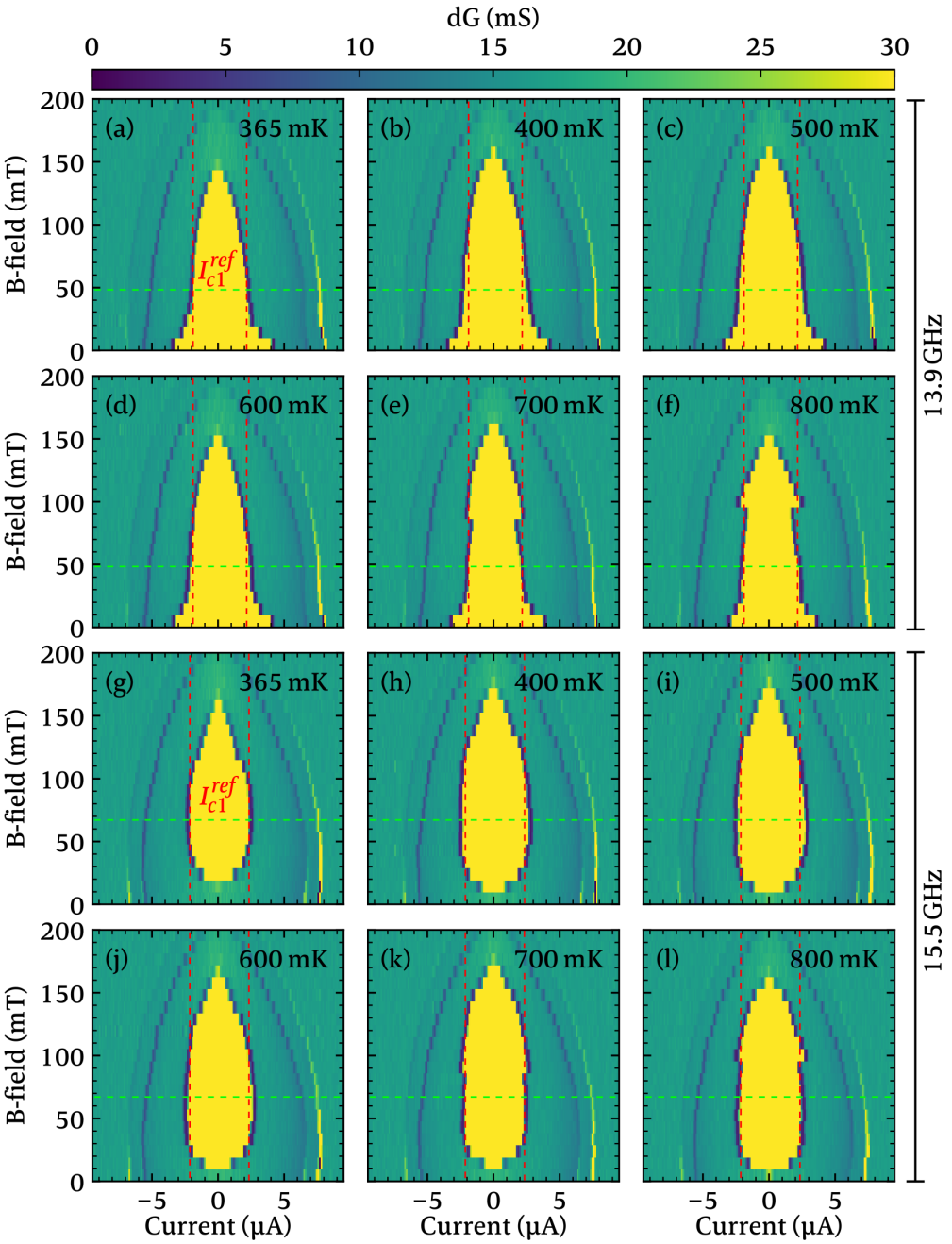

Figure 48: d$G(I,B)$ vs T (± 7 mK) for 13.9 GHz in (a) to (f) and for 15.5 GHz in (g) to (l). Red dashed lines indicate I_{c1}^{ref} at $T = 365$ mK, taken at green dashed line. Maximum of I_{c1} at $T = 400$ mK (13.9 GHz) and $T = 500$ mK (15.5 GHz).

denoted as I_{c1}^{ref}. Actually, the red dashed line at negative bias currents marks the re-trapping current I_{r1}^{ref}. For the sake of simplicity we will just name I_{c1}^{ref} in the following. An I_{c1}^{ref} is defined for the 15.5 GHz measurements in figure 48(g) with the same procedure as in figure 48(a). Drawing the red and green dashed lines for 13.9 GHz and 15.5 GHz in the respective figures for the higher Ts, one can see, at the intersection of the green and red dashed lines, an increase of I_{c1} with respect to I_{c1}^{ref} at $T = 365\,\mathrm{mK}$.

The increase of I_{c1} becomes clearer when plotting I_{c1} at B^{ref} (green dashed lines) for each temperature. The light and dark orange data points in figure 49 represent these individual $I_{c1}(B^{\mathrm{ref}})$ values. For 13.9 GHz, I_{c1} is maximal at around $B = 50\,\mathrm{mT}$ and between $T = 400\,\mathrm{mK}$ and $T = 500\,\mathrm{mK}$. It even appears that there is a minimum of I_{c1} at $T = 700\,\mathrm{mK}$. For 15.5 GHz, I_{c1} is maximal at around $B = 70\,\mathrm{mT}$ and between $T = 400\,\mathrm{mK}$ and $T = 600\,\mathrm{mK}$. The corresponding critical B_{c1}-fields, where I_{c1} goes to zero, are plotted in light and dark blue. For 13.9 GHz and 15.5 GHz, B_{c1} shows a minimum at $T = 600\,\mathrm{mK}$ and maximums at around $T = 500\,\mathrm{mK}$ and at $T = 700\,\mathrm{mK}$.

Since the measurements were performed up to 800 mK, there is no further information if the minima and maxima of I_{c1} and B_{c1} are part of a T-dependent oscillation. A non-monotonous $I_c(T)$, however, is predicted by Takahashi et al. [23] where a maximum of $I_c(T)$ emerges when MW are irradiated. A similar non-monotonous $I_c(T)$ is predicted by Eschrig and Löfwander [90] without MW but with disordered ferromagnetic moments at the S-F-interface. Both theories assume a half metal, what is a 100% spin polarized ferromagnet and a S-F-S Josephson junction. This supports our assumption of having a fJJ in the S/FS part of our samples. Moreover, our S-F-interface needs to host either a static or dynamic magnetic inhomogeneity.

5.6 Discussion

The unusual $I_c(B)$ behavior just emerges under the influence of MW irradiation. Publications on S-F-heterostructures under MW irradiation are rare and the comparability of their findings with our results are difficult what may be due to the complexity of our samples and the simultaneous emergence of several effects. Nevertheless, the following section, attempts to provide possible explanations for the origin of the unusual $I_c(B)$ behavior and discusses their similarities and inconsistencies to our results.

In the work of Patiño, Bell and Blamire [63], a sudden reduction of the critical current $I_c(B)$ near the coercive field of Co was observed in 25 nm thin Nb

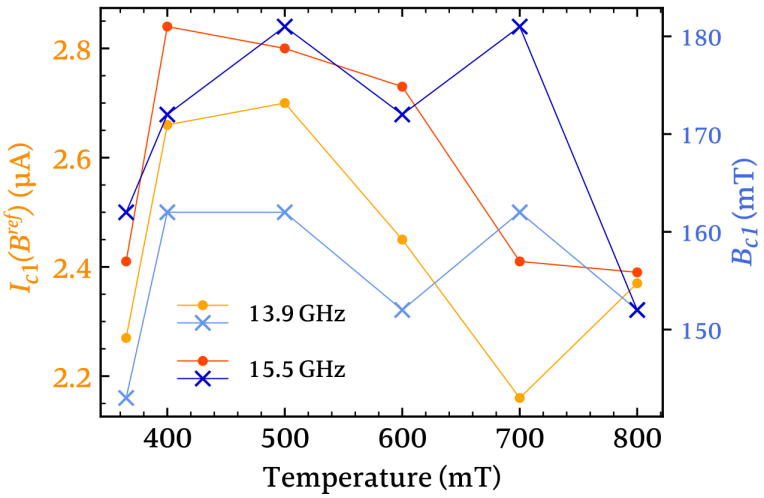

Figure 49: I_{c1}^{ref}s taken from figure 48 at intersection of I_{c1} and green dashed line to highlight the $I_{c1}(T)$ evolution in orange colors and the $B_{c1}(T)$ in blue colors.

which lay on top of Co. Later work by Patiño, Edgar and Blamire [62] could explain the sudden reduction of $I_c(B)$ by a sudden drop of the magnetization of Nb placed on top of Co when applying a in-plane B-field. They interpret the data as an alignment of naturally formed Bloch domain walls (BDW) in Co with the external B-field. The BDW create stray field vortices in the S which suppress $I_c(B)$ due to the magnetic proximity effect in Nb (see fig. 3 in sec. 2.5.1). The alignment of the domain walls (DW) in-plane of Co reduces the stray field and $I_c(B)$ recovers. This effect could just be observed for Co thicknesses of $d_F > 30\,\mathrm{nm}$. Lower thicknesses are expected to host Néel domain walls (NDW) which do not create the out-of-plane stray fields. Thicker Co layers enhanced the reduction of $I_c(B)$ since BDW are strengthened. The same effect could be observed by Rusanov, Golikova and Egorov [91] in Nb on top of permalloy.

Our sample have a Co thickness of $d_{\mathrm{Co}} \approx 2\,\mathrm{nm}$ and therefore hosting NDW. The alignment of the WG with respect to the sample is such that the ac $b(t)$-field component of the MW can cause a dynamic out-of-plane magnetization of Co (see fig. 8 in sec. 3.1) which is expected to suppress I_c. A sufficiently strong in-plane B-field re-aligns the magnetization of Co in-plane and I_c recovers. An increase of the suppression of I_c for increasing MW power supports that picture since a rising ac $b(t)$-field should enhance the out-of-plane magnetization of

Co what is comparable to the static strengthening of BDW by thicker Co layers.

Neither the anomalous $I_{c1}(B)$ behavior can be explained by the dynamic out of plane magnetization, nor the fact that the suppression of $I_{c1}(B=0)$ is just observable in frequency spans of 4.5 GHz to 7.9 GHz and of 11 GHz to 16 GHz, though.

Another explanation is motivated by the similarity of the non-monotonous $I_{c1}(T)$ from the previous section with the theory of Eschrig and Löfwander [90] and Takahashi et al. [23]. The latter is the basis for the theory of Hikino et al. [28] which predicts a suppression of the Josephson coupling when an odd number of magnons are generated in F by MW. A enhanced coupling arises for an even magnon number (see sec. 2.5.2). Following this picture, the non-monotonous $I_{c1}(B)$ may be due to an odd magnon number and the anomalous $I_{c1}(B)$ due to an even number of magnons. The fact that I_{c1} under MW irradiation never exceeds I_{c1} without MW can be explained by a general reduction of the SC due to local heating as discussed in section 5.1. The anomalous $I_{c1}(B)$ consequently can be interpreted as an relative enhancement of I_c around a MW frequency of 14 GHz. According to Takahashi et al. [23], this frequency should be the FMR of our Co, which would be around three times to large than expected from measurements on thin film Co conducted by Irtenkauf [92]. Moreover, the analysis in figure 41 from section 5.3.2 does not show a clear repetition between non-monotonous and anomalous $I_{c1}(B)$ within an interval of the MW frequency $\omega = n\omega_0$. The explanatory model about a dynamic sc spin triplet Josephson coupling can naively explain the emergence of the non-monotonous $I_{c1}(B)$ and the anomalous $I_{c1}(B)$. The inconsistencies to our results, however, renders this hypothesis as a sufficient explanation rather unlikely.

Our results may originate from a combination of multiple physical phenomena mentioned throughout the thesis, and under certain parameter configurations the one or the other dominates.

5.7 Hysteretic Resistance vs Temperature

The last section showed that I_c is not just non-monotonously dependence on the B-field but also on T. Figure 50 shows the qualitative similarity between the influence of the B-field and T on the resistance R for a fixed bias current. In 50(a) a bias current of 2 µA was applied to measure R during a cool-down of the cryostat while a 5.2 GHz MW was irradiated and different B-fields were applied, at different cool-downs. The increase of R at $T = 1.5$ K in the cool-down curve of figure 22 is suppressed for an irradiated 5.2 GHz MW and applied

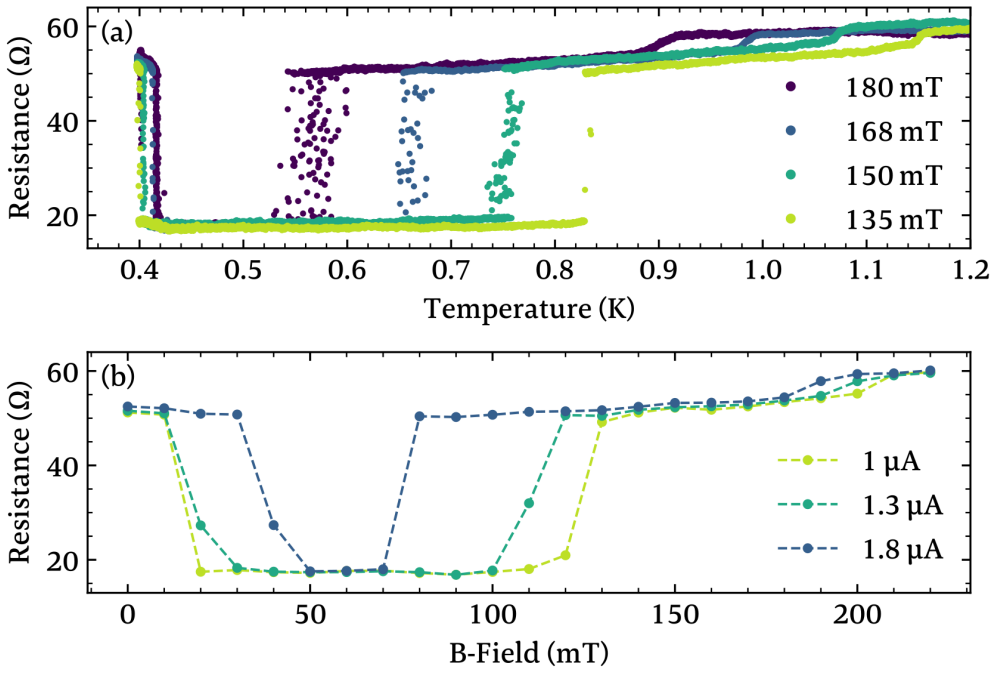

Figure 50: Transport measurements with 5.2 GHz MW irradiation. (a) $R(T)$ measurement for decreasing T and for different B-fields. (b) $R(B)$ curves are line cuts of figure 37(b) for different constant bias currents at $T = 368(7)$ mK. The dashed lines are a guide for the eye.

B-fields. Instead, a small drop in the resistance of 3 Ω appears at $T = 1.15$ K for $B = 135$ mT which shifts to $T = 900$ mK for $B = 180$ mT. These drops mark T_c for the various parameter configurations. The big jump in R of about 32 Ω shifts from 1.1 K (without MW and B-fields) to 830 mK for 135 mT and to 570(30) mK for 180 mT. This is as expected for a stronger weakening of S for increasing B-fields. This big jump appears to be more and more a noisy transition when the B-field rises. Since the data points plotted are averages over 1000 data points collected by the DAQ, the noisy part is more likely a hopping of R between the two resistance levels 51 Ω and 18 Ω. The jump of R back to around $R = 52$ Ω at low T shifts for increasing B-fields from 400 mK to 420 mK.

If one takes line cuts at fixed bias current values through figure 37(b), $R(B)$ curves can be plotted for a 5.2 GHz MW irradiation, as is depicted in figure 50(b. The dashed lines are guides for the eyes. The qualitative trend of $R(B)$ (figure 50(b)) and $R(T)$ (figure 50(a)) looks astonishingly alike. The general impact of a B-field on R seems to be the same as for T. The cool-down curve taken with $B =$ 168 mT is also shown in figure 51(a) in cyan color, together with a subsequent warm-up curve in yellow up to $T = 930$ mK. Surprisingly, R shows a hysteretic behavior with respect to the T gradient. During the first cool-down from 4 K to $T_{\text{base}} \approx 370$ mK, the resistance drops to 18 Ω and ends up at a higher-resistive state $R^* \approx 52$ Ω close to T_{base}. The sample seems to be trapped in this R^* state when it warms up again. It even stays in this state when it gets cooled down directly from 930 mK to T_{base}.

Normally, a sample warms up to 4 K before it gets cooled down again. The known behavior of R, with its resistance drop at around $T = 1.1$ K (without B-field or MW) and the final increase of R at low T is then observable. The sample seems to be released from the trapped state when overcoming a certain T. It is reasonable to assume this T might be a T_c of one of the sample parts, if one thinks of magnetic flux trapping to be the reason for the hysteresis. Figure 51(b) shows a $R(T)$ measurement with 5.2 GHz MW irradiation from T_{base} to 1.62 K and still being predominantly in the trapped R^* state when subsequently cooling down to T_{base}. The trapped state fluctuates between R^* and the low-resistive state $R = 18$ Ω. The temperature around $T = 1.62$ K seems to be the onset where the sample gets released from the trapped state. This release T is 11% above $T_c = 1.5$ K of the bare S parts. However, the similarity of $R(T)$ and $R(B)$ in figure 50 lead to the assumption that the hysteresis is correlated to the high-conductive part of the sample, because the $R(B)$ curves in 50(b) are taken from the high-conductive regime of figure 37(b). The high-conductive part is associated to the S/SF part of the sample, according to all previous analysis, but

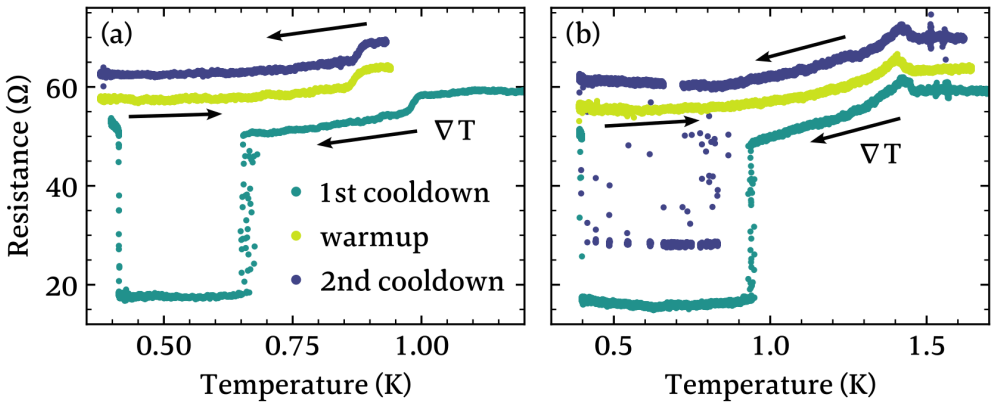

Figure 51: $R(T)$ measurement for decreasing T (cool-down, $\leftarrow \nabla T$) and increasing T (warm-up, $\rightarrow \nabla T$). (a) A first cool-down (cyan) from 4 K to $T_{\text{base}} \approx 370$ mK is followed by a warm-up (yellow) to 930 mK and a subsequent second cool-down (blue) to T_{base}, with a constantly applied B-field of 168 mT. The drop in R in the first cool-down (cyan) is shifted to higher T compared to the yellow and blue $R(T)$ curve because of a higher ∇T during the first cool-down. (b) Same procedure as in (a) but with a warm-up to 1.62 K and no B-field. The sample was demagnetized before the $R(T)$ measurements. The blue and yellow curves are shifted by 5 Ω each for clarity.

its $T_c = 1.1\,\mathrm{K}$ is even lower than 1.5 K, which itself is already smaller than the releasing $T = 1.62\,\mathrm{mK}$. On the other hand, a correlation of the different sample parts was shown and $T_c = 1.5\,\mathrm{K}$ still might be the temperature where the sample gets released from the trapped state. This argumentation is corroborated by considering potential differences in T at the sample and at the thermometer during the successive cool-downs and warm-ups.

An ordinary flux trapping can rather be excluded, because a measurement like in figure 50(a) does not show such a pronounced hysteresis for different B-field sweep directions (see fig. 43). Even more, the fact that the $R(T)$ data in figure 51(b) was taken without an applied B-field, and that the sample was even demagnetized before the measurement, makes a flux trapping of a constant B-field impossible. The trapping of R^* must be due to the MW irradiation, because the increase of R to R^* at low T just occurs under MW irradiation. A trapping of the static stray field of Co thus can also rather be neglected. The effect of a R^* trapping was also observed for 13 GHz without B-field and thus is not unique to a 5.2 GHz MW irradiation.

We cannot explain the $R(T)$ hysteresis with a static flux trapping. However, we can say, that this effect must be an interplay of T, the MWs and most likely the ferromagnetic Co in the S/FS part of the sample. The actual mechanism for the $R(T)$ hysteresis is unknown to us.

Little is known about a hysteretic temperature-resistance behavior in literature. Minhas et al. in 2017 [47] and Yan et al. in 2020 [48] observed a different $R(T)$ for a decreasing and increasing T in a metallic two dimensional electron gas (2DEG) formed at the interface of the two insulators $LaAlO_3/SrTiO_3$ in combination with an applied backgate voltage V_{BG}. The most-detailed explanation was given by Kwak et al. in 2022 [49]. The V_{BG} injects electrons not only in the 2DEG but also into impurity sites. A T dependent dielectric constant increases the charge carrier density in the 2DEG and at the impurity sites during cool-down. The electrons at the impurity sites are trapped and are energetically stable. This leads to a preferential reduction of the number of mobile electrons from the 2DEG during the warm-up and appears as an increase in R compared to the cool-down. Although, the physical system of a 2DEG in $LaAlO_3/SrTiO_3$ is pretty different from our S-F-heterostructures, their findings show that complex electronic states can appear as a $R(T)$ hysteresis.

6 Conclusion

Our work on superconductor (S)-ferromagnet (F)-heterostructures under microwave (MW) irradiation reveals a variety of different transport phenomena, which will be summarized after a brief overview of the structure of the dissertation.

In order to embed our work in the field of superconducting spintronics, chapter 1 gives an overview of the current state of research. The chapter 2 highlights the physical fundamentals that play a role in our work, like superconductivity (sec. 2.1) and Josephson junctions (JJ) (sec. 2.2), microwaves (sec. 2.3), magnetism (2.4) and the interplay of all these (sec. 2.5), where proximity effects emerge (sec. 2.5.1) and the response of ferromagnetic Josephson junctions (fJJ) to MW (sec. 2.5.2).

Chapter 3 shows how our samples are composed and how they were produced (sec. 3.1). The measurement setup presented in section 3.2 consist of the cryogenics (sec. 3.2.1) and the ac and dc electronics (sec. 3.2.2).

The results of our experiments can be categorized in two transport regimes. Firstly, in transport measurements under static conditions without MW which are summarized in chapter 4. Basic sample properties, like the superconducting gap energy Δ and the critical magnetic field B_c were identified in section 4.1 and the transport characteristics without B-fields are analyzed in section 4.2. The discussion of which feature in the transport characteristic arose from which sample part is presented in section 4.3. The relation between the transport characteristics and the sample parts is further elaborated within the investigation of the temperature (T) response of the samples in section 4.4 and the magnetic B-field dependence in section 4.5."

Secondly, the transport measurements under the influence of MW are summarized in chapter 5, where the observation of MW induced local heating is stated in section 5.1, followed by results on MW stimulated superconductivity in section 5.2. The astonishing and difficult to interpret unusual critical current evolution in a B-field ($I_c(B)$) under MW irradiation is shown in section 5.3 which can be subdivided into a non-monotonous (sec. 5.3.1), an anomalous (sec. 5.3.2) and a discontinuous $I_c(B)$ behavior (sec. 5.3.3). Section 5.4 shows that a B-field dependent MW frequency response of the setup can be excluded as a trivial explanation for the unusual $I_c(B)$ behavior, whose temperature (T) dependence is investigated in section 5.5. An attempt of an explanation for the unusual $I_c(B)$ behavior is made in section 5.6. The last section 5.7 shows results of a T dependent hysteresis of the resistance R.

The investigated S-F-heterostructures consist of 50 nm thin Al and 12 nm thin ferromagnetic Co which are stacked to Al-Co-Al trilayers. The layers are aligned with respect to each other in such a way that different sample parts are formed. Parts of bare Al (S part), parts where Al lays on top or under the Co layer (SF part), and parts where two Al layers sandwich the Co layer (S/FS part). The SF parts experience the strongest exchange field from Co which leads in most samples to a complete suppression of the SC in one SF part. A residual resistance is then measured down to the base temperature $T_{base} \approx 360\,\mathrm{mK}$.

In conclusion of our work, it can be said that the complex sample structure leads to phenomena, some of which can clearly be assigned to known effects, for some, explanatory models are proposed, which, however, show partial inconsistencies to our results, and for the observed $R(T)$ hysteresis we could not find an explanation but compared it with similar findings in different physical systems.

The fact of a geometrically reduced Co thickness to around 1.5 nm, the pronounced hysteresis of the biggest step in the I-Vs and the maximum of the corresponding critical current $I_{c1}(T)$ at $T > T_{base}$, which can emerge in fJJs, strongly suggest a formation of a fJJ in the S/FS part although no Fraunhofer pattern is visible.

The comparison to thermal heating reveals a preferential local heating of the S/FS part by the MW. The stronger dissipation in the S/FS part is due to a coupling of the MW to the F in the fJJ. The coupling not only leads to a pronounced heat dissipation, but also to a suppression of the SC in the S/FS part which can be restored for B-fields higher than the coercive field of Co, what we call non-monotonous $I_c(B)$ behavior. This may be due to a dynamic out-of-plain magnetization of the naturally in-plain magnetized thin Co by the MW or due to a B-field dependent coupling of the MW into the sample. The latter theory can rather be excluded due to differences in the experimental conditions and both theories cannot explain the anomalous $I_c(B)$ behavior. We speak of an anomalous $I_c(B)$ when I_c is strongest around $B = 0\,\mathrm{T}$, but decreases strongest around the coercive field of Co, before I_c decreases monotonically for increasing B-fields as one would expect for a orbital depairing. Since this effect just occurs around the small frequency span of 14.1(3) GHz, a resonant effect seems reasonable, like the stimulation of an even number of magnons by the MW which lead to a dynamic sc spin triplet JJ coupling. An odd magnon number would suppress the JJ coupling. Partial inconsistencies of the underlying theory with our results render this hypothesis unlikely to be a sufficient explanation of the unusual $I_c(B)$ behavior. We think the unusual $I_c(B)$ behav-

ior is a combination of effects emerging in our S-F-heterostructures under MW irradiation where the one or the other dominates under a certain parameter configuration.

Controlling a dynamic spin triplet formation in fJJs is an extremely challenging task. More control experiments are needed which are tailored to the individual findings of this dissertation, like the investigation of a potential dynamic magnetic texture of our Co layer by magnetic force microscopy with and without MW irradiation. A variation of the Co layer thickness would allow to check for FFLO states to confirm the presence of sc spin triplets and a variation of the dimensions of the samples may yield Fraunhofer patterns and Shapiro steps to definitely confirm the presence of a fJJ and allows to further investigate a potential dynamic JJ coupling.

References

1. R. R. Cai, I. Zutic & W. Han. Superconductor/Ferromagnet Heterostructures: A Platform for Superconducting Spintronics and Quantum Computation. *Adv Quantum Technol* **6** (2023).
2. N. Elsayed, A. S. Maida & M. Bayoumi. A Review of Quantum Computer Energy Efficiency. *IEEE Green Technol,* 1 (2019).
3. D. Jaschke & S. Montangero. Is quantum computing green? An estimate for an energy-efficiency quantum advantage. *Quantum Sci Technol* **8** (2023).
4. H. K. Onnes. Further experiments with liquid helium D. On the change of the electrical resistance of pure metals at very low temperatures, etc V. The disappearance of the resistance of mercury. *Proceedings Royal Acad Amsterd* **14,** 113 (1911).
5. H. K. Onnes. Further experiments with liquid helium G. On the electrical resistance of pure metals, etc. VI. On the sudden change in the rate at which the resistance of mercury disappears. *Proceedings Royal Acad Amsterd* **14,** 818 (1912).
6. J. Bardeen, L. N. Cooper & J. R. Schrieffer. Theory of Superconductivity. *Phys Rev* **108,** 1175 (1957).
7. L. N. Cooper. Bound Electron Pairs in a Degenerate Fermi Gas. *Phys Rev* **104,** 1189 (1956).
8. F. S. Bergeret, A. F. Volkov & K. B. Efetov. Induced ferromagnetism due to superconductivity in superconductor-ferromagnet structures. *Phys Rev B* **69,** 174504 (2004).
9. V. O. Yagovtsev, N. G. Pugach & M. Eschrig. The inverse proximity effect in strong ferromagnet-superconductor structures. *Supercond Sci Tech* **34** (2021).
10. R. I. Salikhov *et al.* Spin screening effect in superconductor/ferromagnet thin film heterostructures studied using nuclear magnetic resonance. *Phys Rev B* **80,** 214523 (2009).
11. M. Houzet & A. I. Buzdin. Long range triplet Josephson effect through a ferromagnetic trilayer. *Phys Rev B* **76** (2007).
12. M. Eschrig. Spin-polarized supercurrents for spintronics: a review of current progress. *Rep Prog Phys* **78,** 104501 (2015).

13. J. Linder & J. W. A. Robinson. Superconducting spintronics. *Nat Phys* **11,** 307 (2015).

14. J. W. A. Robinson, J. D. S. Witt & M. G. Blamire. Controlled Injection of Spin-Triplet Supercurrents into a Strong Ferromagnet. *Science* **329,** 59 (2010).

15. M. Alidoust & J. Linder. Spin-triplet supercurrent through inhomogeneous ferromagnetic trilayers. *Phys Rev B* **82,** 224504 (2010).

16. S. Diesch *et al.* Creation of equal-spin triplet superconductivity at the Al/EuS interface. *Nat Commun* **9,** 5248 (2018).

17. R. Fermin *et al.* Superconducting Triplet Rim Currents in a Spin-Textured Ferromagnetic Disk. *Nano Lett* **22,** 2209 (2022).

18. Y. Jungxiang, R. Fermin, K. Lahabi & J. Aarts. Triplet supercurrents in lateral Josephson junctions with a half-metallic ferromagnet. *arXiv:2303.13922v1 [cond-mat.supr-con]* (2023).

19. R. S. Keizer *et al.* A spin triplet supercurrent through the half-metallic ferromagnet CrO2. *Nature* **439,** 825 (2006).

20. M. S. Anwar, F. Czeschka, M. Hesselberth, M. Porcu & J. Aarts. Long-range supercurrents through half-metallic ferromagnetic CrO_2. *Phys Rev B* **82,** 100501 (2010).

21. F. S. Bergeret & I. V. Tokatly. Spin-orbit coupling as a source of long-range triplet proximity effect in superconductor-ferromagnet hybrid structures. *Phys Rev B* **89,** 134517 (2014).

22. J. R. Eskilt, M. Amundsen, N. Banerjee & J. Linder. Long-ranged triplet supercurrent in a single in-plane ferromagnet with spin-orbit coupled contacts to superconductors. *arXiv:1906.07725v1* (2019).

23. S. Takahashi, S. Hikino, M. Mori, J. Martinek & S. Maekawa. Supercurrent Pumping in Josephson Junctions with a Half-Metallic Ferromagnet. *Phys Rev Lett* **99,** 057003 (2007).

24. I. Petković, M. Aprili, S. E. Barnes, F. Beuneu & S. Maekawa. Direct dynamical coupling of spin modes and singlet Josephson supercurrent in ferromagnetic Josephson junctions. *Phys Rev B* **80,** 220502 (2009).

25. K.-R. Jeon *et al.* Enhanced spin pumping into superconductors provides evidence for superconducting pure spin currents. *Nat Mater* **17,** 499 (2018).

26. I. V. Bobkova, A. M. Bobkov & M. A. Silaev. Dynamic Spin-Triplet Order Induced by Alternating Electric Fields in Superconductor-Ferromagnet-Superconductor Josephson Junctions. *Phys Rev Lett* **127,** 147701 (2021).

27. S. Hikino, M. Mori, S. Takahashi & S. Maekawa. Geometrical dependence of Josephson current induced by ferromagnetic resonance in ferromagnetic Josephson junctions. *Physica C-Superconductivity and Its Applications* **470,** S819 (2010).

28. S. Hikino, M. Mori, S. Takahashi & S. Maekawa. Microwave-induced supercurrent in a ferromagnetic Josephson junction. *Supercond Sci Tech* **24,** 024008 (2011).

29. S. Shapiro. Josephson Currents in Superconducting Tunneling: The Effect of Microwaves and Other Observations. *Phys Rev Lett* **11,** 80 (1963).

30. A. F. G. Wyatt, V. M. Dmitriev, W. S. Moore & F. W. Sheard. Microwave-Enhanced Critical Supercurrents in Constricted Tin Films. *Phys Rev Lett* **16,** 1166 (1966).

31. A. H. Dayem & J. J. Wiegand. Behavior of Thin-Film Superconducting Bridges in a Microwave Field. *Phys Rev* **155,** 419 (1967).

32. G. M. Eliashberg. Film Superconductivity Stimulated by a High-Frequency Field. *JETP* **11,** 114 (1970).

33. I. V. Zolochevskii. Stimulation of superconductivity by microwave radiation in wide tin films. *Low Temp Phys* **39,** 571 (2013).

34. S. L. McCarthy & J. Warman. Microwave and Magnetic-Field Effects in Superconducting Granular Aluminum Film Microbridges. *J Low Temp Phys* **14,** 521 (1974).

35. J. Flouquet & A. Buzdin. Ferromagnetic superconductors. *Phys World* **15,** 41 (2002).

36. V. P. Mineev. Superconductivity in uranium ferromagnets. *arXiv:1605.07319v3* **60,** 121 (2017).

37. F. Lévy, I. Sheikin, B. Grenier & A. D. Huxley. Magnetic Field-Induced Superconductivity in the Ferromagnet URhGe. *Science* **309,** 1343 (2005).

38. D. Aoki & J. Flouquet. Ferromagnetism and Superconductivity in Uranium Compounds. *arXiv:1108.4807v1* (2012).

39. S. Ran *et al.* Enhancement and reentrance of spin triplet superconductivity in UTe_2 under pressure. *Phys Rev B* **101,** 140503 (2020).

40. A. Rosuel *et al.* Field-Induced Tuning of the Pairing State in a Superconductor. *Phys Rev X* **13,** 011022 (2023).

41. K. Kinjo *et al.* Change of superconducting character in UTe_2 induced by magnetic field. *Phys Rev B* **107,** L060502 (2023).

42. V. D. Esin *et al.* Reentrant proximity-induced superconductivity for GeTe semimetal. *arXiv:2304.05971v2* (2023).

43. A. Lau & C. Ortix. Topological Semimetals in the SnTe Material Class: Nodal Lines and Weyl Points. *Phys Rev Lett* **122,** 186801 (2019).

44. J. Krempasky *et al.* Triple-Point Fermions in Ferroelectric GeTe. *Phys Rev Lett* **126,** 206403 (2021).

45. R. Meservey & D. H. Douglass. Energy Gap Measurements by Tunneling between Superconducting Films. 2. Magnetic Field Dependence. *Phys Rev* **135,** A24 (1964).

46. C. H. L. Quay, M. Weideneder, Y. Chiffaudel, C. Strunk & M. Aprili. Quasiparticle spin resonance and coherence in superconducting aluminium. *Nat Commun* **6,** 9660 (2015).

47. M. Z. Minhas, A. Muller, F. Heyroth, H. H. Blaschek & G. Schmidt. Temperature dependent giant resistance anomaly in $LaAlO_3/SrTiO_3$ nanostructures. *Sci Rep* **7,** 5215 (2017).

48. X. Yan, H. Zhang, B. G. Shen, F. X. Hu & J. R. Sun. Transport abnormity and its modulations via gating effect and light illumination at the $SrNbO_3/SrTiO_3$ interface. *Mater Res Express* **7,** 096407 (2020).

49. Y. Kwak, W. Han, J. S. Lee, J. Song & J. Kim. Hysteretic temperature dependence of resistance controlled by gate voltage in LaAlO3/SrTiO3 heterointerface electron system. *Sci Rep* **12,** 6458 (2022).

50. D. R. Lide. *CRC Handbook of Chemistry and Physics (CD-ROM Version)* 90th ed. (CRC Press/Taylor and Francis, Boca Raton, 2010).

51. R. B. Pettit & J. Silcox. Film Structure and Enhanced Superconductivity in Evaporated Aluminum Films. *Phys Rev B* **13,** 2865 (1976).

52. D. H. Douglass & R. Meservey. Energy Gap Measurements by Tunneling between Superconducting Films. I. Temperature Dependence. *Phys Rev* **135,** A19 (1964).

53. M. D. Maloney, M. Cardona & F. Delacruz. Superconducting Parameters and Size Effects of Aluminum Films and Foils. *Phys Rev B* **5,** 3558 (1972).

54. C. Kittel & P. McEuen. *Introduction to Solid State Physics* 8th ed. (John Wiley and Sons, Inc, Hoboken, NJ, 2005).

55. M. Tinkham. *Introduction to Superconductivity* 2nd ed. (McGraw Hill, New York, 1996).

56. V. Palenskis. The effective density of randomly moving electrons and related characteristics of materials with degenerate electron gas. *AIP Adv* **4,** 047119 (2014).

57. P. Mangin & R. Kahn. *Superconductivity: An Introduction* 1st ed. (Springer International Publishing, Cham (Switzerland), 2017).

58. B. D. Josephson. Possible New Effects in Superconductive Tunnelling. *Phys Lett* **1,** 251 (1962).

59. P. M. Tedrow & R. Meservey. Critical Thickness for Ferromagnetism and Range of Spin-Polarized Electrons Tunneling into Co. *Solid State Commun* **16,** 71 (1975).

60. J. M. Alameda *et al.* Effects of the initial stages of film growth on the magnetic anisotropy of obliquely-deposited cobalt thin films. *J Magn Magn Mater* **154,** 249 (1996).

61. R. J. Kinsey, G. Burnell & M. G. Blamire. Active supercurrent control in superconductor/ferromagnet heterostructures. *IEEE T Appl Supercon* **11,** 904 (2001).

62. E. J. Patiño & M. G. Blamire. Sudden magnetization drops in superconductor/ferromagnet bilayered structures. *Supercond Sci Tech* **32,** 01LT02 (2018).

63. E. J. Patino, C. Bell & M. G. Blamire. Sudden critical current drops induced in S/F structures. *Eur Phys J B* **68,** 73 (2009).

64. M. Sato & Y. Ishii. Critical sizes of cobalt fine particles with uniaxial magnetic anisotropy. *J Appl Phys* **54,** 1018 (1983).

65. J. Camarero, J. J. de Miguel, R. Miranda, V. Raposo & A. Hernando. Influence of film morphology on perpendicular magnetic anisotropy. *Phys Rev B* **64,** 125406 (2001).

66. B. Hillebrands & K. Ounadjela. *Spin dynamics in confined magnetic structures II* (Springer Science and Business Media, 2003).

67. C. Bell, S. Milikisyants, M. Huber & J. Aarts. Spin dynamics in a superconductor-ferromagnet proximity system. *Phys Rev Lett* **100,** 047002 (2008).

68. S. S. Kalarickal *et al.* Ferromagnetic resonance linewidth in metallic thin films: Comparison of measurement methods. *J Appl Phys* **99,** 093909 (2006).

69. P. Fulde & R. A. Ferrell. Superconductivity in Strong Spin-Exchange Field. *Phys Rev A* **135,** 550 (1964).

70. A. I. Larkin & Y. N. Ovchinnikov. Inhomogeneous State of Superconductors. *Sov Phys Jetp-Ussr* **20,** 762 (1965).

71. J. W. A. Robinson, S. Piano, G. Burnell, C. Bell & M. G. Blamire. Critical current oscillations in strong ferromagnetic π junctions. *Phys Rev Lett* **97,** 177003 (2006).

72. R. P. Boardman. *Computer simulation studies of magnetic nanostructures* Thesis (University of Southampton, 2005).

73. J. W. Ekin. *Experimental Techniques for Low-Temperature Measurements* 1st ed. (Oxford University Press Inc., New York, 2006).

74. Oxford Instrumens. *HelioxVL Sorption pump 3He Insert* Operator's Handbook (2005).

75. Yokogawa. *Model 7615 Programmable DC Source* Operator's Handbook (1990).

76. N. A. Court, A. J. Ferguson & R. G. Clark. Energy gap measurement of nanostructured aluminium thin films for single Cooper-pair devices. *Supercond Sci Tech* **21,** 015013 (2008).

77. L. Hall. *Survey of Electrical Resistivity Measurements on 16 Pure Metals in the Temperature Range 0 to 2730 K* (US Department of Commerce, National Bureau of Standards, 1968).

78. V. Palenskis. Drift Mobility, Diffusion Coefficient of Randomly Moving Charge Carriers in Metals and Other Materials with Degenerated Electron Gas. *World Journal of Condensed Matter Physics* **03,** 73 (2013).

79. M. J. Wolf, C. Sürgers, G. Fischer & D. Beckmann. Spin-polarized quasiparticle transport in exchange-split superconducting aluminum on europium sulfide. *Phys Rev B* **90,** 144509 (2014).

80. L. J. Sun *et al.* The electrical resistivities of nanostructured aluminium films at low temperatures. *J Phys D Appl Phys* **50,** 415302 (2017).

81. A. M. Kadin, W. J. Skocpol & M. Tinkham. Magnetic field dependence of relaxation times in nonequilibrium superconductors. *J Low Temp Phys* **33,** 481 (1978).

82. V. I. Fal'ko, C. J. Lambert & A. F. Volkov. Andreev reflections and magnetoresistance in ferromagnet-superconductor mesoscopic structures. *JETP* **69,** 532 (1999).

83. A. B. Cawthorne, C. B. Whan & C. J. Lobb. Complex dynamics of resistively and inductively shunted Josephson junctions. *J Appl Phys* **84,** 1126 (1998).

84. I. Giaever & K. Megerle. Study of Superconductors by Electron Tunneling. *Phys Rev* **122,** 1101 (1961).

85. B. Borcsok, S. Komori, A. I. Buzdin & J. W. A. Robinson. Fraunhofer patterns in magnetic Josephson junctions with non-uniform magnetic susceptibility. *Sci Rep* **9,** 5616 (2019).

86. M. Alidoust, G. Sewell & J. Linder. Non-Fraunhofer Interference Pattern in Inhomogeneous Ferromagnetic Josephson Junctions. *Phys Rev Lett* **108,** 037001 (2012).

87. J. A. Pals & J. Dobben. Measurements of Microwave-Enhanced Superconductivity in Aluminum Strips. *Phys Rev B* **20,** 935 (1979).

88. J. A. Pals & J. Dobben. Observation or Order-Parameter Enhancement by Microwave Irradiation in a Superconducting Aluminum Cylinder. *Phys Rev Lett* **44,** 1143 (1980).

89. E. Strambini *et al.* Revealing the magnetic proximity effect in EuS/Al bilayers through superconducting tunneling spectroscopy. *Phys Rev Mater* **1,** 054402 (2017).

90. M. Eschrig & T. Löfwander. Triplet supercurrents in clean and disordered half-metallic ferromagnets. *Nat Phys* **4,** 138 (2008).

91. A. Y. Rusanov, T. E. Golikova & S. V. Egorov. Change in the sign of the magnetoresistance effect in bilayer superconductor/ferromagnet structures under change in the type of the domain structure in the ferromagnet. *JETP* **87,** 175 (2008).

92. O. Irtenkauf. *Broadband ferromagnetic resonance measurements on thin cobalt films at low temperatures* Master Thesis (University of Konstanz, 2021).